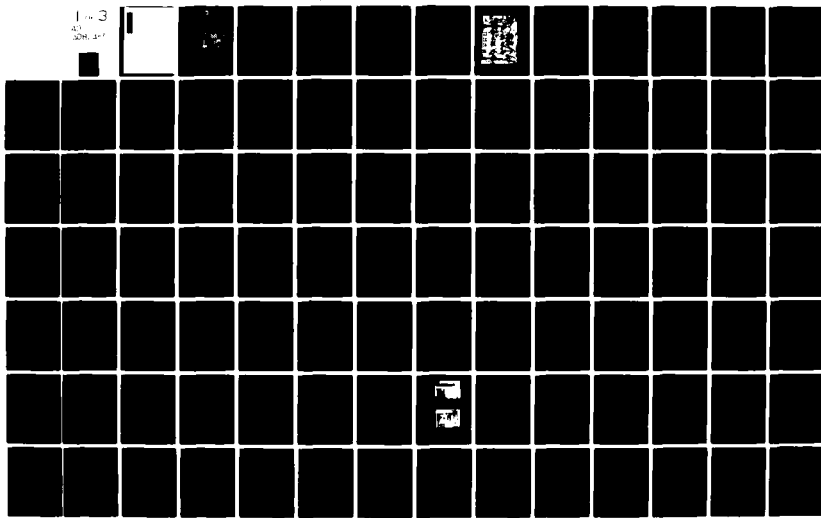


AD-A082 455

WOODS HOLE OCEANOGRAPHIC INSTITUTION MASS F/G 8/3
1979 SUMMER STUDY PROGRAM IN GEOPHYSICAL FLUID DYNAMICS AT THE --ETC(U)
NOV 79 M E STERN, F K MELLOR N00016-79-C-0671
UNCLASSIFIED WHOI-79-84-VOL-2 NL

1-3
43
304-147



ADA082455

14 WHOI-79-84-VOL-2

6 1979 SUMMER STUDY PROGRAM
IN
GEOPHYSICAL FLUID DYNAMICS at
THE WOODS HOLE OCEANOGRAPHIC INSTITUTION,
NOTES ON POLAR OCEANOGRAPHY. Volume II.
By Lectures of the Fellows.

10 Melvin E. Stern Director
and
Florence K. Mellor Editor

WOODS HOLE OCEANOGRAPHIC INSTITUTION
Woods Hole, Massachusetts 02543

11 Nov 1979

12 226

9 TECHNICAL REPORT

Prepared for the Office of Naval Research under
Contract N00014-79-C-0671
15

Reproduction in whole or in part is permitted for any purpose
of the United States Government. This report should be cited as:
Woods Hole Oceanographic Institution Technical Report WHOI-79-84

Approved for public release; distribution unlimited.

Approved for Distribution

Charles D. Hollister
Charles D. Hollister
Dean of Graduate Studies

381000

Jim

1979 SUMMER STUDY PROGRAM
in
GEOPHYSICAL FLUID DYNAMICS
at
THE WOODS HOLE OCEANOGRAPHIC INSTITUTION
NOTES ON POLAR OCEANOGRAPHY

Accession For	
NTIS GRA&I	<input checked="" type="checkbox"/>
DDC TAB	<input type="checkbox"/>
Unannounced Justification	<input type="checkbox"/>
By _____	
Distribution/ _____	
Availability Codes	
Dist.	Avail and/or special
A	

STAFF MEMBER AND PARTICIPANTS

Aagaard, Knut	University of Washington, Seattle
Browand, F. K.	University of Southern California, Los Angeles
Bryan, Kirk	Princeton University
Foster, Theodore	University of California, Santa Cruz
Gill, Adrian	D.A.M.T.P., Cambridge, England
Gordon, Arnold	Lamont-Doherty Geological Observatory
Howard, Louis	Massachusetts Institute of Technology
Hunkins, Kenneth	Lamont-Doherty Geological Observatory
Killworth, Peter	D.A.M.T.P., Cambridge, England
Krishnamurti, Ruby	Florida State University
Malkus, Willem	Massachusetts Institute of Technology
Martin, Seelye	University of Washington, Seattle
McCartney, Michael S.	Woods Hole Oceanographic Institution
Neshyba, Steve	Oregon State University, Corvallis
Smith, J. D.	University of Washington, Seattle
Stern, Melvin	University of Rhode Island
deSzoeka, Roland	Oregon State University, Corvallis
Turner, J. Stewart	Australian National Univ, Canberra
Veronis, George	Yale University
Welander, Pierre	University of Washington
Whitehead, John A.	Woods Hole Oceanographic Institution

FELLOWS

Hua, Bach-Lien	University of Paris
Keffer, Thomas	Oregon State University
Lemke, Peter	Max-Planck Institut fur Meteorologie
Martinson, Douglas	Columbia University
Moritz, Richard E.	Yale University
Roisin, Benoit	Florida State University
Rudels, Bert	University of Gothenburg
Talley, Lynne D.	WHOI/MIT Joint Program
Topham, David R.	Institute of Ocean Sciences, B.C., Canada

PARTICIPATING WHOI STAFF

Bryden, Harry	Schmidt, Ray
Joyce, Terrence	Voorhis, Arthur
Rhines, Peter	

VISITORS

Baines, Peter	C.S.I.R.O., Australia
Gascard, J. C.	Laboratoire d'Océanographie Physique, Paris
Hide, Raymond	GFD Meteorological Office, England
Shepherd, John	Lamont-Doherty Geological Observatory
Spiegel, Edward	Columbia University
Sugimoto, Takashige	Tohoku University, Sendai, Japan

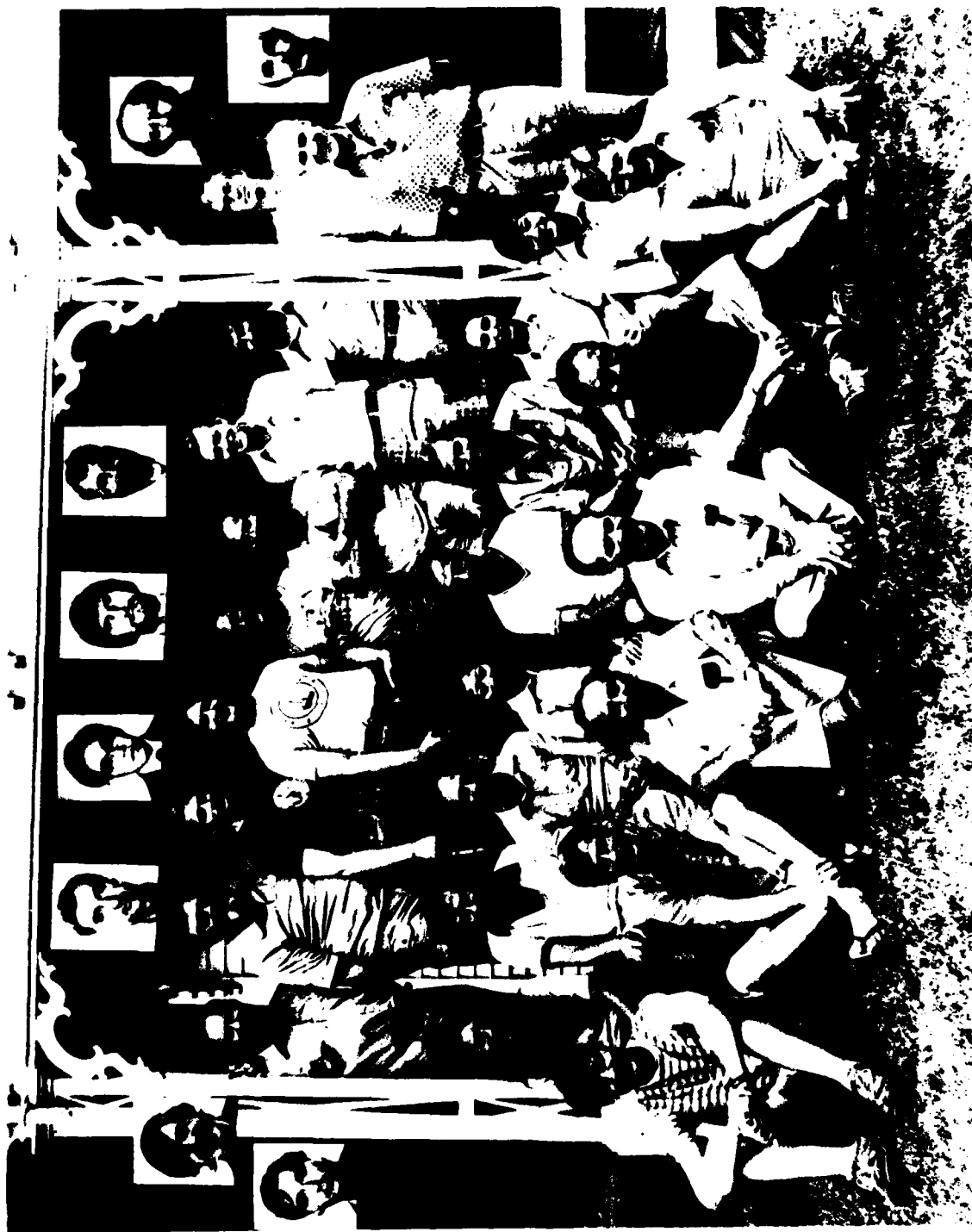
EDITOR'S PREFACE
VOLUME II

↓ This volume contains the manuscripts of research lectures by the nine fellows of the summer program. Some reports are obviously related to the main theme; some are related to crucial physical processes in the Polar Oceans; some are pure fluid dynamics or related to particular educational goals of the fellows.

These lecture reports have not been edited or reviewed in a manner appropriate for published papers, but we hope that several of them have the beginnings of an idea which will eventually find its way into the literature. Therefore, readers who wish to reproduce any parts of these Unpublished Manuscripts[†] should seek permission directly from the authors.

Seven of the fellows were supported by ONR, NASA and NOAA. One of the fellows was supported by The West German Government through the Max Plank Institute for Meteorology, and one of the fellows was supported by the Canadian Government through the Institute of Ocean Sciences. ↗

Melvin E. Stern



Gascard Killworth Foster Sugimoto DeSzoeko Smith Gordon Hunkins

Top row: Armi, Browand, Rudels, Martinson, Lemke, McCartney, Howard, Baines, Malkus, Hyde;
 Middle row: Hua, Topham, Gill, Krishnamurti, Veronis, Keffer, Talley, Roisin;
 Front row: Moritz, Bryan, Stern, Neshyba, Martin, Whitehead.

Contents of Volume I: Course Lectures, Seminars, and Abstracts of Seminars

CONTENTS OF VOLUME II
Lectures of the Fellows

	Page No.
Penetrative Convection: Modelling with Discrete Convecting Elements Benoit Roisin	1
Penetrative Convection Behind a Moving Horizontal Temperature Discontinuity Richard Moritz	29
A Laboratory Model of Chimney Instability Thomas Keffer	63
A Model for the Seasonal Variation of the Mixed Layer in the Arctic Ocean Peter Lemke	82
Steady Two-Layer Source-Sink Flow Lynne Talley	97
A Study of Thermal Convection in a Rotating Annulus with Applied Wind Stress and Surface Velocity David Topham	119
Cycling Polynya States in the Antarctic Douglas G. Martinson	149
Experiment with Double Diffusive Intrusions in a Rotating System Bert Rudels	176
Boundary Density Currents of Uniform Potential Vorticity Bach-Lien Hua	197

PENETRATIVE CONVECTION: MODELLING WITH DISCRETE CONVECTING ELEMENTS

Benoit Roisin

Introduction

The atmospheric tropopause, the oceanic thermocline and the solar photosphere are dynamic processes controlled by the heat flux through them. On one side of these transition regions heat is carried by turbulent convection. On the other side, radiation, conduction, or steady advection is responsible for the flux. The position, thickness and mean structure of these regions depend upon the balance struck between the penetrating convection and the competing heat flux mechanism. Moreover, entrainment may or may not be superimposed on the structure.

It is worthwhile to state here the distinction between penetration and entrainment. The penetration layer is the zone where the convective heat flux is decreasing, progressively replaced by conduction, any other heat transfer mechanism, or used to change the temperature of the medium, the fluid being itself the sink of all heat. The penetration layer is mainly characterized by its thickness and structure. It may be steady, or changing with time, in which case entrainment occurs; the entrainment is therefore characterized by a velocity of progression of the penetration into the stable fluid. If the convective region narrows, we may speak of detrainment. The steady situation of water cooled below 4°C on its bottom (Malkus, 1963; Moore and Weiss, 1973) is a case of penetration without entrainment, while the deepening of a sharp thermocline (Turner, 1967; Pollard, Rhines and Thompson, 1973; Heidt, 1977) is one of entrainment and penetration.

Modelling by Discrete Convecting Elements: the Thermals

In this work, the convection is modelled by the motion of thermals, convecting elements of fluid particles at a temperature different from the surroundings. The convective heat flux is partly carried by the fast moving thermals and partly by the slow return flow of the surroundings. The buoyant thermals are accelerated, mix with the ambient fluid and may also mix with one another, until they reach the neutral level where they are not longer buoyant. Because of their non-zero velocity at that level and their inertia, they overshoot their equilibrium position and are progressively slowed down. In view of that mechanism, the penetration layer is that latter region extending from the neutral level to the position of vanishing velocity. One might fear that still because of their inertia, the thermals oscillate back and forth until their motion is damped by mixing or viscosity. In reality, as one may observe in clouds, for instance, the thermals are critically damped; i.e., when their velocity first vanishes, they lose their identity and mix with the surroundings. In this work, we will assume with Manton (1975) that the fraction f of the area at any level occupied by thermals is constant. This leads to the proportionality between the velocity and the volume of the convecting elements, such that when the velocity vanishes so does the volume. Therefore, the thermals lose their identity after only one overshooting.

The penetration strongly depends upon the structure of the adjacent stable region as well as upon the way the thermals carry heat. Is the heat carried by a few fat thermals of low temperature contrast or by many small thermals of high temperature contrast? Are the thermals moving fast or slowly? The answer to these questions is found by analyzing the thin unstable region near the boundary where the thermals are formed, as well as their travel

throughout the convective layer. But this is the subject of another work. Roughly, we may say that the solution of that problem yields the boundary conditions at the entrance of the penetration layer in terms of velocity, volume and flux of thermals, as functions of a Rayleigh number and the forcing of the system.

Equations for Thermals

The thermals are characterized by their velocity w , their volume V , their temperature T' as well as the number n of those which flow through a horizontal plane per unit area and unit time. The environment is only characterized by its return velocity w_e and temperature T_e . The resulting averaged temperature \bar{T} we may observe is a combination of T' and T_e . Moreover, we introduce the fraction f of the area at any level occupied by convecting elements (Manton, 1975). According to that definition, the product fw represent the flux of volume of thermals at any level, which is obviously equal to nV so that:

$$fw = nV \quad (1)$$

The fraction of the area available for the return flow is $1-f$ and continuity requires

$$(1-f)w_e + fw = 0 \quad (2)$$

It also follows that the averaged temperature T is given by

$$\bar{T} = (1-f)T_e + fT' \quad (3)$$

The convective part of the heat flux (divided by ρc , as usual) is the correlation \overline{wT} , i.e.,

$$H_{\text{conv}} = \overline{wT} = fwT' + (1-f)w_e T_e$$

or, using (2),

$$H_{\text{conv}} = fw(T' - T_e) \quad (4)$$

Using (1), the part of H_{conv} due to the thermals may be also written as

$$nVT'$$

the product of the heat content of one thermal VT' and the number n of thermals flowing per unit time and area. This could have been another way to establish (4).

To be complete, the description must include an equation of motion for w , an equation predicting the change in T' due to changes in volume, as well as a closure hypothesis telling how the volume changes by mixing or leakage processes.

Equation of Motion

Contrary to Turner (1973), we assume that the environment may be considered a source or sink of momentum such that a change in volume does not lead to any change of momentum of the elements, the environment accounting for such changes. Turner (1973) assumed that the environment may not gain or lose any momentum from the elements. The reality lies in between. With our hypothesis, in an Eulerian frame $\left(\frac{d}{dt} = w \frac{\partial}{\partial z}\right)$, the equation of motion reads:

$$wV \frac{\partial w}{\partial z} = V\alpha g (T' - T_e) \quad (5)$$

where V does not appear behind the operator $\frac{\partial}{\partial z}$. In the case of water over ice, the non-linearity of the equation of state leads us to replace $T' - T_e$ by $T' - T^2$ if the temperatures are referred to 4°C .

We have to be aware that equation (5) is also based on other assumptions. Firstly, the Boussinesq approximation is made and viscosity is neglected. Then, all the thermals are supposed to be identical, such that there are not extra terms due to the underlying averaging process. Finally, in a non-steady state, the sinking time of the thermal is assumed to be small compared to the evolution time scale of the system, such that there is no $\frac{\partial w}{\partial t}$ term.

Equation for Temperature

If the element entrains some environmental fluid, its temperature will tend to T_e according to the law $\left(\frac{d}{dt} = w \frac{\partial}{\partial z} \right)$:

(6)

$$w \frac{\partial}{\partial z} (VT') = T_e w \frac{\partial V}{\partial z} .$$

But on the other hand, if the element loses mass, its temperature remains unchanged:

$$T' = \text{constant} \quad (7)$$

Closure Hypothesis

In the case of the convection below the atmospheric inversion (Manton, 1975), the value of f ranges between 0.45 and 0.5, although extreme values of 0.33 and 0.6 may be encountered. For the oceanic mixed layer, we did not find corresponding values of f in the literature, but the same narrow range seems likely.

With Manton (1975), we assume that the fractional area f is constant. This means that after an isotropic expansion period, the thermals begin to

feel the presence of one another in such a way as to keep constant the available surface for the return flow. Therefore we write:

$$f = nV = \text{constant} \quad (8)$$

This closure hypothesis has the advantages that no new parameter is introduced (everything may be determined by the upstream conditions) and a diagnostic equation is obtained. An immediate consequence of (8) is that since no thermals are created nor lost at any level ($n = \text{constant}$), the volume is proportional to the velocity. In the convection region, the velocity increases and so does the volume, implying that (6) must be used there to predict T' . But, in the penetration layer, where the velocity decreases, the volume diminishes in proportion and (7) must be used.

The Case of Water Cooled Below 4°C on its Bottom

A typical example of penetrative convection is the one of a horizontal layer of water cooled below 4°C on its bottom surface. The density maximum admits two layers: a top stably stratified layer (above 4°C) and a bottom convective layer (below 4°C). Experiments were carried out by Furumoto and Rooth (1961). Simple insight, confirmed by the experiments, reveals that convecting elements may overshoot the density maximum and penetrate the stable layer to some extent, creating a penetration zone. The system is driven by the temperature difference across the layer, and if this forcing is kept constant, a steady state takes place (no entrainment). The mean temperature profile is distorted (Fig. 1): the initially stable region is deeply penetrated by the denser water, and is compressed until the temperature gradient is sufficient to produce the heat flux required for a steady state in the entire layer; the convective region is nearly homogeneous, limited on its top by the

penetration layer and on its bottom by the intermittent, unstable layer where the thermals are generated. The stability and initial finite amplitude behavior of this system have been studied by Veronis (1963). Using the stability criterion and the property of constant heat flux throughout the layer, Malkus (1963) determined the ratio of the depth of the convective region to the total layer thickness, and the Nusselt number, as functions of a Rayleigh number. Moreover, making some assumptions, he was also able to determine the thickness of the penetration layer as well as its temperature profile. His assumptions and results will be compared to the present attempt. Moore and Weiss (1973), extending Malkus' first results, used global arguments and showed that for Rayleigh numbers close to, but less than the critical value, two regimes are equally likely, pure conduction or convective regime. As one might expect, between two stable regimes exists an unstable one, and so a third solution is found (another but less active convective regime). A criterion of stability is built which easily leads to the instability of the intermediate solution and to the stability of the subcritical convective regime. The authors also built a non-linear numerical model for a two-dimensional cell of given geometry, and compared their results.

Our interest here is not in the global heat flux relationship but in predicting the thickness and the structure of the penetrative region.

The model of Malkus (1963) pictures the convective elements reaching the top of the convective layer with an r.m.s. vertical velocity w and a mean temperature excess δT , such that

$$H_{\text{conv}} = \overline{wT} = w \delta T \quad (9)$$

Assuming a non-dissipative rising motion, T does not change through the layer, it will also be considered small. As thermals penetrate, more and more of the constant heat flux is taken over by conduction, the total heat flux reads:

$$H = -\kappa \frac{\partial T_e}{\partial z} + w \delta T \approx H(z) \quad (10)$$

with, at the bottom,

$$H = w_{\max} \delta T \quad (\text{pure convection}) \quad (11)$$

and at the top,

$$H = -\kappa \frac{\partial T_e}{\partial z} \quad (\text{pure conduction}) \quad (12)$$

The deceleration of the conservative convective element in the environment, T_e , is given by the Boussinesq relation:

$$w \frac{\partial w}{\partial z} \approx -\alpha g T_e^2 \quad (13)$$

when $\delta T \ll T_e$ (All the temperatures are measured from 4°C).

Eliminating δT by the use of (11), considering the heat flux as given, Eqs. (10) and (13) constitute a set of two equations for two unknowns T_e and w .

On the other hand, our assumptions lend to (4) and (5), i.e.

$$H = -\kappa \frac{\partial T_e}{\partial z} + f w (T' - T_e) \quad (14)$$

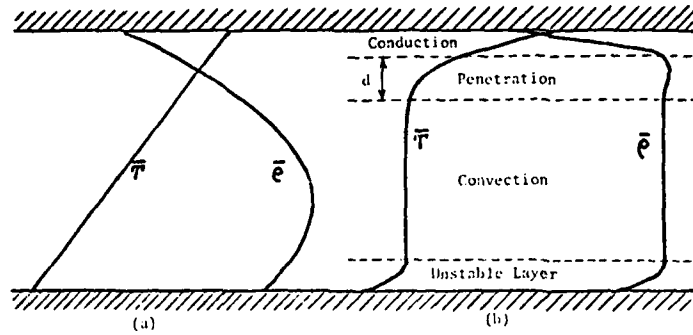


Fig. 1. Temperature and density profiles. (a) Conduction only.
(b) Penetrative convection.

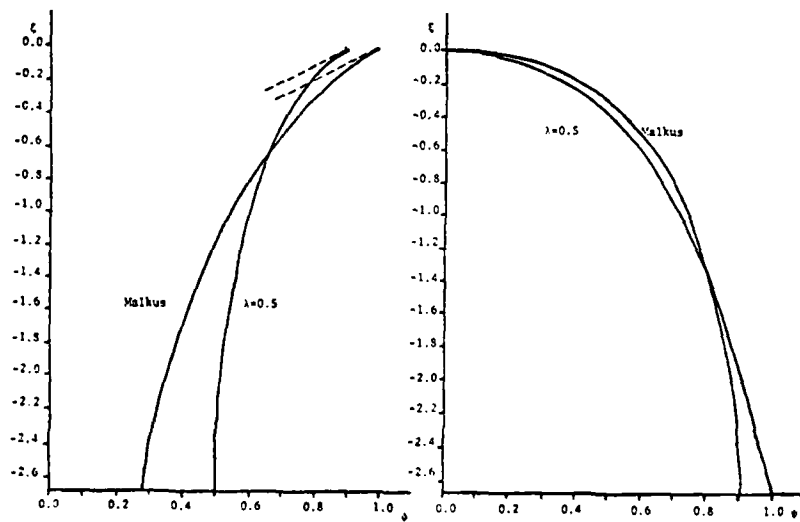


Fig. 2. Temperature and velocity profiles for the two models.

$$w \frac{\partial w}{\partial z} = \alpha g (T'^2 - T_e^2) \quad (15)$$

where H, F and T' are constants related by $H = f_{\max} (T' - T_e(0))$. This constitutes another more accurate system for the same two unknowns.

The scaling of the above sets of equations leads to a scale for the thickness d of the penetration layer. Indeed, let us scale the vertical velocity w by its initial maximum value w_{\max} , the environment temperature T_e by T_1 the order of magnitude of the unknown temperature at the top of the layer, and the coordinate z by the unknown scale thickness d:

$$\psi = \frac{w}{w_{\max}}, \quad \phi = \frac{T_e}{T_1}, \quad \xi = \frac{z}{d} \quad (16)$$

The pure conductive process at the top of the layer requires, by using (10) or (14)

$$|H| = \frac{\kappa T_1}{d} \quad (17)$$

while the balance of (13) or (15) yields:

$$\frac{w_{\max}^2}{2d} = \alpha g T_1^2 \quad (18)$$

Eliminating T_1 , between the two previous relationships, a scale for d is found to be

$$d = \left(\frac{\kappa^2 w_{\max}^2}{2\alpha g |H|^2} \right)^{1/3} \quad (19)$$

The dimensionless equations now read:

Malkus' model

$$1 = \phi' + \Psi \quad (20)$$

$$(\Psi^2)' = -\phi^2 \quad (21)$$

Present model

$$1 = \phi' + \frac{\Psi}{\lambda} (\lambda - \phi(0) + \phi) \quad (22)$$

$$(\Psi^2)' = (\lambda - \phi(0))^2 - \phi^2 \quad (23)$$

where the prime means a derivative with respect to ξ and where

$$\lambda = \frac{\kappa}{f d w_{\max}} = \frac{T_e(0) - T_i}{T_i} \quad (24)$$

represents the non-dimensional initial temperature difference. The boundary conditions at the bottom of the layer are:

$$\begin{aligned} w &= w_{\max}, \quad T_e = T_e(0), \quad \text{as } z = 0 \\ \text{i.e.,} \quad \Psi &= 1, \quad \phi = \phi(0), \quad \text{as } \xi = 0 \end{aligned}$$

$T_e(0)$ and hence $\phi(0)$ are to be chosen such that the vertical velocity decreases starting at the bottom of the layer. Malkus chose $\phi(0) = 0$ so that the deceleration is first infinitesimal, requiring an infinite space for Ψ to drop to zero. In other words, his solution is boundary-layer-like. Since the equations in that case are simpler, an integral constraint may be

found which leads to $\psi = 1$ where Ψ vanishes (top of the layer) and therefore a numerical backward integration is possible. The numerical solution is plotted on Fig. 2.

In the present model, an integral constraint leading to the value of ψ where Ψ vanishes was not found and a backward integration was impossible. For that reason, we have chosen to integrate forward starting with $\psi(0) = \lambda$. This means that the thermals have a zero temperature T' and are thus at the density maximum. The value ξ_1 of ξ where Ψ vanishes yields the depth of penetration in units of d ; the value ψ_1 of ψ at that level gives the top temperature. The solution for $\lambda = 0.5$ is plotted on Fig. 2 for comparison with Malkus' solution. Table 1 gives some values of ξ_1 and ψ_1 for different values of λ .

Measure of the Initial Temperature Difference	Thickness Scaled by d	Top Temperature Scaled by $(H d) / \kappa$
λ	ξ_1	ψ_1
1.0	0.8728	1.2372
0.5	2.683	0.9018
0.1	50.75	0.4735
0.05	200.6	0.3589

TABLE 1. Values of the penetration thickness, and the temperature at the top of the layer.

For small values of λ , near the bottom of the layer, the term is negligible in (22) and we get an asymptotic solution

$$\xi \approx \frac{1 - \psi^4}{2\lambda^2}, \quad \psi \approx \frac{\lambda}{\Psi}.$$

The first relation seems to hold all across the layer and allows us to find the value of ξ_1 for small λ : when Ψ vanishes, we get:

$$\xi_1 \approx \frac{1}{2\lambda^2} \quad (25)$$

which is in perfect agreement with the previous numerical solutions. This shows that when λ is small, ξ_1 is no longer of order one and the variables must be rescaled. In that case, the thickness of penetration appears to be:

$$\text{thickness} = \frac{d}{2\lambda^2} = \frac{w_{\text{max}}^2}{4\sigma g T_e^2(0)} \quad (26)$$

which increases if λ , i.e., $T_e(0)$, decreases. This is understandable since a small $T_e(0)$ implies fast moving thermals of low heat content which penetrate deep into the stable region.

While there is no value of λ for which the two models are identical, the value $\lambda = 0.5$ leads to close profiles. The velocity profile is very similar except that, for the present model, Ψ equals one for a finite value of ξ_1 (-2.683 from the top). The curves of temperature differ, the present model leading to a smaller temperature difference across the layer.

The advantage of the new calculations is to show that there is no universal profile of temperature, nor of velocity, but rather a series of profiles depending upon the manner in which the convective elements hit the stable region. The bottom instability of the convective layer selects the structure. It also shows that for fast-moving elements the penetration becomes very deep, and that a new scaling is necessary.

The Case of Ocean Surface Cooling

During the Fall and Winter, when the ocean surface is cooled instability and convection occur. A mixed layer is formed, penetrating in the stable stratification below. This mixed layer, contrary to the diurnal thermocline formation, is generally very efficient and may mix, in some cases, the top 500 m of the water column. The wind stirring may play an important role at the start but rapidly convection dominates the processes, supplying, by itself, the kinetic energy required for stirring and deepening. In this present attempt, we will therefore ignore the wind effect. At the bottom of the mixed layer is the penetration layer; this layer too, deepens with time and entrainment is present. In this case molecular conduction of heat is not important and, in the penetration layer, the convective heat flux is progressively consumed for changing the temperature of the water. Our interest is again in predicting the thickness and the structure of the penetration layer, by modelling the convection by thermals sinking from the surface down to the stable fluid. The situation may be depicted as on Fig. 3.

Apart from a thin unstable layer near the surface, the mixed layer of depth h is considered of homogeneous temperature T_0 . This layer is progressively cooled and thus leads to a linear decrease of the heat flux from its imposed surface value Q ($Q > 0$ for cooling). In the unstable layer, convective elements are produced with a temperature T' ; during their sinking motion they gradually mix with their environment and T' becomes closer to T_0 . When the temperature profile curves, the temperature will first equal and then exceed the environmental temperature, there noted by T_e . Where $T' = T_e$, almost at the top of the penetration layer, the convective heat flux is exactly zero, according to (4). In the penetration layer, the convective

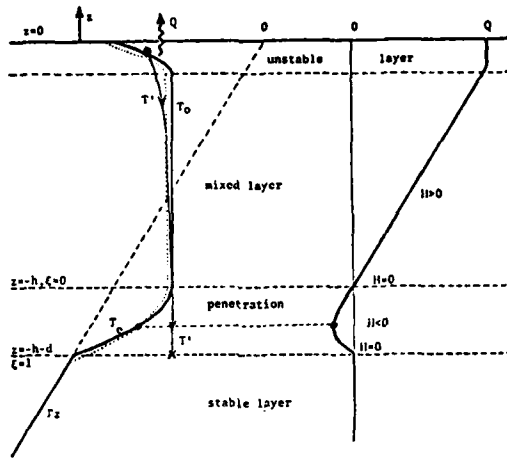


Fig. 3. Schematic diagram of the temperature and heat flux profiles in case of penetration in a stable ocean by surface cooling.

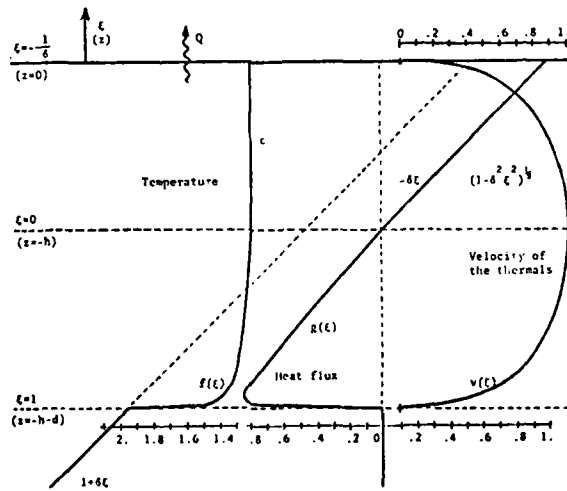


Fig. 4. Temperature, heat flux and vertical velocity profiles for $s=0.1$;

$$\delta = 1.0647$$

$$\epsilon = 1.324$$

$$\lambda = 41.2$$

elements are warmer than their surroundings, the heat flux is therefore downward (negative) and they decelerate. The time scale of the entrainment process is much greater than the time required for an element to sink all the way down. We may therefore assume that an element sees a steady temperature profile and stops exactly at the bottom of the penetration layer. According to (4), the convective heat flux, there again is zero. If we neglect the conduction, the heat flux exhibits the profile shown on Fig. 3, with a negative minimum value inside the penetration layer.

The heat conservation equation is:

$$\frac{\partial T_e}{\partial t} = - \frac{\partial H}{\partial z} \quad (27)$$

and tells us that above the minimum value of H the temperature decreases while beneath the minimum it increases with time. A short time after, the temperature profile will look like the dotted profile on Fig. 3. Somewhere in the penetration layer, T_e did not change. Of course that level deepens with time, allowing every level of fluid to be cooled after a short time of heating.

Above the intersection point of the T' and T_e profiles, the convective elements are denser than their environment. They thus accelerate and mix with the surroundings, equations (6) and (8) hold. Below that point, the elements are less dense and decelerate; there equations (7) and (8) are to be used; the temperature T' is therefore constant, approximately equal to T_0 (see Fig. 3). In the present model we will assume that the changes in temperature follow the deepening, having in mind the search of a similarity solution. We note

$$T_0 = T' = -\epsilon \Gamma h \quad (28)$$

$$T_e = -\Gamma h f\left(\frac{z}{h}\right) \quad (29)$$

where Γ is the temperature gradient in the stable layer, ϵ a pure number to be determined by the model, $f(\xi)$ an unknown function of the similarity coordinate through the penetration layer (see Fig. 3).

$$\xi = - \frac{z+d}{d}$$

$\xi = 0$ at the top of the layer

$\xi = 1$ at the bottom of the layer

must match the temperature profiles above and below the penetration layer, i.e.,

$$f(0) = \epsilon, \quad f(1) = 1 + \frac{d}{h}. \quad (30)$$

For similarity to be used, the last condition requires that d grow in time as h does. We therefore note:

$$d = \delta h \quad (31)$$

where δ is a second pure number to be determined by the model.

Firstly, a few properties inside the mixed layer will be deduced to help to solve the penetration dynamics. Then, the equations for the penetration will be established, an integral constraint, found, and a numerical solution presented. Finally, an analytical solution will be given for the case of strong initial stratification, and this solution will be compared to the model of Krauss and Turner (1967).

A Few Properties Inside the Mixed Layer:

In the mixed layer the temperature T_0 is z -independent and the heat conservation equation (27) may thus be integrated to find the heat flux:

$$H = Q - z \frac{dT_0}{dt} \quad (32)$$

where Q is the surface value considered as the forcing of the system. Using

(28) and the fact that H vanishes at the bottom of the mixed layer ($z = -h$), we get:

$$Q = \epsilon \Gamma h. \quad (33)$$

If Q may be considered constant and if h is initially zero, we may integrate and find h at any time, provided that ϵ is known.

We neglect any conduction, assuming it plays a negligible role in the entrainment process. The definition of the heat flux (4) and the equation of motion (5) may be solved with the use of (32) and (33) to get:

$$w^3 = w^3(z=0) + \frac{3\epsilon N^2 h}{2f} (2hz + z^2)$$

$$T' = -\epsilon \Gamma h + \frac{\epsilon \Gamma h (h+z)}{f \left\{ w^3(z=0) + \frac{3\epsilon N^2 h}{2f} (2hz + z^2) \right\}^{1/3}}$$

where $N^2 = \alpha g \Gamma$ is the Brunt-Vaisala frequency in the stable layer. For a mixed layer deep enough, at the bottom of the layer the value w ($z=0$) has no effect, and we get

$$w(-h) = - \left(\frac{3\epsilon N^2 h^2}{2f} \right)^{1/3} \quad (34)$$

$$T'(-h) = -\epsilon \Gamma h. \quad (35)$$

The latter relationship is a repetition of (28) and gives the temperature T across the penetration layer.

The Similarity Equations For the Penetration Layer:

We introduce in place of T_e , H and w the similarity functions $f(\xi)$, $g(\xi)$ and $v(\xi)$ such that:

$$\begin{aligned} T_e &= - \Gamma h f(\xi) \\ H &= - Qg(\xi) = - \epsilon \Gamma h \dot{h} g(\xi) \\ w &= - h N v(\xi) \end{aligned} \quad (36)$$

and we also introduce a dimensionless measure of the underlying stratification:

$$\lambda = \frac{f h N}{h} \quad (37)$$

The equations (4), (5) and (27) yield:

$$\epsilon g(\xi) = \lambda v(\xi) \{ f(\xi) - \epsilon \} \quad (38)$$

$$-v(\xi) v'(\xi) = \delta \{ f(\xi) - \epsilon \} \quad (39)$$

$$\{ (1 + \delta \xi) f(\xi) \}' - 2 \delta f(\xi) = -\epsilon g'(\xi) \quad (40)$$

The boundary conditions are:

- at the top:

$$\begin{aligned} \xi = 0 \quad f(0) &= \epsilon \\ v(0) &= \left(\frac{3\epsilon}{2\lambda} \right)^{1/3} \\ g(0) &= 0 \end{aligned} \quad (41)$$

- at the bottom

$$\begin{aligned} \xi = 1 \quad f(1) &= 1 + \delta \\ v(1) &= 0 \\ g(1) &= 0. \end{aligned} \tag{42}$$

According to (38), the two conditions on $g(\xi)$ are redundant. Equation (38) is algebraic; the system is of second order and required only two boundary conditions. We are thus left with two extra conditions, precisely those which will enable us to determine ϵ and δ . The problem is therefore closed and self-consistent.

Replacing $f(\xi)$ by its expression from (39) into (40), we may integrate with respect to ξ and use the top boundary conditions (41):

$$(1 + \delta\xi)f(\xi) - \epsilon - 2\epsilon\delta\xi + v^2 - \left(\frac{3\xi}{2\lambda}\right)^{2/3} + \epsilon g(\xi) = 0. \tag{43}$$

Using the bottom boundary conditions (42), we obtain a relationship between and .

$$\delta^2 + 2(1 - \epsilon)\delta + (1 - \epsilon) - \left(\frac{3\xi}{2\lambda}\right)^{2/3} = 0. \tag{44}$$

This is an integral constraint. It may be shown that it is identical to the global heat budget of the system: the amount of heat lost at the surface was used to cold the fluid from its initial stratification to its present state:

$$\int_0^t Q dt = \int_{-h-d}^0 (\Gamma z - T_e) dz.$$

On the other hand, looking at the conversion of potential to kinetic energy we are led to consider the integral

$$\int_{-h-d}^0 \overline{wT} dz = \int_{-h-d}^0 H dz$$

The computations reveal that the integration across the mixed layer exactly balances the integration across the penetration layer, leading to a net zero global conversion. This is understandable: since the model is conservative (inviscid and nonconducting), the potential energy in the mixed layer is given to the accelerating thermals and recovered in the penetration layer where the thermals decelerate. Because there is no conversion, no dissipation and no energy impact from the wind, the total kinetic energy in the system is conserved. But, the kinetic energy in the mixed layer always increases with time.

From (38) and (39), we may express $g(\xi)$ and $f(\xi)$ in terms of $N(\xi)$. Replacing in (43), we end up with a single first-order nonlinear differential equation:

$$\frac{1 + \delta \xi}{2\delta} \frac{dv^2}{d\xi} - v^2 + \left(\frac{3\varepsilon}{2\lambda}\right)^{2/3} + \varepsilon \delta \xi + \frac{\lambda}{3\delta} \frac{dv^3}{d\xi} = 0. \quad (45)$$

A Numerical Solution

If we were able to solve analytically that equation by using the top boundary condition on v , we could find the second relationship between ξ and δ by using the bottom boundary condition on v . But this is not the case and the problem must be addressed in a different way if we want to find a

numerical solution. For that purpose let us note:

$$v = \left(\frac{3\epsilon}{2\lambda}\right)^{1/3} u(\xi) \quad (46)$$

$$\eta = \delta \xi \quad (47)$$

$$s = \frac{1}{\epsilon} \left(\frac{3\epsilon}{2\lambda}\right)^{2/3} \quad (48)$$

and the problem becomes:

$$s \left\{ \frac{1}{2} (1 + \eta) \frac{du^2}{d\eta} + 1 - u^2 \right\} + \eta + \frac{1}{2} \frac{du^3}{d\eta} = 0 \quad (49)$$

with

$$u = 1 \quad \text{as } \eta = 0 \quad (50)$$

$$u = 0 \quad \text{as } \eta = \delta . \quad (51)$$

The coefficient s contains the unknown ϵ and the known λ . Let us assign a value to s , and set λ free, so that we may solve (49) with the aid of (50). The value δ of η where u vanished will be given by the numerical

solution. Going back to the integral constraint (44) transformed into

$$\delta^2 + 2(1 - \epsilon)\delta + (1 - \epsilon) - (\epsilon s)^{1/2} = 0 \quad (52)$$

we solve for ϵ . Finally, the definition of s will tell us for which value of λ the solution was found.

Calculations were carried out for the value $s = 0.1$. The solution as well as the analytical solutions for the mixed layer are shown on Fig. 4. The penetration layer is found as thick as the mixed layer (δ very close to one) but the variation in temperature and heat flux are concentrated near the bottom of the layer. This might be surprising but will be understood in light of the analytical solution for the asymptotic case of strong underlying stratification.

The Case of Strong Underlying Stratification

According to (37) and (48), strong stratification in the stable layer (large Brunt-Vaisala frequency) leads to a small value of s . (A small rate of entrainment \dot{h} leads to a small value of s , too). The present paragraph is devoted to finding an asymptotic analytic solution for s close to zero.

For $s = 0$, equation (49) joined to $u(\eta = 0) = 1$, yields the solution

$$u^3 = 1 - \eta^2 \quad (53)$$

which is, by the way, exactly the solution in the mixed layer. The solution leads to an unbounded bracketed quantity in (49) near $\eta = 1$. We have thus to consider a boundary layer near $\eta = \delta$, anticipating that δ is close to unity. Scaling arguments show that in the boundary layer, u is of order s

and $\delta - \eta$ of order s^3 . The solution satisfying $u(\eta = \delta) = 0$ is found to be:

$$u^3 + s(1 + \delta)u^2 = 2\delta(\delta - \eta). \quad (54)$$

This solution for increasing u and $\delta - \eta$ must match the interior solution (53) for small u and $\delta - \eta$. The matching implies

$$\delta = 1 \quad (55)$$

and the two solutions may be combined to yield a simple expression valid throughout the layer to order s :

$$u^3 + 2su^2 = 1 - \eta^2. \quad (56)$$

The use of the integral constraint (52) gives, to first order

$$\epsilon = \frac{4}{3} - \frac{2}{3} \left(\frac{\xi}{3} \right)^{1/2} \quad (57)$$

and therefore the solution is found for large values of λ given by

$$\lambda = 2 \left(\frac{3}{4s} \right)^{3/2} \quad (58)$$

Back to the initial variables, the solution reads:

$$\lambda v^3 + 3v^2 = 2(1 - \xi^2) \quad (59)$$

$$f = \frac{4}{3} \left(1 + \frac{\xi}{\lambda v + 2} \right) \quad (60)$$

$$g = \frac{\xi}{1 + \frac{z}{\lambda v}} \quad (61)$$

The thickness of the boundary layer was found to be s^3 in units of η . Back to the variable z , the actual thickness is (without a factor 27):
16

$$t = \frac{h^2}{f^2 h N^2} \quad (62)$$

inversely proportional to N^2 . The larger the underlying stratification, the thinner the boundary layer and the sharper the transition between penetration and stable fluid.

The thickness t is to be considered as the thickness of the thermocline. So, by this model we are led to establish a distinction between penetration layer and thermocline. The penetration is a layer as thick as the mixed layer, and is usually incorporated in the latter from a double layer, the so-called "mixed layer". The thermocline, on the other hand, is a thin region of large transition, the front of the penetration.

It is worthwhile to confront the solution of Krauss and Turner (1967) with the present asymptotic case. They model the "mixed layer" as homogeneous bounded below by an infinitely sharp thermocline. Their model contains two unknowns: the depth h of the mixed layer and its temperature T_0 . The first equation they use is identical to (32). To form their second equation they

write the mechanical energy balance:

$$\frac{d}{dt}(\text{KE}) = \sigma g \rho \int_{-h}^0 w T dz + G - D$$

rate of change of kinetic energy conversion from potential energy kinetic energy input from wind dissipation

The left-hand side is mysteriously set equal to zero, and the balance is struck among potential energy, wind action and dissipation. To compare to our case, set G and D to zero. Their model, therefore, leads to $\int_{-h}^0 w T dz = 0$, what we previously found from our model. Therefore, in both models, the basic equations used are the same apart from the fact that our model justifies $\frac{d}{dt}(\text{KE}) = 0$. However, the solutions differ because we work with a non-zero thickness of the thermocline. In the limiting case $N^2 \rightarrow \infty$, solutions are identical. The merit of our model is to show that in fact, a slight slope in the temperature profile is required in the bottom half of the "mixed layer" and that Krauss and Turner's mixed layer is divided in two: half pure mixed layer and a half penetration layer. The separation line is the zero heat flux level.

Beyond clearing up a classical paper and the justification of a zero heat flux level somewhere in the middle of the mixed layer, our model is also capable of predicting the structure of the penetration, the thickness and structure of the thermocline.

Conclusions

This modelling of convection by discrete thermals leads to a new approach for studying the effects of penetration as well as of entrainment. The model is closed by basic physical assumptions without introduction of any new empirical coefficient. After a general presentation of the modelling by

convective elements, the model was applied to steady and unsteady cases. In the study case of water cooled below 4°C on its bottom, the structure of the penetration was compared to a previous model (Malkus, 1963), and we pointed out the non-universality of that structure and its dependence upon the bottom instability. In the non-steady case of the mixed layer deepening, the model leads to a penetration layer as thick as the mixed layer. Therefore, the so-called mixed layer as we observe it has in fact a double structure and contains the pure mixed layer and the penetration layer. For a strong underlying stratification, the model predicts a sharp thermocline, front of the penetration layer.

This model is to be understood as a compromise between depth integrated models with an infinitely sharp thermocline (Krauss and Turner, 1967; Pollard, Rhines, and Thompson, 1973; Heidt, 1977), and more elaborate numerical models where the full partial differential equations are solved for a particular geometry (Moore and Weiss, 1973). By its situation of a compromise and its physical background (convective elements are actually observed), the model may be fruitful, especially if certain weaknesses are removed and improvements made.

Among the weaknesses are the assumptions of identical thermal elements and the absence of wind and shear effects. In the mixed layer deepening case, the assumption of crossing and profiles exactly where T_e starts to curve might be reconsidered. Indeed, in the limiting case of strong underlying stratification, the curvature of the T_e profile is trapped in the thermocline.

Among the possible improvements as starting points for a future work, we propose to relax the assumption of identical elements by introducing property

distributions and a statistical treatment. We also plan to investigate the generation of internal gravity waves in the penetration layer, and to study the case of a more general relationship between volume and velocity.

Acknowledgments

My sincere thanks go to Professor Malkus for suggesting to me the problem. His continuous guidance throughout this work is deeply appreciated. I am grateful to the Staff Members for giving me the chance to participate in the GFD summer program and for financial support.

REFERENCES

- Furumoto, A. and Rooth, C., 1961. Observations on convection in water cooled from below. Geophysical Fluid Dynamics, Woods Hole Oceanographic Institution, WHOI-61-39(3).
- Heidt, F. D., 1977. The growth of the mixed layer in a stratified fluid due to penetrative convection. Boundary Layer Meteorology, 12, 439-461.
- Krauss, E. B. and Turner, J. S., 1967. A one-dimensional model of the seasonal thermocline, II. Tellus, 19, 98-105.
- Malkus, W.V.R., 1963. A laboratory example of penetrative convection. Proc. 3rd. Tech. Conf. on Hurricanes and Tropical Meteorology, Mexico, 89-95.
- Manton, M. J., 1975. Penetrative convection due to a field of thermals. Jour. Atm. Sci., 32, 2272-2277.
- Moore, D. R. and Weiss, N. O., 1973. Nonlinear penetrative convection. Jour. Fluid Mech., 61, 553-581.
- Pollard, R. T., Rhines, P. B. and Thompson, R., 1973. The deepening of the wind-mixed layer. Geophysical Fluid Dynamics, 4, 381-404.
- Turner, J. S., 1973. Buoyancy effects in fluids. Cambridge Univ. Press, 367 p.
- Veronis, G., 1963. Penetrative convection. Astrophys. J., 137, 641-663.

PENETRATIVE CONVECTION BEHIND A MOVING,
HORIZONTAL TEMPERATURE DISCONTINUITY

Richard E. Moritz

I. Introduction

The motivation for this study comes from a desire to better understand the sea-to-air energy exchange processes over isolated openings (e.g. leads or polynyas) in an otherwise continuous canopy of sea ice. Given that a stably-stratified shear boundary layer comprises a typical upstream boundary condition, one is confronted with the problems of penetrative convection and shear turbulence in a horizontally-inhomogeneous internal boundary (IBL) (Venkatram, 1977). A simpler problem, requiring fewer assumptions and empirical parameters, is obtained by eliminating the effects of mean shear flow so as to isolate the problem of convective heat transfer due to buoyancy. While we may not expect quantitative agreement between the latter model and measurements in the pack ice (because the shear flow is undeniably crucial to heat fluxes in the real atmosphere), it is the author's opinion that the simpler problem is interesting in its own right and can provide insight into the more complete problem. A significant component of the physics is retained here, namely, the internal boundary layer processes associated with penetrative convection in an initially stable fluid. Moreover, a well-established theory for the heat flux is available, requiring only two empirical constants, both of which are known from careful laboratory experiments. Finally, a controlled laboratory simulation of our model IBL may be feasible, so that the conclusions might be subject to verification. In the next section we describe the simple convective system to be studied.

II. The Moving Temperature Discontinuity

Consider a two-dimensional "Boussinesq" fluid system in the (x,z) plane (Fig. 1). We assume that the fluid is at rest ($u,w = 0$) and is linearly stratified ($T(z) = T_0 + \gamma z$) at $x = +\infty$. Here T is the fluid temperature, γ is a constant vertical temperature gradient, (u,w) are the (x,z) velocity components and T_0 is the surface temperature at $x = +\infty$. The fluid is acted upon by a body force field $(0,g)$ and is completely characterized by its mean density ρ_0 , specific heat capacity (at constant pressure) c_p , thermal conductivity k , thermal diffusivity $\kappa = k/\rho_0 c_p$, molecular viscosity ν and thermal expansion coefficient α (all assumed constant). Hence our equation of state reads

$$\rho(T) = \rho_0 (1 - \alpha T') \quad (1)$$

where

$$T' \equiv T - T_0$$

$$\alpha = \left. \frac{1}{\rho_0} \frac{\partial \rho}{\partial T} \right|_{P_0, T_0}$$

and P_0 is a convenient reference pressure. Equation (1) corresponds to a linear decrease in density with height at $x = +\infty$ that can be characterized as hydrostatically stable by incorporating the assumed state of rest and the body force g into the z -momentum equation. Thus γ is our stability parameter. We imagine that the system is a half-plane, bounded at $z = 0$ by a smooth, perfectly conducting plate. At the moving coordinate $x = x_0(t)$ is maintained a step change in the temperature of the plate, such that $T(x,0,t) = T_0$ for $x > x_0$ and $T(x,0,t) = T_1 > T_0$ for $x < x_0$. This temperature discontinuity moves along the plate at constant speed $U = \dot{x}_0$ where ()

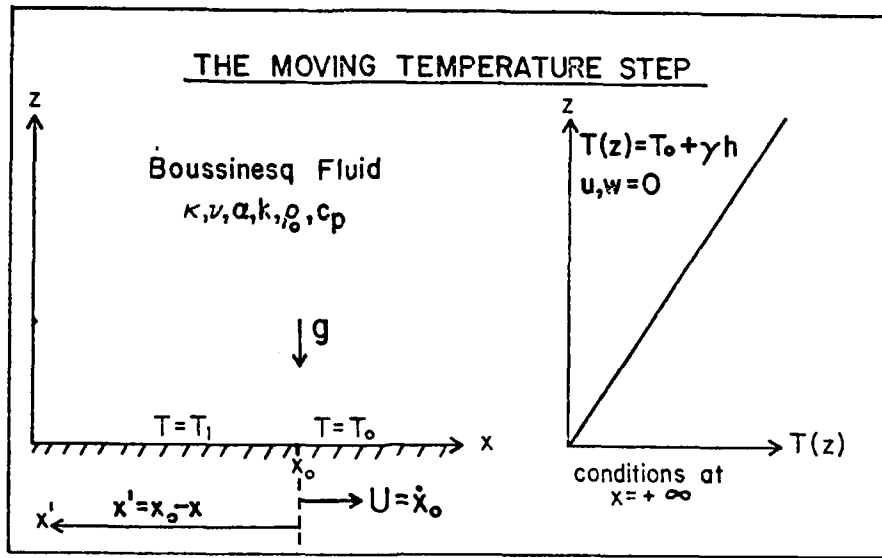


Fig. 1. The simple fluid system with a moving discontinuity in surface temperature.

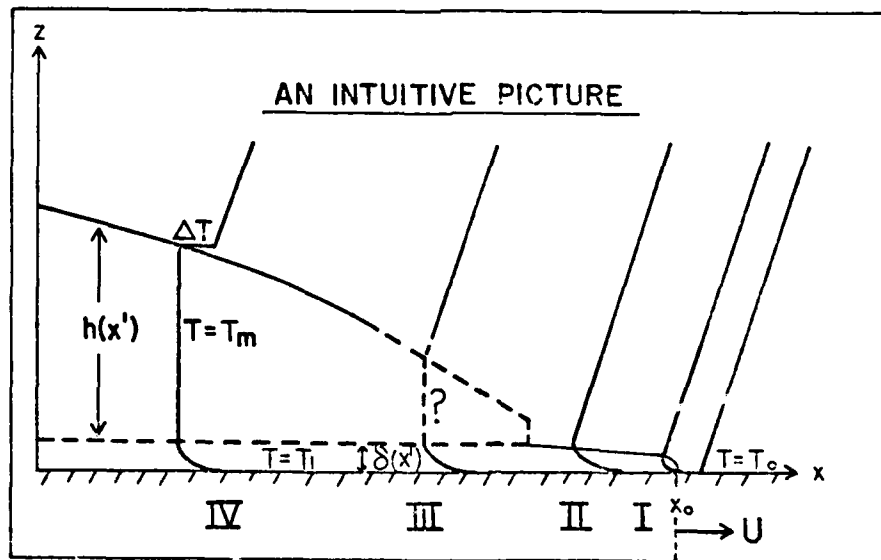


Fig. 2. Intuitive picture of four different regions in the wake of x_0 .

$= d(\quad)/dt$, and t is time. We emphasize that the plate is at rest relative to the undisturbed fluid ahead of x_0 , while the temperature step moves within the plate. In this manner we develop an IBL in the "wake" behind x_0 , free from viscous stresses other than those generated by the buoyancy effects of the temperature step. In the analyses that follow we shall make use of the coordinate $x' = x_0 - x$, giving the distance behind the advancing temperature step.

III. An Intuitive Picture of the "Wake" Region

Our intuition about the system leads us to expect an internal boundary layer whose form is sketched in Fig. 2. We emphasize that this heuristic picture needs justification, and scaling arguments to that effect are given in a later section. At the moment, however, we shall quickly outline our concept of the region immediately behind x_0 and then proceed directly to the convective region (IV in Fig. 2) where our main interest lies. The near-vertical sloping lines on Fig. 2 are schematic temperature profiles drawn in each of four distinct regions. The top edge of the IBL is denoted by the near-horizontal curve emanating from the point $(x_0, 0)$ and continuing to the left as the height $h(x')$ in region IV. Below this curve we expect the temperature profiles to differ substantially from the linear profiles at $x = +\infty$. Region I gives the appearance of a thermal diffusion "nose", wherein the conductive heat flux has significant x and z components. Ignoring for the moment the possibility of temperature advection due to motions generated by the horizontal pressure gradients in this nose region, we would expect the heat conduction to flatten the top edge of the boundary layer further back in the x' direction, where the conduction is mainly vertical (region II). Here we have a gravitationally unstable density (temperature) profile near the

plate, giving way to the linear, stable gradient γ above the edge of the IBL. Further behind the step x_0 , the diffusion has had more time ($t = x'/U$) to thicken the thermal boundary layer, which eventually reaches a height $z = \hat{\delta}$ at which the growth rate of (convectively unstable) perturbations is no longer negligible relative to the diffusive growth rate $\kappa/\hat{\delta}^2$ (Howard, 1964). At this point vertical convection sets in, in earnest, penetrating the overlying fluid (region III). As the process continues, we assume that a mixed layer, wherein temperature is effectively constant with height, develops between the unstable surface layer ($z \sim \hat{\delta}$) and stable fluid above ($z = h(x')$). Such layers are observed, for example, in penetrative convection in laboratory tanks (Heidt, 1977), the essential difference being that we have assumed a similar process in a system with horizontal variations. Again, our worries about the possible horizontal circulation set up by the horizontal temperature gradient will be deferred. At some point, then, we enter region IV, within which $h(x')$ is so much larger than the local thermal boundary layer thickness (x') that we can adopt the "1/3 power law" for the Nusselt number, namely

$$Nu = cRa^{1/3} \quad (2)$$

The Nusselt number is defined as the ratio of the total vertical heat flux H in the freely-convecting region to the flux that would occur by conduction alone acting on the vertical mean temperature gradient. If T_m is defined to be the mixed layer temperature then

$$Nu = \left[k (T_i - T_m) \right]^{-1} H h(x') \quad (3)$$

The Rayleigh number Ra is given here by

$$Ra = \frac{g\alpha(T_i - T_m)h^3}{\kappa \nu} \quad (4)$$

while c is an empirically-determined constant (that may, however, vary with the Prandtl number $\sigma = \nu/\kappa$). The "1/3 power law" is the only combination that makes the heat flux H independent of the height $h(x')$ as $h \rightarrow \infty$ (Stern, 1975), as is easily seen by combining (2), (3) and (4) and solving for H . Once more we defer until later questions involving the production of shear by the convection itself in such a way as to alter the heat flux in a way that depends on h and σ . We now consider the convective region IV in more detail.

IV. The Penetrative Convection Region

We now focus our thoughts on region IV (Fig. 3). For convenience sake we have here reversed the directions of the horizontal coordinates, so x' now increases to the right and x_0 moves to the left with speed U . In order to obtain a tractable mathematical representation of the system, we adopt the idealized geometry and temperature profile shown in Fig. 3. In the lowest layer ($0 < z < \delta$) the vertical heat transport is accomplished chiefly by molecular conduction and a correspondingly large fraction of the total mean temperature difference across the system is therefore confined to this stratum. At the top of this layer there is convective activity in the form of intermittent "thermals"-plumes of heated boundary layer fluid which, when sufficiently unstable, rip away from the plate, as shown schematically in Fig. 4. Laboratory experiments in air (Townsend, 1959) and water (Heidt, 1977) demonstrate clearly the existence of the thermals. Figure 4 is based on

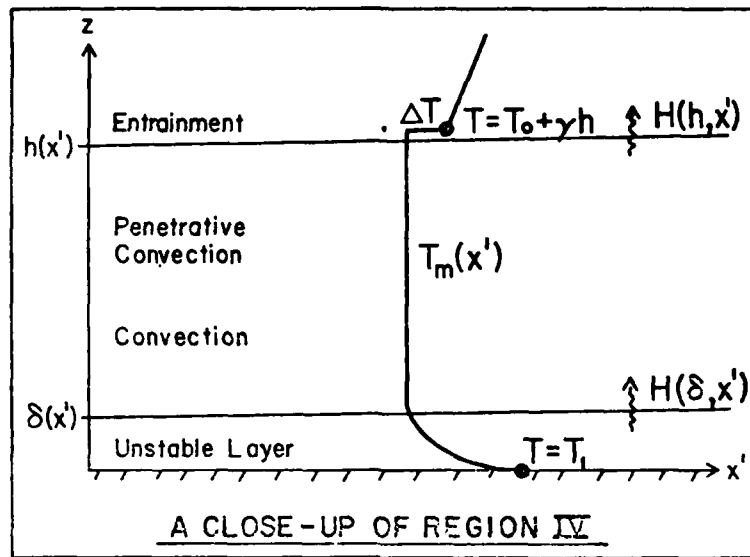


Fig. 3. Idealized geometry and temperature profile in region IV.

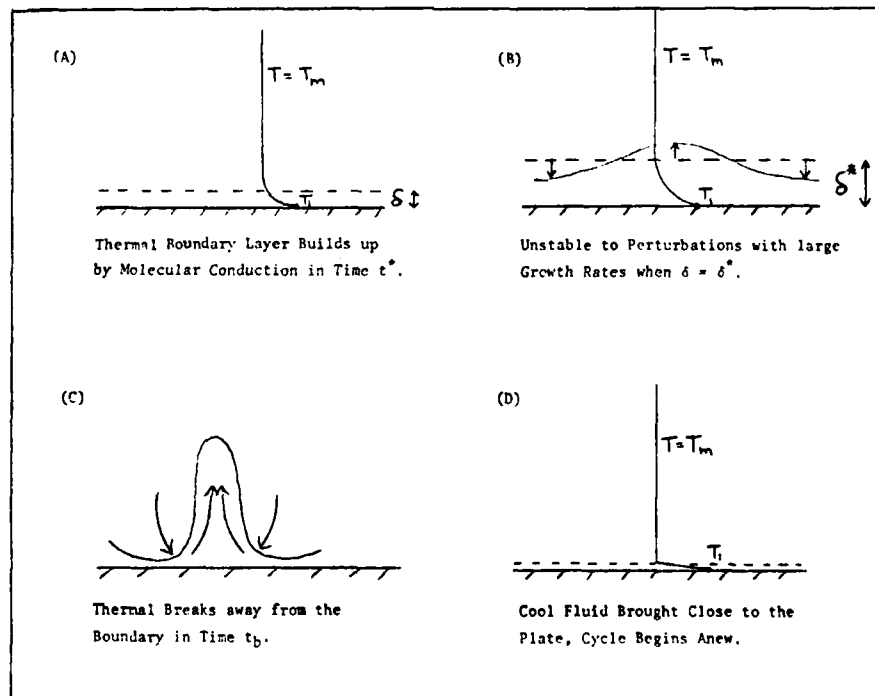


Fig. 4. Schematic stages in the periodic buildup of the thermal boundary layer.

Howard's (1964) theory, where the idea of repetitive buildup of the conduction layer, followed by thermal formation was used to obtain equation (2) for the Nusselt number, with $c = R_{\delta^*}^{-1/3}$ (so long as $t^* \gg t_b$). Here R_{δ^*} is the Rayleigh number based on an assumed "critical" boundary layer depth, i.e.

$$R_{\delta^*} \equiv \frac{g \alpha (T_i - T_m) \delta^{*3}}{\kappa \nu} \quad (5)$$

Howard's preliminary calculations for convectively unstable growth rates greater than δ^{*2}/κ give $R_{\delta^*} \sim 10^3$ while laboratory data suggest $c = 0.089$ (Turner, 1973), implying $R_{\delta^*} = 1419$. The validity of (2) depends on the maintenance of a constant far-field temperature above the plate. In our problem, however, T_m varies locally with time or, equivalently, with x' for a steady state in a reference frame moving with x_0 . If τ_m be the characteristic time for a small (say 1%) change in T_m , then we require $t^* \ll \tau_m$ as a condition for the validity of (2). We shall derive the ratio of these time scales presently. The upward heat flux out of the conductive boundary layer will be called $H(\delta, x')$.

In the fully convective layer we assume that the temperature T_m is independent of height on $\delta < z < h$. This assumption seems justified in view of the laboratory results of Heidt (1977) in water, and also appears to be in reasonable agreement with data from the convective atmospheric boundary layer, even with shear present (Lenschow, 1974; Willis and Deardorff, 1974). Furthermore, for sufficiently large γ , a theory based on the dynamics of thermals in the penetrative region predicts only slight vertical variation of tempera-

ture, followed by a step-like temperature change near $z = h$ (Roisin, 1979). We idealize our profile to a discontinuous jump ΔT at $z = h$ (Fig. 3), above which level the basic state $T = T_0 + \gamma z$ obtains. The entrainment process involves deepening ($\dot{h} > 0$) of the mixed layer as the thermals bombard the stable fluid above, mixing it downward. This mixing implies a non-zero heat flux $H(h, x')$ at the top of the convective layer. In the following section we investigate mathematically the implications of our qualitative picture (Fig. 3) and the heat flux equation (2) for IBL development.

V. Equations for the Internal Boundary Layer

Let θ be the departure of the temperature T from a standard vertical profile $\tilde{T}(z)$ with $\frac{\partial \tilde{T}}{\partial z} = \beta$ (a constant). Then the Boussinesq "heat" equation can be written

$$\frac{\partial \theta}{\partial t} + u \frac{\partial \theta}{\partial x} + w \frac{\partial \theta}{\partial z} + \beta w = \kappa \nabla^2 \theta \quad (6)$$

We time average (6) by applying the operator

$$\overline{(\quad)} \equiv \frac{1}{\tau} \int_{t-\tau/2}^{t+\tau/2} (\quad) dt'$$

where $\tau \ll \tau_m$ is the condition necessary for the thermal turbulence to produce statistically meaningful average quantities. Using the continuity equation

($\partial u / \partial x + \partial w / \partial z = 0$) and assuming $\overline{\partial \theta / \partial t} = \partial \bar{\theta} / \partial t$ we have

$$\frac{\partial \bar{\theta}}{\partial t} + \frac{\partial}{\partial x} \left(\overline{u\theta} - \kappa \frac{\partial \bar{\theta}}{\partial x} \right) + \frac{\partial}{\partial z} \left(\overline{w\theta} - \kappa \frac{\partial \bar{\theta}}{\partial z} \right) + \bar{w} \beta = 0. \quad (7)$$

Anticipating the dominance of vertical over horizontal fluxes, we assume that the second term in (7) is negligible, although it could be parameterized, for example, by

$$\frac{\partial}{\partial x} \left(\overline{u\theta} - \kappa \frac{\partial \bar{\theta}}{\partial x} \right) = \frac{\partial}{\partial x} \left(K^* \frac{\partial \bar{\theta}}{\partial x} \right) \quad (8)$$

where the horizontal eddy viscosity K^* depends on a statistical moment of the vertical velocity, say $(\overline{w^2})^{1/2}$, which value is, in turn, available from other equations. However, we shall see that our solution gives very small $\partial \bar{\theta} / \partial x$, while inclusion of (8) increases the order of the differential equation we must solve. This simply complicates the mathematics without adding materially to the physics. Neglecting this term, then, we integrate (7) vertically on $\delta < z < h$, noting that $\beta = 0$ here and $\partial \bar{\theta} / \partial t = \partial T_m / \partial t$ is independent of z , thus

$$\frac{\partial T_m}{\partial t} (h - \delta) = \left(\overline{w\theta} - \kappa \frac{\partial \bar{\theta}}{\partial z} \right) \Bigg|_{z=h}^{z=\delta} \quad (9)$$

In the systems considered here $\delta \ll h$ so $(h - \delta)$ can be replaced by h . Furthermore, the righthand members of (9) are just the total (conductive plus convective) temperature fluxes at $z = \delta$ and $z = h$, respectively. Therefore we can write the heat fluxes

$$\bar{H}(\delta) = e_0 c_p \left(\overline{w\theta} - \kappa \frac{\partial \bar{\theta}}{\partial z} \right) \Bigg|_{z=\delta} \quad (10)$$

and

$$\bar{H}(h) = \rho_c c_p (\bar{w\theta} - \kappa\gamma) \Big|_{z=h} \quad (11)$$

so that

$$h \frac{\partial T_m}{\partial t} = \frac{\bar{H}(s) - \bar{H}(h)}{\rho_c c_p} \quad (12)$$

We now assume that the asymptotic regime $h, Ra \rightarrow +\infty$ is realized so $\bar{H}(s)$, using (2), (3), and (4), becomes

$$\bar{H}(s) = \frac{\kappa (T_i - T_m)}{h} c Ra^{1/3} = \kappa c \left(\frac{g \alpha}{\kappa \nu} \right)^{1/3} (T_i - T_m)^{4/3} \quad (13)$$

We assume that no mean motions develop in region IV, so that $\bar{u} = \bar{w} = 0$.

Nonetheless, the mixed layer will thicken as the convection proceeds, giving us an eddy temperature flux at h due to the temperature step ΔT . The downward-moving fluid parcels have $T = T_m + \Delta T$ while their upward-moving counterparts have $T = T_m$ giving

$$\bar{w\theta} \Big|_{z=h} = -\dot{h} \Delta T$$

for the temperature flux. In the systems considered here, $\kappa\gamma$ is negligible relative to $\bar{w\theta}$, so we have (Carson and Smith, 1974)

$$\bar{H}(h) = \rho_c c_p \bar{w\theta} \Big|_{z=h} = -\rho_c c_p \dot{h} \Delta T \quad (14)$$

With no mean motion, $\partial(\)/\partial t = d(\)/dt = (\dot{\ })$, so we can combine (12), (13) and (14) into a single ordinary differential equation

$$h \dot{T}_m = \frac{Kc}{\rho c_p} \left(\frac{g \alpha}{\kappa \nu} \right)^{1/3} (T_i - T_m)^{4/3} + h \Delta T \quad (15)$$

where all dependent variables are understood to be time-averaged and we omit the overbars. The unknowns here are h , T_m and ΔT . From the geometry adopted earlier (Fig. 3) we see that

$$\Delta T = T_c + \gamma h - T_m \quad (16)$$

The final equation needed for closure is obtained through parameterization of the entrainment process at $z = h$. We adopt the hypothesis of Plate (1971), namely

$$\Delta T = \gamma(1 - \epsilon)h \quad (17)$$

where ϵ is a dimensionless, empirical parameter that must lie on the interval $0.5 \leq \epsilon \leq 1$ (Heidt, 1977). Equation (17) is exactly equivalent to the assumption

$$H(h) = -Ah(\delta)$$

where

$$A = \frac{1 - \epsilon}{2\epsilon - 1}$$

and yields $\Delta T = 0$ for the case of zero entrainment ($\epsilon = 1$). Equations (16) and (17) imply

$$T_m = T_o + \epsilon \gamma h \quad (18)$$

Heidt's laboratory data for penetrative convection in water heated uniformly from below indicate $\epsilon = 0.87 + 0.03$ and are in reasonable agreement with laboratory and atmospheric measurements reported by other investigators. We shall see presently that our results are relatively insensitive to our choice of ϵ , so the closure hypothesis (17) is not considered to be a serious limitation of the model. We use (17) and (18) to eliminate T_m and h from (15), and define the parameter $T^* = T_1 - T_o$, hence

$$\epsilon \gamma h \dot{h} = \frac{\kappa c}{\rho c_p} \left(\frac{g \alpha}{\kappa \nu} \right)^{1/3} (T^* - \epsilon \gamma h) + \gamma (1 - \epsilon) h \dot{h}$$

Rearranging the above yields

$$h \dot{h} = \frac{\kappa c \left(\frac{g \alpha}{\kappa \nu} \right)^{1/3}}{\rho c_p \gamma (2\epsilon - 1)} (T^* - \epsilon \gamma h)^{4/3} \quad (19)$$

Equation (19) holds at any point (sufficiently far) behind the temperature step at x_o , i.e. at any point in region IV. We require an initial height $h(t = 0)$ to fully determine the integral of (19). Assuming a statistically steady state relative to the coordinate x_o , we can make the transformation $\partial t = \partial \hat{t} = \partial x' / U$ and (19) becomes

$$h \frac{dh}{dx} = \frac{\kappa c \left(\frac{g \alpha}{\kappa \nu} \right)^{1/3}}{U \rho c_p \gamma (2\epsilon - 1)} (T^* - \epsilon \gamma h)^{4/3} \quad (20)$$

where we now omit the primes on x . We must specify a condition $h(0)$ in space in order to integrate away from the beginning of region IV. Introducing non-dimensional variables

$$\hat{h} = h/\eta$$

$$\hat{x} = x/L$$

where

$$\eta = T^*/\epsilon\gamma \quad (21)$$

$$L = \frac{e_c c_p (2\epsilon - 1) U T^{*2/3}}{\epsilon^2 \lambda \gamma} \quad (22)$$

and

$$\lambda = ck \left(\frac{g\alpha}{k\gamma} \right)^{1/3} \quad (23)$$

is a heat transfer coefficient, we obtain (dropping caps)

$$h \frac{dh}{dx} = (1-h)^{4/3} \quad (24)$$

Equation (24) can be integrated to obtain the universal, implicit, nondimensional solution

$$x(h) = \frac{3}{2} (1-h)^{2/3} + 3 (1-h)^{-1/3} - C_3 \quad (25)$$

that can be specialized to any case of interest by choosing the parameters T^* , U and γ . C_3 is the integration constant

$$C_3 = \frac{3}{2} (1-h(0))^{2/3} + 3 (1-h(0))^{-1/3}$$

Other nondimensional quantities of interest are the surface layer heat flux

$$\hat{H}(\delta, x) = \frac{H(\delta, x)}{\lambda T^{*4/3}} = (1-h)^{4/3} \quad (26)$$

the temperature

$$\hat{T}(x) = \frac{T_m(x) - T_c}{T^*} = h(x) \quad (27)$$

and the temperature step at $z = h$

$$\hat{\Delta T}(x) = \frac{\Delta T(x)}{T^*} \left(\frac{\epsilon}{1-\epsilon} \right) = h(x). \quad (28)$$

We now proceed to investigate the properties of our solution.

VI. Properties of the Solution

In Figure 5 we plot $\hat{h}(\hat{x})$ from equation (25), with $C_3 = 4.5$. This initial condition corresponds to convection in air, for example, with $T^* = 25K$, $\gamma = 10^{-2} \text{ Km}^{-1}$ and (dimensional) $h(0) = 10^{-1} \text{ m}$. A range of plausible initial values showed that the solution is insensitive to the choice of C_3 for $\hat{x} > .002$. Figure 5 portrays the nondimensional functions $\hat{h}(\hat{x})$, $\hat{T}(\hat{x})$ and $\Delta\hat{T}(\hat{x})$. The heat flux $\hat{H}(\hat{x})$ is shown in Fig. 6 (note the compression by 1/2 of the vertical scale here). The horizontal asymptotes are

$$\lim_{\hat{x} \rightarrow \infty} (\hat{h}, \hat{T}, \Delta\hat{T}) = 1 \quad (29)$$

and

$$\lim_{\hat{x} \rightarrow \infty} \hat{H} = 0 \quad (30)$$

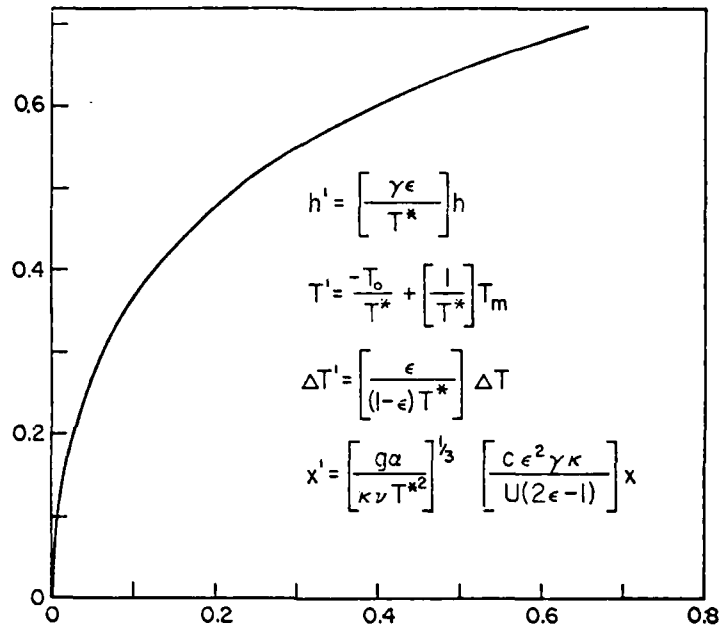


Fig. 5. Nondimensional solution $h(x)$, for the IBL height.

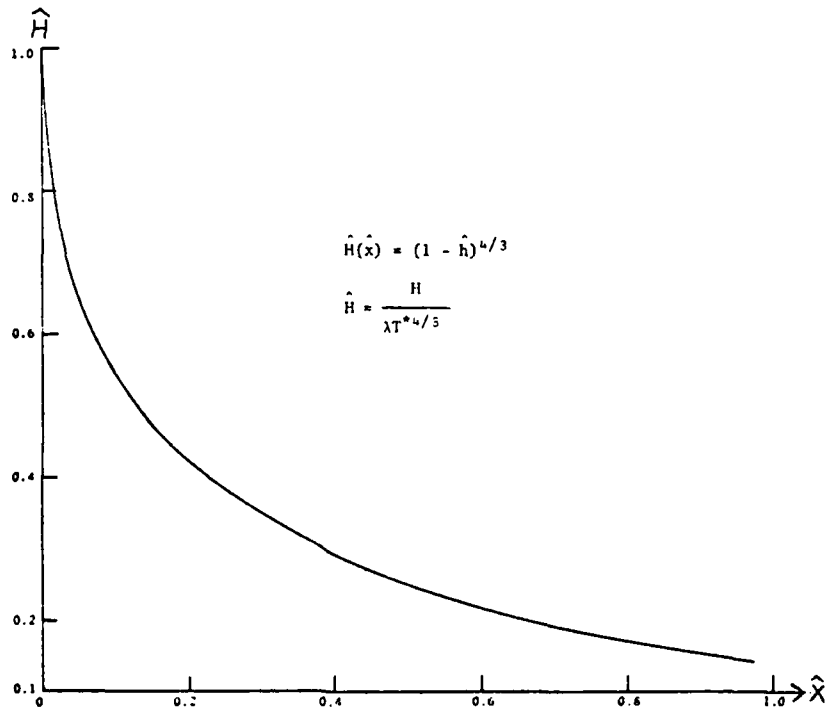


Fig. 6. Nondimensional solution $H(x)$ for the heat flux.

corresponding to $h \rightarrow T^*/\epsilon \gamma$, $T_m \rightarrow T_1$, $\Delta T \rightarrow T^*(1 - \epsilon/\epsilon)$ and $H \rightarrow 0$, all as $x \rightarrow \infty$. Note that $H(0) = \lambda T^{*4/3}$. We can see from the plots that all variables change rapidly with x near $x = 0$, which point corresponds to the temperature step, x_0 . If we define χ_n as the nondimensional distance from x_0 to x (the analog of "fetch" if the fluid were moving at speed U) at which a dependent variable has changed by a factor n of the difference between its initial and asymptotic values, then

$$\left(\chi_{1/4}^{(h)}, \chi_{1/4}^{(T)}, \chi_{1/4}^{(\Delta T)} \right) = 0.040 \quad (31)$$

$$\left(\chi_{1/2}^{(h)}, \chi_{1/2}^{(T)}, \chi_{1/2}^{(\Delta T)} \right) = 0.225 \quad (32)$$

$$\chi_{1/4}^{(H)} = 0.024 \quad (33)$$

and

$$\chi_{1/2}^{(H)} = 0.128 \quad (34)$$

where the superscripts denote the dependent variables. In order to assess the qualitative significance of these numbers, we must multiply by the length scale L . First, however, let us note the qualitative dependence of η , the asymptotic mixed layer height, and L on the parameters of the problem. From (22) we have L proportional to the heat capacity $\rho_o c_p$, and inversely related to the heat transfer coefficient λ . The combination $(2\epsilon - 1)/\epsilon^2$ and the parameter $UT^{*2/3}/\gamma$ (as given in any particular problem) also vary directly as L . The former quotient increases from 0.76 to 1 as ϵ is varied from 0.67

to 1, so our choice of ϵ is not crucial within wide limits as regards the qualitative analyses of L that follow.

As one might expect, the maximum height η is proportional to the temperature difference T^* and inversely proportional to γ . Thus a hotter surface heats a deeper layer, but the stability can confine the mixing. One interesting effect of γ is to keep the heat capacity $\rho_o c_p h$ of the mixed layer smaller, leading to larger temperature changes for a given heat flux. The heat flux scales with $\lambda T^{*4/3}$, independent of γ . For this reason, then, L is inversely proportional to γ , and a larger stability implies a smaller "fetch" required for significant changes in h , T_m , ΔT and H . L also varies directly with U, which might be viewed as the analog to the rate of cold air input to the heated lead. When this rate is large, a longer fetch is required to attenuate the heat flux and vice versa. The dependence of L on $T^{*2/3}$ is a direct consequence of equation (2) for the Nusselt number. A different power of T^* determines the length scale when the transfer of heat by shear turbulence is parameterized in a simple way as we shall see shortly.

Despite the rather questionable correspondence between our model IBL and a real flow over leads, we can adopt the following values characteristic of the lead problem in winter

$$\frac{\rho_o c_p (2\epsilon - 1)}{\epsilon^2 \lambda} = 1.116 \times 10^3 \text{ K}^{1/3} \text{ s m}^{-1} \text{ (air)}$$

$$U = 5 \text{ m s}^{-1}$$

$$T^* = 25 \text{ K}$$

$$\gamma = 10^{-2} \text{ K m}^{-1}$$

and see what happens. The resulting length scale is

$$L = 4769 \text{ Km}$$

so for example, $\chi_{1/4}^{(H)}$ is 114 km. Although wintertime open water features on such a scale have been observed in the Arctic (Muench, 1975) and the Antarctic (Gordon, 1978) pack ice, it is typically assumed that most of the open water and thin ice occurs on smaller scales, i.e. tens to hundreds of meters (Maykut, 1978). If our simple, no-shear model is even in order-of-magnitude agreement with the real atmospheric situation, then it seems justified to compute the large-scale sea-to-air heat flux in polar regions by assuming no variation with fetch over the leads. This assumption is implicit in the computations of Maykut (1978) and Gordon (1979). The fetch required to significantly alter the surface flux by warming the convective layer is simply too long. However, we emphasize that the largest scale openings, by their very nature, account for a large proportion of the surface area of open water. Also the inclusion of the shear processes may cut L down to the size of more typical open water features. Plugging in our typical values for T^* and δ yields the asymptotic convective layer height $\eta = 2.87$ km. Coupled with $\chi_{1/4}^{(h)}$ we have a mixed layer 718 m deep at 190 km downwind. If the model considered here is analogous to the real atmospheric case with shear, we might then expect to see a qualitative feature of the large-scale atmospheric circulation, due to the presence of recurring areas of open water on a 100+ km scale. The "North Water" of Baffin Bay and the Weddell Polynya off Antarctica are examples of recurrent, large-scale open water features. Our calculations would imply a considerable vertical penetration of the heating over such features.

We consider now the scale appropriate to a laboratory experiment, wherein we might test the qualitative picture put forward in Fig. 2.

Using water at $T_o = 293$ K as a working fluid we have

$$\frac{e_o c_p (2\varepsilon - 1)}{\varepsilon^2 \lambda} = 3.191 \times 10^4 \text{ K}^{1/3} \text{ s m}^{-1}$$

$$U = 10^{-2} \text{ m s}^{-1}$$

$$T^* = 30 \text{ K}$$

$$\gamma = 8.0 \times 10^1 \text{ K m}^{-1}$$

These numbers yield

$$L = 34.1 \text{ m}$$

$$\eta = 0.431 \text{ m}$$

so that $X_{1/4}^{(h)} = 1.4 \text{ m}$ and $X_{1/4}^{(H)} = 0.82 \text{ m}$. The estimates above indicate that our experiment might be feasible in a reasonable-size laboratory tank. Recall, though, that regions I, II and III must also occupy some of the tank, and our assumptions about the negligibility of thermally generated mean shear and about the time scales must also be satisfied. We shall return to these problems later.

A final property of interest is the total heat flux, integrated over "fetch" (dx). Some simple substitutions and manipulation of equations (25) and (26) lead to

$$\int_0^{\hat{x}} \hat{H} dx' = \frac{1}{2} \left(\hat{h}^2(\hat{x}) - 1 \right) \Bigg|_{h = \hat{h}(0)}^{h = \hat{h}(\hat{x})}$$

For plausible initial conditions, $\hat{h}(0)$ is vanishingly small compared to one, so

$$\int_0^{\hat{x}} \hat{H} dx' = \frac{\hat{h}^2(\hat{x})}{2} \tag{35}$$

and, in dimensional form

$$\int_0^x H dx' = L \lambda T^* \frac{\hat{h}^2}{2} = \frac{\rho_0 c_p (2\epsilon - 1) U T^*}{\epsilon^2 \gamma} \frac{\hat{h}^2 (x/L)_{(36)}}{2}.$$

In Figure 7 we present a plot of $\hat{h}^2/2$. The horizontal asymptote is

$$\int_0^\infty \hat{H} d\hat{x} = 1/2$$

and the length scales are

$$\chi_{1/4}^{(S)} = 0.225 \quad (37)$$

and

$$\chi_{1/2}^{(S)} = 0.687 \quad (38)$$

These length scales can be compared to their counterparts for h , to illustrate the "flattening" of the curve $h(x)$ achieved by squaring (recall $0 < \hat{h} < 1$). Again the dimensional counterparts of (37) and (38) are quite large for the pack ice parameters used previously. We note that the heat transfer coefficient λ does not appear explicitly in the amplitude coefficient (equation (36)), but its effects are implicit in the argument (x/L) of \hat{h}^2 . Thus as $x \rightarrow \infty$ the integrated heat transfer is the same for all λ , but at any finite x the reduction in L , due to more efficient heat transfer (larger λ) puts us at a larger \hat{x} , that corresponds to a larger \hat{h}^2 and more total heat flux up to that point. Finally, we note that the asymptotic value of the integrated heat flux increases with the velocity U , the square of the temperature difference T^* and with γ^{-1} .

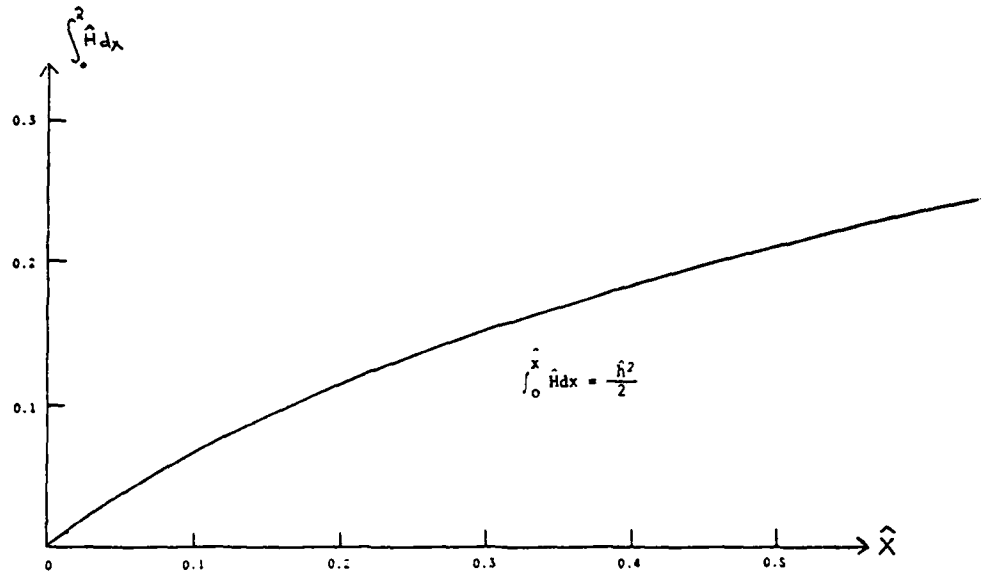


Fig. 7. Nondimensional solution $h^2(x)/2$ for the integrated heat flux.

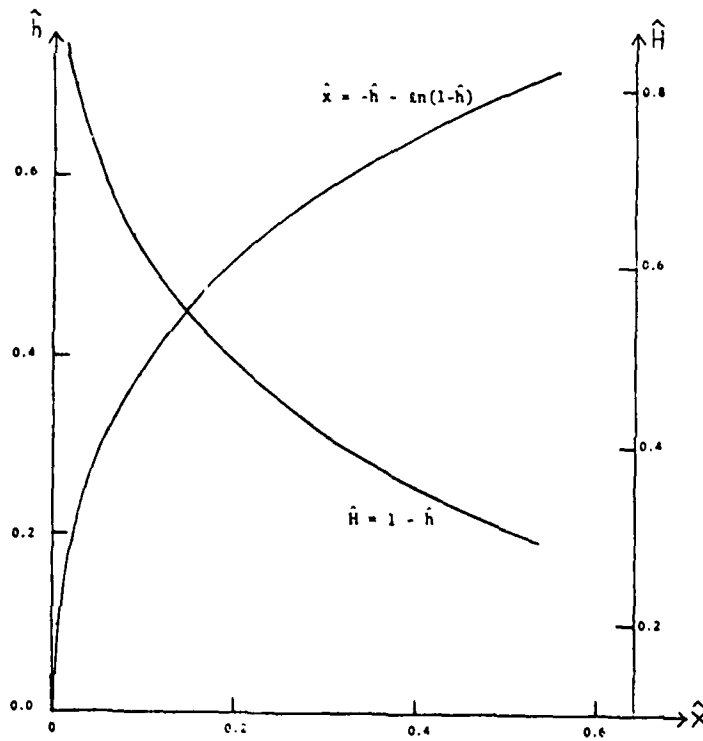


Fig. 8. Nondimensional solutions $h(x)$ and $H(x)$ for the IBL height and heat flux, respectively: turbulent model.

VII. Observations of the Heat Flux from Open Water

Measurements of the type needed for a reasonably complete description of the IBL over open water in the midst of ice are non-existent (to the best of our knowledge). Ideally we would like transects of the IBL height $h(x)$, the surface layer heat flux (measure via eddy correlation techniques) $H(x) = \rho_o c_p \overline{w\theta}$, mean air temperature and wind speed profiles $\overline{\theta}(x,z)$ and $\overline{u}(x,z)$, and the surface layer stress component $\tau(x) = \rho_o \overline{uw}$, in addition to the external parameters U , T_1 and γ . The logistical problems associated with this desideratum are staggering, particularly in view of the long fetches necessary to obtain meaningful differences in the downwind direction. Some IBL properties over small leads (tens of meters) are reported by Andreas, et al. (1979). Briefly, their data include calculations of the average heat flux over 6 to 20 m wide leads, with T^* in the range 23 K to 30 K. The wind speeds \overline{u} at $z = 2$ m vary from 2 to 4.5 $m s^{-1}$ in the cases reported. The heat fluxes are based on a simple conservation of energy argument, utilizing upwind and downwind $\overline{u}(z)$ and $\overline{\theta}(z)$ profiles to compute the sea-air exchange over the lead as a residual, and are therefore independent of assumptions about the nature of the turbulent energy transfer over the lead. The upwind stability is described as "stable" or "unstable" in each case. These data show a significant positive relationship between H and \overline{u} , such that the heat flux increases from 189 $W m^{-2}$ to 370 $W m^{-2}$ as \overline{u} goes from 2.2 $m s^{-1}$ to 3.4 $m s^{-1}$ and T^* decreases from about 30 K to about 25 K. Our model, of course, makes no allowance for the effects of shear embodied in \overline{u} , and H varies as $T^{*4/3}$. For $T^* = 30$ K at $x = 0$ our model gives $H = 103 W m^{-2}$, compared to about 400 $W m^{-2}$ from Andreas, et al. and over 500 $W m^{-2}$

calculated by Maykut (1978). These last values were computed using a turbulent transfer coefficient and the same \bar{u} and T^* as assumed above. Surprisingly our simple, no-shear model gives the same order of magnitude for the flux. On the other hand, we fear that our estimates for L and η may be seriously in error due to our choice for the coefficient λ . We make a brief digression here to pursue some of the gross differences between the "4/3-law" and a turbulent transfer formulation for the flux.

If we assume that the turbulent IBL has adjusted to the temperature step in a shallow surface layer, then we can apply simple empirical formulas for steady, homogeneous shear turbulence. According to Deardorff (1968) the turbulent heat flux can be calculated from

$$H = \rho c_p C_H \bar{u} (T_i - T_m) \quad (39)$$

where the wind speed \bar{u} and transfer coefficient C_H apply at a given height z . Deardorff uses "bulk" (i.e. finite difference) stability parameters to compute the ratio C_H/C_{HN} as a function of C_{HN} and the bulk Richardson number

$$Ri_B = \frac{g \alpha (T_m - T_i) z}{\bar{u}(z)^2} \quad (40)$$

where C_{HN} is the transfer coefficient for neutral stability. When the surface layer is neutral, it is useful to assume that the same eddy mechanisms transport heat and momentum, so that $C_{HN} = C_{DN}$, and C_{DN} is a neutral drag coefficient. Deacon and Webb (1962) present an approximate formula for C_{DN} over ocean surfaces

$$C_{DN} = (a_1 + a_2 \bar{u}) \quad (41)$$

where

$$a_1 = 10^{-3}$$

$$a_2 = 7 \times 10^{-5} \text{ s m}^{-1}$$

If we assume a reference height $z = 10 \text{ m}$ where $\bar{u} = U = 5 \text{ m s}^{-1}$ and $T_m - T_1 = -20\text{K}$, we have $C_{DN} = C_{HN} = 1.35 \times 10^{-3}$ (from (41)) and $Ri_B = -0.27$. Deardorff's calculations then give $C_H/C_{HN} = 1.7$, so we get $C_H = 2.3 \times 10^{-3}$. We define $\lambda_T = e_o c_p C_H$ as a turbulent transfer coefficient. In the case under consideration, $\lambda_T = 2.88 \text{ J m}^{-3} \text{ K}^{-1}$. If we retain all of the assumptions made in our earlier model, except that now we allow the fluid to move at speed U , and carry through the analysis just as before, using $H(\delta) = \lambda_T U (T_1 - T_m)$, we have

$$\hat{h} \frac{d\hat{h}}{d\hat{x}} = 1 - \hat{h} \tag{42}$$

The nondimensionalization is achieved using the same η as before and the new turbulent length scale

$$L_T = \frac{e_o c_p (2\varepsilon - 1) T^*}{\lambda_T \varepsilon^2 \gamma} \tag{43}$$

Equation (42) integrates to

$$\hat{X}(\hat{h}) = -(\hat{h} + \ln\{1 - \hat{h}\}) \tag{44}$$

in nondimensional form. This solution is similar to the one obtained by Fleagle and Businger (1963, p. 206), using a somewhat different approach. The graph of (44) is shown in Fig. 8, along with the nondimensional heat flux

$$\hat{H} = 1 - \hat{h} \tag{45}$$

The length scales in this problem are

$$\chi_{1/4}^{(h)} = 0.038$$

$$\chi_{1/2}^{(h)} = 0.193$$

$$\chi_{1/4}^{(H)} = 0.038$$

$$\chi_{1/2}^{(H)} = 0.193$$

where again we have $\hat{h} = \hat{T} = \Delta\hat{T}$ in nondimensional form. The length scale (43) may be compared with (22) for the no-shear problem. The most obvious difference is the disappearance of U . This is a result of the heat flux equation (39), that varies directly with U . This proportionality just offsets increases in the cold air input rate with increased heat transfer, and is a clear-cut difference between the no-shear case and the shearing case. Also apparent is the linear factor T^* in (43) compared to $T^{*2/3}$ in (22). The linear temperature-dependence requires a longer length L to deepen the convective layer to a given height, other factors being equal. Other factors are not equal, however, which fact brings us to λ_T . The surface heat transfer is much more efficient in the turbulent case, i.e. $\lambda_T U \approx 13 \lambda$. We can see this by plugging in our T^* and γ from the earlier estimate ($L = 4769$ km), to get

$$L_T = 1066 \text{ Km}$$

so that

$$\chi_{1/4}^{(T)} = .038 \rightarrow X_{1/4} = 41 \text{ Km}$$

$$\chi_{1/4}^{(H)} = .038 \rightarrow X_{1/4} = 41 \text{ Km.}$$

The length scales are substantially closer to the typical extent of open water areas. Also the heat flux $\lambda_{TUT^*} = 360 \text{ W m}^{-2}$ is in better agreement with the objective measurements of Andreas, et al., at least for this particular Richardson number. We are still far from the 10 to 100 m scale suggested by Maykut for typical leads, but the simple turbulent model points quite strongly to the importance of air mass modification cutting down the heat flux over the larger open water features. For example, at 200 km downwind from the ice-water edge, our heat flux would be cut by half. Gordon (1978) notes that the Weddell Polynya can have horizontal dimensions of 200 km x 500 km at certain times. In this case, the assumption of heat flux constant with fetch would be incorrect, according to our calculations. We note, however, that we have kept the Richardson number constant, when, in fact, as the air warms Ri is reduced, thus reducing the heat flux from our earlier estimate. This simply reinforces our conclusion, because it implies, for the complete heat flux, a higher power than T^* ¹ and a larger λ_T than λ . However, L_T will be a little larger than we calculated above. It seems that the simple, no-shear model can provide us with some qualitative insight into the nature of the parameters that determine the IBL properties. The flux and length scales are correct to order of magnitude, but incorporation of the shear effects is necessary to bring the scales into more quantitative agreement with measurements. Also, the difference in length scales is such that the inclusion of shear just brings the modification of the heat flux to the status of an "important" parameter, due to the scales of open water found in nature.

VIII. Scale Analysis of Some Processes in the No-shear Model

In this section we just briefly mention some rough measures of the validity of our picture (Fig. 2), given typical parameters. Our primary

assumptions are

- 1) T_m is constant on $\delta < z < h$
- 2) ΔT is a step change in temperature
- 3) $\bar{H}(\delta) \propto (T_1 - T_m)^{4/3}$
- 4) Steady conditions prevail with respect to the coordinate X_0 .

We shall not treat (1) and (2) here, but simply reiterate that they are consistent with observations, and the results are not sensitive to (2). Our third assumption is valid if shear turbulence is not generated and the time scale for individual thermals t^* is much less than τ_m , the scale for a small (say 5%) change in T_m . If this last is satisfied then we can successfully exploit the averaging operator (page 6) by sandwiching its time scale T between t^* and τ_m . We intuitively expect (4) to hold, but a laboratory experiment is needed to verify this.

Let's look at assumption (3). To avoid shear effects we would hope to minimize mean horizontal circulations, because our fluids are viscous and bounded by a solid plate. In the case of uniform heating from below (e.g. $U \rightarrow \infty$) there is no tendency to generate mean horizontal pressure gradients.

However, we have horizontal variations in $\bar{\theta}$ on level surfaces, indicating that pressure gradients will form in regions I through IV. In region IV we already have seen that L is large, and the horizontal pressure gradients induced by the heating will vary as L^{-1} . Furthermore, the thermal turbulence should produce an extremely large "mixing length" for momentum, because thermals near the plate have effectively zero \bar{u} -momentum and rise all the way up to $z = h$. The horizontal circulations in IV might, then, be acceptably small, but this problem requires further work.

In regions I and II we would like molecular diffusion to build up the thermal boundary layer so that it can rapidly convect. Hopefully this would occur before the thermally-generated mean flow develops substantially, although we still might expect eventual thermal plumes even if the boundary layer were disrupted by shear for small x' . For order-of-magnitude purposes, we introduce a boundary layer

depth
$$\delta = \sqrt{\pi \kappa \hat{t}} \quad (46)$$

characteristic of thermal diffusion. If the "critical" Rayleigh number for this layer is about 1500 (Howard, 1964) then δ^* , the critical depth is

$$\delta^* \sim \left(\frac{1500 \kappa \nu}{g \alpha T^*} \right)^{1/3}$$

In the following computations we choose the nominal values for air: $T^* = 25\text{K}$,

$\gamma = 10^{-2} \text{km}^{-1}$, $U = 5 \text{ms}^{-1}$ and for water (in the lab): $T^* = 30 \text{K}$, $\gamma = 80 \text{km}^{-1}$, $U = 10^{-2} \text{ms}^{-1}$.

From these values we have, for air

$$\delta^* \sim 0.8 \text{ cm}$$

$$t^* \sim 1 \text{ sec}$$

$$X^* = U t^* \sim 5 \text{ m}$$

and for water

$$\delta^* \sim 0.2 \text{ cm}$$

$$t^* \sim 5 \text{ sec}$$

$$X^* \sim 5 \text{ cm}$$

Notice that X^* is quite acceptable for a laboratory tank roughly 2 m long.

Qualitatively, Heidt's (1977) $h(t)$ data for uniform heating indicate a length of less than 10 cm for region III, assuming $t = X'/U$, so, in principle, we could see more than 1 m of region IV in a 2 m tank. Now, just ahead of region

I, the fluid is at rest. If we linearize the 2-D Boussinesq vorticity equation about $u = w = 0$, we have

$$\frac{\partial \xi}{\partial t} = g\alpha \frac{\partial \theta}{\partial x'} + \nu \nabla^2 \xi \quad (47)$$

where $\xi = \frac{\partial w}{\partial x'} - \frac{\partial u}{\partial z}$ is the vorticity. If the temperature gradient is assumed known from molecular diffusion and $\frac{\partial \xi}{\partial t}$ is set to zero, we will have just enough vorticity so that viscosity balances the pressure gradient. Because a finite time is required for the fluid to obtain this vorticity, and $\frac{\partial \theta}{\partial x}$ would be smoothed out by the motion, ξ estimated this way should be larger than the value that occurs. If we assume a linear temperature gradient in the vertical T^*/δ where $\delta = \sqrt{\pi \kappa X'/U}$, then we get

$$\frac{\partial \theta}{\partial x'} \sim \frac{T^*}{2X'}$$

We scale the vorticity dissipation as

$$\nu \nabla^2 \xi \sim \nu \frac{\partial \bar{u} / \partial z}{\delta^2} \sim \nu \frac{\bar{u}(\delta)}{\delta^3}$$

Our hypothetical balance requires

$$\bar{u}(\delta) \sim \frac{\delta^3 g \alpha T^*}{2 \nu X'} = \frac{\pi g \alpha T^*}{2 U \sigma} \delta(x')$$

Where σ is the Prandtl number. Region II ends where $\delta = \delta^*$, so our nominal values give us $\bar{u}(\delta^*) = 3 \times 10^{-3} \text{ ms}^{-1}$ for air and $\bar{u}(\delta^*) = 2 \times 10^{-3} \text{ ms}^{-1}$ for water. These numbers are overestimates, and indicate the insignificance of

the circulations in regions I and II, so that we might expect these regions to form approximately the way we assumed earlier. Notice that, by increasing U , we reduce the tendency for horizontal circulations.

Another necessary condition for assumption (3) is that the thermal turbulence itself does not generate sufficient shears to alter the heat flux in a way that depends on h and thus Ra . Kraichnan (1962) used a mixing length argument to show that the turbulent eddies can affect the heat flux, especially for $\sigma < 1$ (i.e. for air).

Qualitatively, we would like a large σ so that the viscous boundary layer is deeper than the molecular conduction layer, allowing thermal plumes to form without the effects of shear $\partial \bar{u} / \partial z$. The Prandtl number for air $\sigma = 0.7$ is "borderline" in this regard, while the value for water $\sigma = 7$ is better.

Finally, and most importantly, we consider the time scales t^* , τ_m and T . If we use the relations

$$Ra^* = 1500 = \frac{g \alpha (T_i - T_m) \delta^{*3}}{\kappa \nu} \quad \text{with} \quad \delta^* = \sqrt{\pi \kappa t^*}$$

and

$$\tau_m(5\%) = \frac{0.05 \rho_0 c_p h (T_i - T_m)}{H(\delta) - H(h)}$$

we find

$$\frac{t^*}{\tau_m} = \frac{991}{\tilde{Ra}^{1/3} \hat{h} (1 - \hat{h})^{1/3}} \quad (48)$$

where

$$\tilde{Ra} = \frac{g\alpha T^*}{\kappa\nu} \left(\frac{T^*}{\epsilon\gamma} \right)^3.$$

Thus t^*/τ_m should be small to guarantee the existence of a Υ for valid averaging.

This ratio decreases as \hat{h} increases, and we use $\hat{h} = 0.1$ along with our nominal γ , T^* and U values to obtain

$$\frac{t^*}{\tau_m} = 2.5 \times 10^{-3}$$

for air, and

$$\frac{t^*}{\tau_m} = 3.15$$

for water. Thus we have about 400 thermals in the time needed for $T_1 - T_m$ to change by 5% in air at $\hat{h} = 0.1$. This seems sufficient. However, the water case looks quite bad, and we might expect the 4/3 law not to apply to penetrative convection wherein T_m is not constant with time. We hope to assess the data of Heidt (1977) in future work to see if his heat fluxes follow a 4/3 power law.

IX. Conclusion

We have constructed simple models of IBL properties and investigated the resulting scales as they depend on T^* , U and γ . For the pure convective case (no-shear) the "fetch" scales are quite long for air.

However, a simple shear-turbulence model indicates that heat fluxes may vary significantly with fetch over the larger open water areas of the polar oceans. The analyses of a possible laboratory simulation of the convective model indicate problems with the $4/3$ law. We hope to pursue this in future work. Also, the linearized vorticity and heat equations can be solved for an imposed surface temperature step at X_0 , eliminating the need for scaling arguments in regions I and II.

Acknowledgements

I would like to thank the entire GFD Staff, and Dr. Melvin Stern in particular, for their constructive advice and encouragement this summer.

REFERENCES

- Andreas, E. L., C. A. Paulson, R. M. Williams, A. W. Lindsay and J. A. Businger, 1979. The turbulent heat flux from Arctic leads. Boundary Layer Meteorology (in press).
- Carson, D. J. and F. B. Smith, 1974. Thermodynamic model for the development of a convectively unstable boundary layer. Advances in Geophysics, 18A, 111-124.
- Deacon, E. L. and E. K. Webb, 1962. Small-scale interactions. The Sea, New York, Interscience, 43-87.
- Deardorff, J. W. 1968. Dependence of air-sea transfer coefficients on bulk ability. Jour. Geophys. Res., 73, 2549-2557.
- Fleagle, R. G. and J. A. Businger, 1963. An Introduction to Atmospheric Physics. New York, Academic Press, 206-207.
- Gordon, A. L., 1978. Deep Antarctic convection west of Maud Rise. Jour. Phys. Oceanogr., 8, 600-612.
- Gordon, A. L., 1979. Meridional heat and salt fluxes in the Southern Ocean. WHOI GFD Lecture.
- Heidt, F. D., 1977. The growth of the mixed layer in a stratified fluid due to penetrative convection. Boundary Layer Meteorology, 12, 439-461.
- Howard, L. N., 1964. Convection at high Rayleigh number. Proc. 11th Inter. Congress of Appl. Mechanics, Berlin, Springer-Verlag, 1109-1115.

- Kraichnan, R. H., 1962. Turbulent thermal convection at arbitrary Prandtl number. Physics of Fluids, 5, 1374-1389.
- Lenschow, D. H., 1974. Model of the height variation of the turbulence kinetic energy budget in the unstable planetary boundary layer. J. Atmos. Sci., 31, 465-474.
- Maykut, G. A., 1978. Energy exchange over young sea ice in the central Arctic. Jour. Geophys. Res., 83, 3646-3658.
- Plate, E. J., 1971. Aerodynamic characteristics of atmospheric boundary layers. U. S. Atomic Energy Commission, Oak Ridge.
- Roisin, B., 1979. Penetrative convection. WHOI GFD Lecture.
- Stern, M. E., 1975. Ocean Circulation Physics. Academic Press, New York, 181-183.
- Townsend, A. A., 1959. Temperature fluctuations over a heated horizontal surface. Jour. Fluid Mech., 5, 209-241.
- Turner, J. S., 1973. Buoyancy effects in fluids. Univ. Press, Cambridge, U.K., 367 pp.
- Willis, G. E. and J. W. Deardorff, 1974. A laboratory model of the unstable planetary boundary layer. Jour. Atmos. Sci., 31, 1297-1307.

A LABORATORY MODEL OF CHIMNEY INSTABILITY

Thomas Keffer

I. The Physical Problem

One might ask why the ocean would choose such a complicated process as chimneying to release its heat to the atmosphere. Why not just simple convection or the deepening of a mixed layer? The answer is that, in general, the ocean does not lose much heat via the relatively rare process of chimneying. But the resulting water products are often dramatically different from surrounding waters and hence attract much attention. Relatively large quantities of dense water can be created in the mid-ocean and moved to the bottom in an organized manner without losing its characteristics to surrounding waters.

II. Observational Background

Chimneying has been observed or suspected to occur in four areas. Of these, the Gulf of Lions in the northwest Mediterranean is by far the most intensively studied. It has been the subject of studies by the MEDOC group in 1979, 1975, and 1970. The consensus from these studies is that chimneying occurs in three distinct phases (at least in the Mediterranean) (Killworth, 1979):

1) Preconditioning:

This stage is characterized by a doming of the isopycnals in a small (1200 km²) area of the ocean (Fig. 1), geostrophically balanced by a surrounding cyclonic circulation. The static stability is much reduced in the center of the dome from values a small distance away. The exact causes of preconditioning are unknown but, in the case of the Gulf of Lions, topographic constraints are suspected (Hogg, 1973).

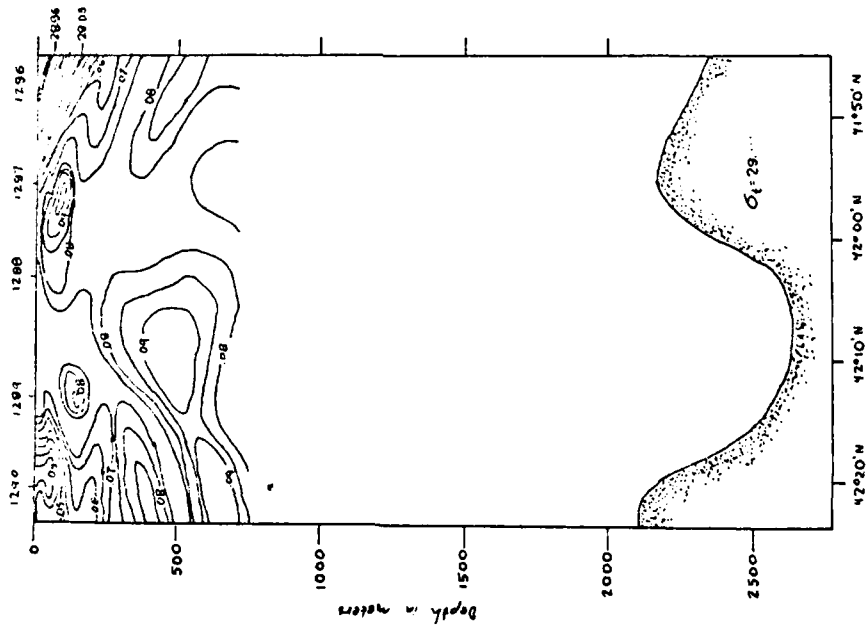


Fig. 1. Section 6 from MEDOC 1969. Taken along the 5015'E meridian immediately before the mistral winds. Note the doming of the isopycnals. From Anati and Stommel (1970).

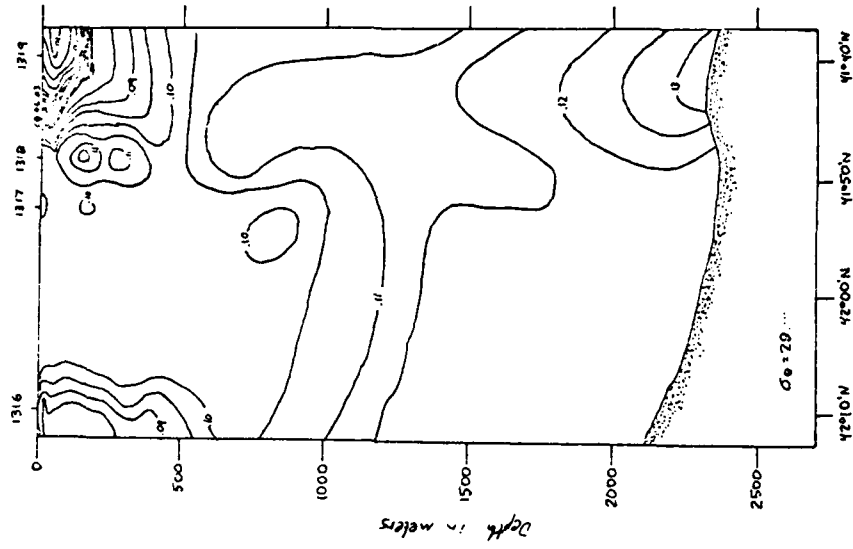


Fig. 2. Section 10 from MEDOC 1969. Taken along the 5015'E meridian shortly after the mistral winds. A homogeneous column (chimney) has formed. From Anati and Stommel (1970).

2) Violent Mixing

The center of the domed region becomes vertically mixed when the cold mistral winds begin to blow (although it is important to note that no mixing occurs from earlier storms that have nearly as strong winds). The result, a mixed, dense cylinder of water extending to 2000 m or more, is the actual "chimney" (Fig. 2).

3) Sinking and Spreading:

The chimney breaks down. Although the process is generally agreed to be a variation on baroclinic instability the exact mechanism is poorly understood. Do the sloping isopycnals surrounding the mixed column break down independently of the column or are the dynamics tightly interlinked? To what extent is mixing involved? Unfortunately the classical Eady model has dominated thinking although the process is probably much more complicated.

The entire process of preconditioning, mixing, and spreading will be referred to as "chimneying" although it is the product of the violent mixing phase (or any other homogeneous water column) that is called a "chimney". The process of "chimney instability" refers to the breakdown of the homogeneous column and subsequent disappearance. Mixing between the surface and subsurface waters occurs at the column periphery and the final chimney product is formed (Gascard, 1978). This paper will address the mechanism of chimney instability, especially the breakdown of the upper layer of a two-layer water column.

III. The Laboratory Model

A cylinder tank 30 cm high by 30 cm diameter was used (Fig. 3). It had an aluminum lid that could be rotated and cooled with ice. Two thermistors were mounted .8 cm below the lid. The inner thermistor was 5 cm from the

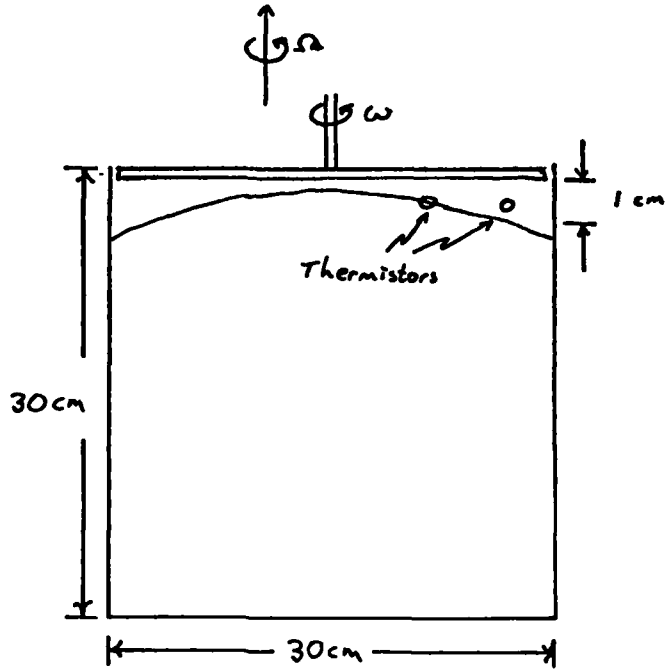


Fig. 3. The laboratory apparatus with the fluid shown in a preconditioned state.

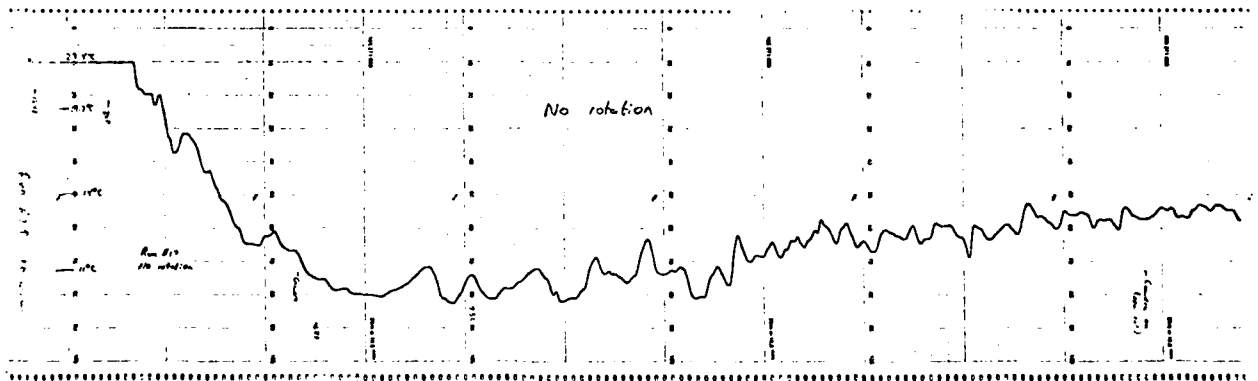


Fig. 4. The record of temperature at the inner thermistor for Case 1 (no rotation). The temperature scale is shown on the lefthand side. It is nonlinear due to the response characteristic of the thermistor. Each horizontal division is 20 seconds.

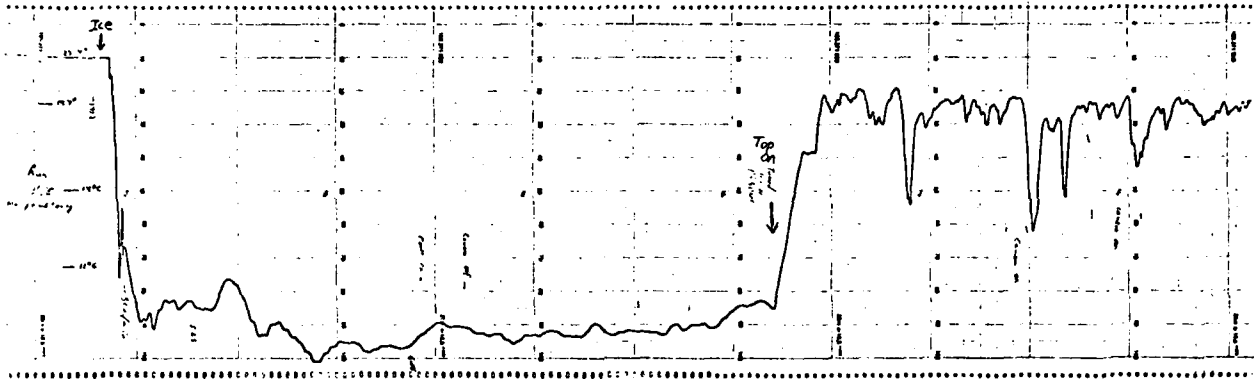


Fig. 5. As in Fig. 4 except for Case 2 (rotation, no preconditioning). The initially stopped lid was turned on approximately 13 minutes after ice was added. Note the instabilities that resulted.

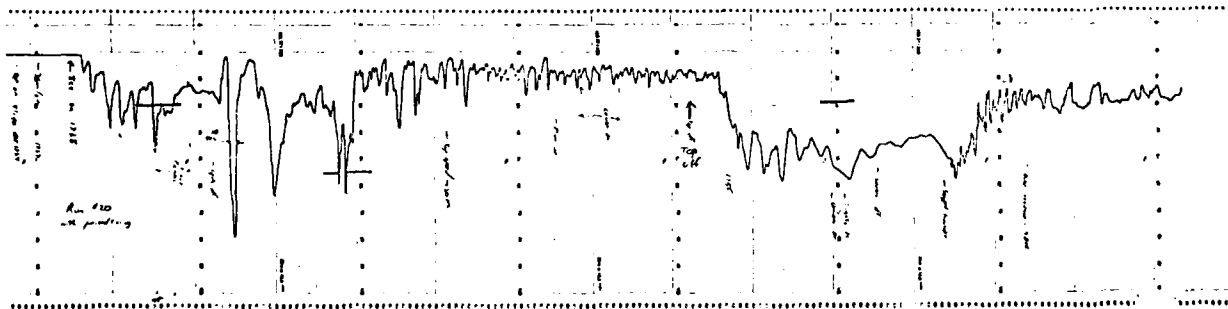


Fig. 6. As in Fig. 4 except for Case 3 (rotation, preconditioning) the horizontal bars mark the temperature as measured at the outer thermistors. The lid speed was increased from 50 to 30 seconds per revolution approximately 9 minutes after ice was added with no resulting instabilities. The lid was stopped approximately 6 minutes later after which the record resembles that of Case 2. The high frequency signal near the end of the record is due to the turntable being stopped.



Fig. 7. A typical picture for Case 2 (rotation, no preconditioning) using a dyed upper layer (taken approximately 10 minutes after ice was added). Note the columns below the interface with length scale of approximately the Rossby radius of deformation (2 cm).



Fig. 8. A typical picture for Case 3 (rotation, preconditioning) using fluorescein dye in the upper layer, taken 3 minutes after ice was added. Long, growing columns extend into the interior of the lower layer. Within 10 minutes the entire lower layer was filled with dye.

center and connected to a chart recorder. The outer thermistor was 13 cm from the center and connected to an ohmmeter. Their thermal time constant was about 2 seconds. The whole apparatus was mounted on a rotating turntable.

Two layers were used with a density contrast of $.005 \text{ g/cm}^3$ using salt. This contrast is far greater than what could be overcome with the effects of cooling alone. The upper layer was 1 cm thick and was either heavily dyed or included some fluorescein dye for visualization. Because of the inevitable difficulties in creating a sharp interface the dyed area usually extended to about 1.5 cm below the lid by the time spin-up was completed.

Before each run the top was carefully levelled and the apparatus was slowly spun-up from rest. This process usually took over an hour, care being taken not to allow the interface to break through to the lid due to Ekman pumping. No experiments were run until at least 20 minutes after the last speed adjustment.

The rotating lid allowed the fluid to be "preconditioned". If it was rotated cyclonically the resulting Ekman suction domed the interface upwards. Care was taken to ensure that it did not break through to the top. The interface was usually at least .2 cm from the lid after preconditioning. The position of the inner thermistor was such that it was completely within the upper layer if the fluid was not preconditioned and at the interface if it was (Fig. 9).

IV. Results of the Laboratory Model

Three cases were considered:

Case 1: No rotation at all

Neither the apparatus nor the lid was turned. The lid was simply cooled. Very little "bottom water" (defined as the movement of dyed fluid

downward into the interior) was produced. Time scales as seen by the inner thermistor were very long (Fig. 4). What production there was seemed to be due to mixing at the interface where enough salt could be mixed in to allow the fluid to sink. No signs of the formation of double diffusive interfaces could be seen within the short time it was watched (30 minutes).

Case 2: Rotation but no Preconditioning.

There was, again, very little bottom water production. Time scales were long and temperature perturbations, as measured by the inner thermistor, were small (Fig. 5). Small bulges (Fig. 7) with a scale on the order of the Rossby radius (2 cm) could be seen on the interface. The inner thermistor was 4-8°C colder than the outer thermistor, probably due to their relative distance from the cylinder's edge.

Case 3: Rotation and Preconditioning

The fluid was preconditioned before ice was added. The resulting temperature record at the inner thermistor can be seen in Fig. 6. Large temperature fluctuations (10°C) with short time scales (10-15 seconds per spike) can be seen. There was extensive bottom water production (Fig. 8). Close analysis of movies taken immediately after ice was added showed that instabilities of the interface started at about 5 cm from the center of the cylinder and "grew into" the thicker parts of the upper layer. The preconditioned interface was thin, but still sloping, at the preferred starting point.

The observations suggest a structure as in Fig 9. The interface was originally dome shaped and then developed small, wavelike, azimuthal, perturbations that rapidly grew until they produced long columns as in Fig. 8. The thermistor record can be explained as follows: When the interface was high the thermistor was exposed to the warm water of the lower layer. When

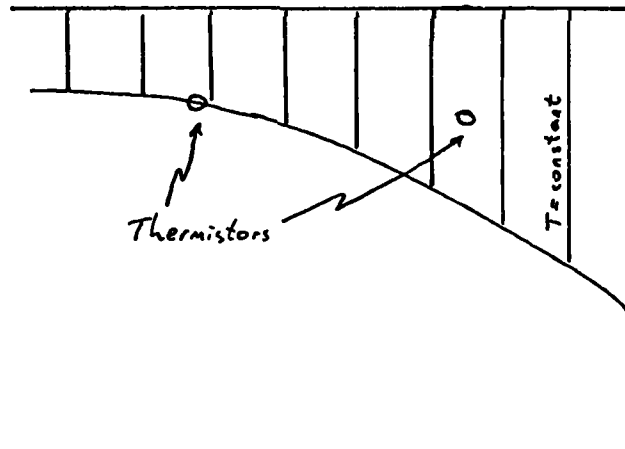
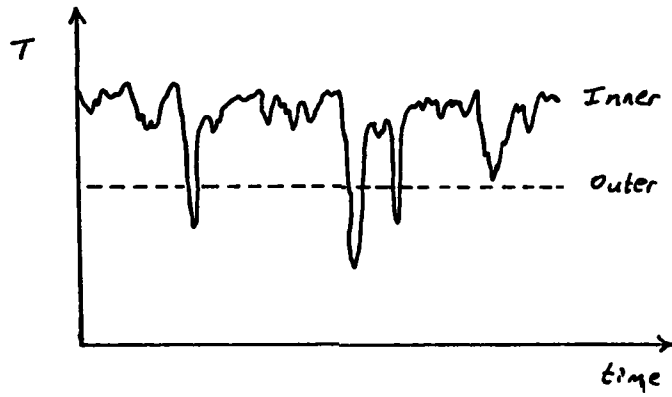


Fig. 9. (a) A schematic of the relative temperatures of the two thermistors. Note that the coldest temperatures measured at the inner thermistor is colder than the outer thermistor. (b) One possible temperature configuration to produce such a record. Large vertical mixing in the upper layer would be assumed.

the interface moved down the thermistor felt the cold water of the upper layer but it was even colder than the water at the outer thermistor. The difference of $3-6^{\circ}\text{C}$ represents a density difference of about $5 \times 10^{-4} \text{ g/cm}^3$ or one-tenth of the density contrast between the two layers. This small density gradient in the upper layer can be extremely destabilizing as will be shown in Section 6.

In the lab experiment the density gradient could be created by any of the three different mechanisms. First, of course, is the relative distance from the edge of the cylinder. The effects of this were seen in Case 2. Second, for a constant heat flux thinner parts of the upper layer will become colder than the thicker parts. Finally, if mixing with the lower layer were to occur it will happen at the thinnest parts of the upper layer first. The mixed in salt would increase the density at the center relative to the edges. In the ocean, the last two mechanisms could operate and suggest looking carefully for correlations in changes of radial density gradients with subsequent chimney breakdown.

It is worth noting that if the fluid is "preconditioned" after ice is added the resulting action resembles Case 3 very closely. This was done with the run showed in Fig. 5. Hence, a cooled fluid can be "postconditioned" and still result in chimney instability. This may be difficult to do in the ocean due to the long time scale usually associated with doming of the interface.

V. Theoretical Model

A theoretical model is developed using a rotating annulus of width L with rigid lid containing a two-layer fluid of density contrast $\Delta\rho$.

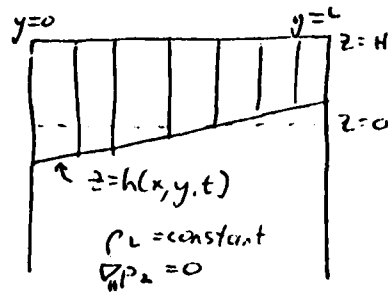


Figure 10

The lower layer is assumed to be infinitely deep and passive ($\nabla_w p_2 = 0$). The upper layer is thin ($H \ll L$) and has horizontal gradients of density only. The assumption here is, of course, that the effects of vertical convective mixing from the cold lid will be dominant, ensuring that horizontal density gradients will be much larger than vertical gradients within the upper layer. The interface is allowed to move as a function of x, y, t . Additional assumptions are:

$$\frac{\partial \rho_1}{\partial y} L \ll \Delta \rho \quad \frac{\Delta h}{H} \ll 1 \quad \frac{\omega}{2\Omega} \equiv \epsilon \ll 1 \quad \frac{A_H}{2\Omega L^2} E \ll 1$$

where Ω is the angular velocity of the tank, ω is the angular velocity of the lid, and ϵ and E are the Rossby and Ekman numbers respectively.

Viscosity was included in the upper layer because without it a fluid with no vertical stratification has the highest growth rates at infinitely small scales.

We integrate the hydrostatic relation and using the requirement that

$$\nabla_w p_2 = 0 \quad \text{we find:}$$

$$\nabla_w p_1 = g \nabla_w [(\rho_2 - \rho_1)(H - h)] + g(H - z) \nabla_w \rho_1 \quad (1)$$

where ∇_H represents horizontal gradients. The governing, dimensional, equations become:

$$u_t + \bar{u} \cdot \nabla_3 u - fv = \frac{g}{\rho_0} \{ (\Delta\rho - \rho) h_x + (z-h) \rho_x \} + A_H \nabla_H^2 u \quad (2)$$

$$v_t + \bar{u} \cdot \nabla_3 v + fu = \frac{g}{\rho_0} \{ (\Delta\rho - \rho) h_y + (z-h) \rho_y \} + A_H \nabla_H^2 v \quad (3)$$

$$u_x + v_y + w_z = 0 \quad (4)$$

$$0 = -p_z - \rho g \quad (5)$$

$$\rho_t + u\rho_x + v\rho_y = A_H \nabla_H^2 \rho \quad (6)$$

where ∇_3 is the three-dimensional del operator and all variables refer to the upper layer. Note that the righthand side of Eq. (2) and (3) contain depth independent ($\sim h_x$) and depth dependent ($\sim z\rho_x$) terms.

We non-dimensionalize as follows:

$$\begin{aligned} u, v &\sim U & x, y &\sim L \\ w &\sim \frac{H}{L} U & z &\sim H \\ h &\sim \frac{\epsilon}{\beta^2} H & t &\sim \frac{L}{U} \end{aligned}$$

where

$$\beta^2 = \frac{g \Delta\rho H}{\rho_0 f^2 L^2}$$

The non-dimensional equations are:

$$\epsilon \{ u_t + \bar{u} \cdot \nabla_3 u \} - v = (1 - \epsilon\rho) h_x + (\beta^2 - z - \epsilon h) \rho_x + \epsilon \nabla_H^2 u \quad \text{x-momentum} \quad (7)$$

$$\varepsilon \{ v_t + \bar{u} \cdot \nabla_3 v \} + u = (1 - \varepsilon \rho) h_y + (B^2 z - \varepsilon h) \rho_y + \varepsilon \nabla_w^2 v \quad \text{y-momentum} \quad (8)$$

$$u_x + v_y + w_z = 0 \quad \text{continuity} \quad (9)$$

$$\rho_t + \bar{u} \cdot \nabla_w \rho = \frac{\varepsilon}{\xi} \nabla^2 \rho \quad \text{density} \quad (10)$$

$$\left. \int_{\frac{\varepsilon h}{B^2}}^1 (u_x + v_y) dz - \frac{\varepsilon}{g^2} \frac{Dh}{Dt} \right|_{z=\frac{\varepsilon h}{B^2}} = 0 \quad \text{Kinematic at interface} \quad (11)$$

with boundary conditions:

$$\begin{aligned} w(z=1) &= 0 & w(z=\frac{\varepsilon h}{B^2}) &= \frac{\varepsilon}{B^2} \frac{Dh}{Dt} \\ v(y=0) &= 0 & v(y=1) &= 0 \end{aligned}$$

A perturbation expansion on the variables u, v, h, ρ, w can be performed with the small parameter ε .

$$\begin{pmatrix} u \\ v \\ h \\ \rho \\ w \end{pmatrix} = \begin{pmatrix} u \\ v \\ h \\ \rho \\ w \end{pmatrix}^{(0)} + \varepsilon \begin{pmatrix} u \\ v \\ h \\ \rho \\ w \end{pmatrix}^{(1)} + \dots \quad (12)$$

to find a pair of quasi-geostrophic eqs. in the dependent variables $\rho^{(0)}, h^{(0)}$:

$$\begin{aligned} \nabla_w^2 (h^{(0)} + \frac{1}{2} B^2 \rho^{(0)})_t + \{ J(\nabla_w^2 h^{(0)}, h^{(0)} + \frac{1}{2} B^2 \rho^{(0)}) + J(\frac{1}{2} B^2 \nabla_w^2 \rho^{(0)}, h^{(0)} + \frac{\varepsilon}{3} B^2 \rho^{(0)}) \} \\ - \frac{\varepsilon}{\xi} \nabla_w^4 (h^{(0)} + \frac{1}{2} B^2 \rho^{(0)}) = \frac{1}{B^2} h_t^{(0)} \quad \text{vorticity} \quad (13) \end{aligned}$$

$$\rho_t^{(0)} + J(\rho^{(0)}, h^{(0)}) = \frac{E}{\xi} \nabla_w^2 \rho^{(0)} \quad \text{density} \quad (14)$$

where:

$$v_x^{(0)} - u_y^{(0)} = -\nabla_w^2 (h^{(0)} + B^2 z \rho^{(0)}) = \text{vorticity}$$

$$J(r, s) = \frac{\partial r}{\partial x} \frac{\partial s}{\partial y} - \frac{\partial r}{\partial y} \frac{\partial s}{\partial x} \quad \text{is the Jacobian operator} \quad (15)$$

We now consider a basic state given by:

$$\bar{\rho} = \bar{\rho}_y (y - \frac{1}{2}) \quad (16)$$

$$\bar{h} = \bar{h}_y (y - \frac{1}{2}) \quad (17)$$

where the interface has a constant slope given by \bar{h}_y and the upper layer has a constant density gradient given by $\bar{\rho}_y$ both in the y direction. We then consider its stability to small wavelike perturbations:

$$\rho = \bar{\rho}_y (y - \frac{1}{2}) + \rho'(x, y, t) \quad (18)$$

$$h = \bar{h}_y (y - \frac{1}{2}) + h'(x, y, t) \quad (19)$$

where

$$\begin{pmatrix} p' \\ h' \end{pmatrix} = \begin{pmatrix} D \\ F \end{pmatrix} e^{ik(x-ct)} \sin n\pi y \quad (20)$$

and D, F are complex relative amplitudes. A dispersion relation can be obtained from the resulting, linearized equations:

$$\begin{aligned} c^2 \left(\kappa^2 + \frac{1}{B^2} + c \left[-2(2\bar{h}_y + B^2\bar{\rho}_y) - \frac{i}{k} \frac{E}{\epsilon} (2\kappa^2 - \frac{1}{B^2}) - \frac{1}{B^2} \bar{h}_y \right] \right. \\ \left. + 2 \left[\bar{h}_y^2 + B^2 \bar{h}_y \bar{\rho}_y + \frac{1}{3} B^4 \bar{\rho}_y^2 - \left(\frac{E}{\epsilon} \frac{\kappa^2}{k} \right)^2 - \frac{i}{k} \frac{E}{\epsilon} \kappa^2 (2\bar{h}_y + B^2\bar{\rho}_y) \right] \right) = 0 \end{aligned} \quad (21)$$

where $\kappa^2 \equiv k^2 + (n\pi)^2$. With the aid of a computer this relationship can be examined for unstable ($\text{Im} \kappa > 0$) roots as a function of the parameters $B^2, \bar{h}_y, \bar{\rho}_y, E/\epsilon, k, \kappa$.

VI. Results of the Theoretical Model

Table I gives the best estimate of the values of the various parameters for the lab experiment. A comment on a few of them would be in order. The Rossby number was estimated from the differential rotation rate of the lid.

TABLE I
PARAMETERS FROM THE LAB EXPERIMENT

<u>PARAMETER</u>	<u>DEFINITION</u>	<u>NOMINAL VALUE</u>
L		10 cm
H		1 cm
ϵ	$\frac{H}{2\Omega}$	0.1
B ²	$\frac{g \Delta \rho H}{\rho_0 f^2 L^2}$	0.3 ²
$\Delta \rho$		0.005 g/cm ³
\overline{h}_y	$\frac{H}{L} \frac{B^2}{\epsilon} \frac{\partial h^*}{\partial y^*}$	0.02
$\overline{\rho}_y$	$\frac{L}{\epsilon \Delta \rho} \frac{\partial \rho^*}{\partial y^*}$	1.0
t		1.26 sec ⁻¹
E	$\frac{A_H}{f L^2}$	0.8 x 10 ⁻⁴

TABLE I. Best estimates of the parameters from the lab experiment. Stars (*) refer to dimensional quantity.

The non-dimensional basic density gradient, $\overline{\rho}_y$, was estimated from the temperature difference between the two thermistors. This difference was approximately 5°C. The thermal expansion coefficient was taken as $1 \times 10^{-4}/^\circ\text{C}$, giving a horizontal density difference of $5 \times 10^{-4} \text{g/cm}^3$. An estimate of the Ekman number was difficult to obtain. It was evaluated using the molecular value of A_H ($.01 \text{ cm}^2/\text{sec}$) and good results were obtained. However, this

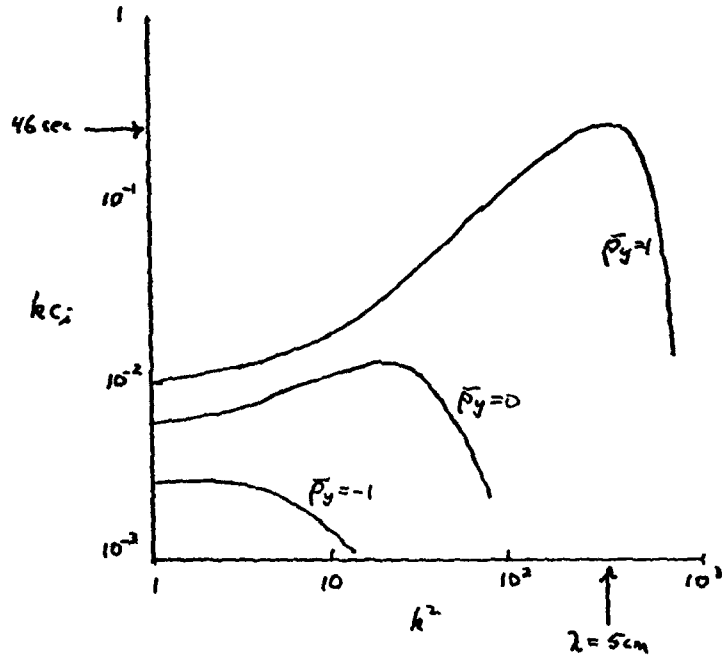


Fig. 11. Growth rate ($k(i)$) versus k^2 for three different layer 1 density gradients.

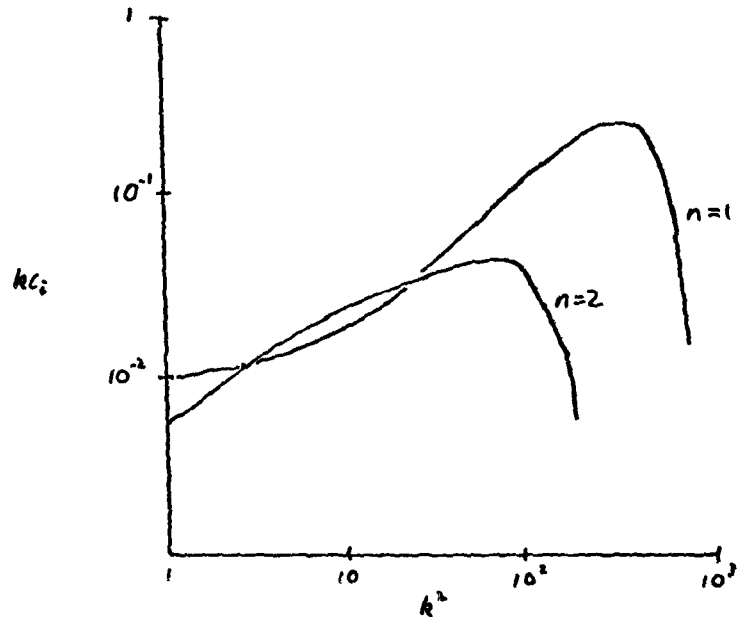


Fig. 12. Growth rate versus k^2 for two different cross-channel mode numbers.

seems difficult to justify in light of the undoubtedly turbulent nature of the upper layer. Higher values of E tended to select larger length scales and slower growth rates than what was observed. Finally, the dimensional slope was taken to be 1/10 which means $\Delta h \approx H$ and the assumption $\Delta h \ll H$ is violated. The theory is, therefore, at its limit of validity.

Figure 11 shows three curves of growth rate (kc_1) versus k^2 for three different values of horizontal density gradients in the upper layer. The upper curve ($\bar{\rho}_y = 1$) is the best estimate for the experiment and predicts an e-folding time of 46 seconds, a half-period of 9 seconds and a half-wavelength of 2.5 cm. All agree well with observations. The central and lower curves give growth rates for no horizontal gradient and a reversed gradient (heaviest on the outside) respectively. It can be seen that the addition of a very modest horizontal density gradient with the same sign as \bar{h}_y can be extremely destabilizing. Conversely, a gradient in the opposite direction can greatly slow or even prevent the growth of a perturbation of an otherwise unstable \bar{h}_y . Furthermore, a destabilizing horizontal gradient encourages smaller scale instabilities.

Figure 12 shows the growth curve for cross-channel mode number 2 as well as for 1. Growth rate is slower and larger along-channel scales are favored.

VII. Conclusions

Preconditioning is a vital part of chimneying. It greatly enhances bottom water production by two mechanisms. First, it offers a potential energy source for chimney instability to work on. Secondly, it allows differential cooling and mixing in the upper layer with subsequent destabilization due to

the resulting horizontal gradients. What is not known is the role of the homogeneous column as an energy source. A follow up study should address the dynamics of this central column.

Instabilities seem to start on the slopes of the thinnest parts of the upper layer and "grow into" the thicker parts. This may be due to the largest horizontal density gradients being created here by nearby mixing. As the instabilities grow they may mix in dense fluid, moving the density gradient outwards, and the instabilities follow.

Finally, the fastest growing wavelengths are not necessarily of the order of the Rossby radius of deformation. The theoretical analysis indicates that the horizontal scale may be set by friction and the magnitude of the layer 1 horizontal density gradients.

VIII Acknowledgments

Special thanks are due to Peter Killworth and John Whitehead for their guidance and assistance. Many thanks is also owed to Robert Frazel for his helpful technical assistance.

REFERENCES

- Anati, D. and H. Stommel, 1970. The initial phase of deep-water formation in the Northwest Mediterranean, during MEDOC, 1969. Cabiers Oceanographiques, 22, 347-351.
- Gascard, J. C., 1978. Mediterranean deep water formation, baroclinic instability and oceanic eddies. Oceanologica Acta, 1(3), 315-330.
- Hogg, N. G., 1973. The preconditioning phase of MEDOC 1969. II. Topographic effects. Deep-Sea Res., 20, 449-459.
- Killworth, P. D., 1979. On chimney formations in the ocean. J. Phys. Oceanogr., 9, 531-554.

A MODEL FOR THE SEASONAL VARIATION OF
THE MIXED LAYER IN THE ARCTIC OCEAN

PETER LEMKE

1. Introduction

Models for the oceanic mixed layer are of special importance in climate related problems, since the mixed layer represents the link between the atmosphere and the interior ocean.

There are a variety of models that describe the time evolution of the mixed layer properties in the open oceans, where wind mixing and seasonal varying heating and cooling are the dominant forcing mechanisms that form the mixed layer. For a review see Niiler and Kraus (1977).

Despite the heavy ice cover a well developed mixed layer is also observed in the Arctic Ocean. The dominant forcing mechanisms here are ice melting and freezing and mechanical mixing due to keel stirring induced by the ice motion. Observations show (McPhee, 1978; Hunkins, Bauer and Amos, 1977) that during most of the year the base of the mixed layer is sharply defined, the depth of which varies from 40-50 m in late May to 15-25 m in the summer. The salinity varies from 30.5 o/oo to 29.8 o/oo respectively.

In this paper a rough quantitative description of the observed data is achieved from a one-dimensional mixed layer model.

II. One-Dimensional Mixed Layer Model

One-dimensional models of the upper ocean are useful since vertical variations of temperature and salinity are more pronounced than horizontal changes. For many purposes the upper ocean layers can therefore be treated as homogeneous along the horizontal, so that the horizontal derivatives can be omitted in the governing equations. This is especially true for the Arctic Ocean (see Fig. 2, SCOR Report). Since temperature, salinity, density and

velocity fields interact with each other, a complete model has to describe the evolution of each of these properties. The prognostic equations can be derived from a set of one-dimensional conservation equations. In particular, the salt flux balance leads to an equation for the bulk salinity \bar{S}

$$\frac{\partial \bar{S}}{\partial t} + \frac{\partial \overline{w'S'}}{\partial z} = 0 \quad (1)$$

where $S' = S - \bar{S}$ and $W' = W - \bar{W}$ are the deviations from their mean values. Similar equations can be derived for temperature, buoyancy and horizontal velocity \bar{v} (Niiler and Kraus, 1977).

To solve this set of equations one has to find explicit expressions for the turbulent fluxes. This has been done in several ways, i.e., in turbulence closure models, by eddy coefficient and mixing length hypothesis and in mixed layer models.

In the latter models it is assumed that mean temperature, salinity and horizontal velocity are uniform in the vertical within the mixed layer. This assumption permits vertical integration of (1) and the equivalent equations for temperature, buoyancy and horizontal momentum from the bottom to the top of the mixed layer. Now these mixed layer properties are described as functions of exchanges with the air above and the deep ocean below.

Since with the time-dependent mixed layer depth $H(t)$ a new variable is introduced, the system has to be closed by an equation for the entrainment velocity w_e defined by

$$w_e \equiv \frac{dH}{dt} \quad \text{for} \quad \frac{dH}{dt} > 0$$

$$w_e = 0 \quad \text{for} \quad \frac{dH}{dt} < 0$$

Entrainment is associated with layer deepening. There is no entrainment during the retreat of the mixed layer. The closure of the system is achieved by introduction of the turbulence energy equation. This is given in simplified form by (Niiler and Kraus, 1977).

$$w_e (c_i^2 - \zeta \bar{y}^2) = 2m u_*^3 + nHB + I \quad (2)$$

with $c_i^2 = H \Delta b$, where Δb is the buoyancy step at the lower interface of the mixed layer, c_i is the velocity of the long interval waves at the lower interface, u_* is the friction velocity, B is the buoyancy flux at the surface and I is the rate of potential energy change produced by penetrating solar radiation, ζ , m and n are parameters. The meanings of the terms are:

- A: Work per unit time needed to lift the dense entrained water and to mix it through the layer;
- C: rate at which energy of the mean velocity field is reduced by mixing across the layer base;
- D: rate of working by the wind;
- E: rate of potential energy change produced by fluxes across the sea surface.

In order to complete Eq. (2) a dissipative term has to be added. But it is assumed that this term is composed of terms which are individually proportional to the active turbulence generating process, described by C, D and also by E during the cooling period when B is positive.

Therefore the parameters ζ , m and n in Eq. (2) include a parameterization of the dissipation ($n = 1$ during the heating period when $B < 0$). With the turbulence energy equation (2) the set of differential equations for the mixed layer is closed.

For given fluxes at the surface and at the lower interface the evolution of the mixed layer properties can be described. Usually mixed layer

models are applied to open ocean, where wind mixing and time varying buoyancy flux at the surface, due to heating and cooling, determine the seasonal variation of the mixed layer. Since the seasonal variation is more pronounced in heating and cooling than in evaporation and precipitation the main variables in these models are temperature and depth. The important features of the evolution of the mixed layer described in such one-dimensional models are:

- a) a pronounced retreat of the mixed layer during the period of increased heating,
- b) a slow deepening of the mixed layer during the period of decreased heating,
- c) a faster deepening during the cooling period, due to wind mixing and mixing through thermal convection.

III. Application to the Arctic Ocean

The one-dimensional mixed layer model described by Niiler and Kraus (1977) is now applied to an ice covered ocean. In this case the seasonal variation of the air temperature (heating, cooling) has nearly no effect on the temperature of the mixed layer. Observations indicate that the mixed layer temperature exhibits nearly no seasonal variation and is near the freezing point down to a depth of 60 m all over the year (Hunkins, Bauer and Amos, 1977). All net heat fluxes are used to freeze and melt ice. During ice melting fresh water is added on top of the mixed layer that tends to stabilize the stratification. During the freezing period brine is excluded from the newly formed ice, a layer of dense salty water destabilizes the stratification and brine convection starts to develop.

Therefore, the seasonal variation of surface air temperature manifests itself in a seasonal varying buoyancy flux due to positive fresh water flux in

summer and negative fresh water flux (out of the mixed layer) during winter-time. Consequently, in contrast to the open ocean, the main variables in a polar mixed layer model must be salinity and depth. For simplicity it is assumed in this paper that the mean horizontal velocity in the mixed layer is zero ($\bar{v} = 0$).

There are two principal stirring mechanisms that may form a mixed layer: brine convection and mechanical mixing due to keel stirring by ice drift. Usually it is considered that brine convection is the most important mixing mechanism. One purpose of this paper is to show the relative importance of the mechanical mixing which has not conclusively been shown in previous studies (Solomon, 1973).

The two main features of our polar mixed layer model are therefore the kinetic energy input due to mechanical stirring by the ice motion and the seasonally varying buoyancy flux at the sea surface.

a) Mechanical Mixing

Since the ice is rather rough at the bottom, ice motion may be an effective mixing mechanism. The ice keels have an average depth of 5-10 m, but may extend through the whole mixed layer (40-50 m).

It was one of the major oceanographic goals during AIDJEX to express the drag exerted on the ice as a function of the speed of the ice relative to the undisturbed ocean. It was found that the drag was fairly constant over a wide speed range and could be expressed as $|\bar{\tau}| = \rho c_w |\bar{u}|^2$, where $|\bar{u}|$ is the speed of the ice relative to the ocean below the frictional layer and the drag coefficient, c_w , was about 0.0034 (McPhee, 1975; MCPhee and Smith, 1976). For $\bar{v} = 0$ in the mixed layer, \bar{u} is the ice velocity, and the rate of working κ is

$$\kappa = \bar{u} \cdot \bar{\tau} = \rho c_w \bar{u}^3 \cos \alpha \quad (3)$$

where α is the frictional turning angle, found to be about 24° .

b) Surface Buoyancy Flux

There are two sources for the surface buoyancy flux, melting and freezing of sea ice and river run off and ice export out of the Arctic Basin. From observations it is evident that the average melting and freezing rate is about 40-50 cm/season. Roughly the same amount of fresh water is added by river run off during summer. Since the salinity of the Arctic Ocean does not change on a long term, ice export and outflow of low saline water out of the Arctic Basin have to balance the river run off. Because of lack of data and for simplicity it is therefore assumed that 1 m of fresh water with a salinity of 5 o/oo ($S_{ice} \approx 5$ o/oo) is added to the top of the mixed layer during summer and removed during winter. Since melting and freezing start slowly and exhibit a maximum roughly in the middle of the seasons, a sinusoidal time dependence of the fresh water flux F is assumed (Fig. 1).

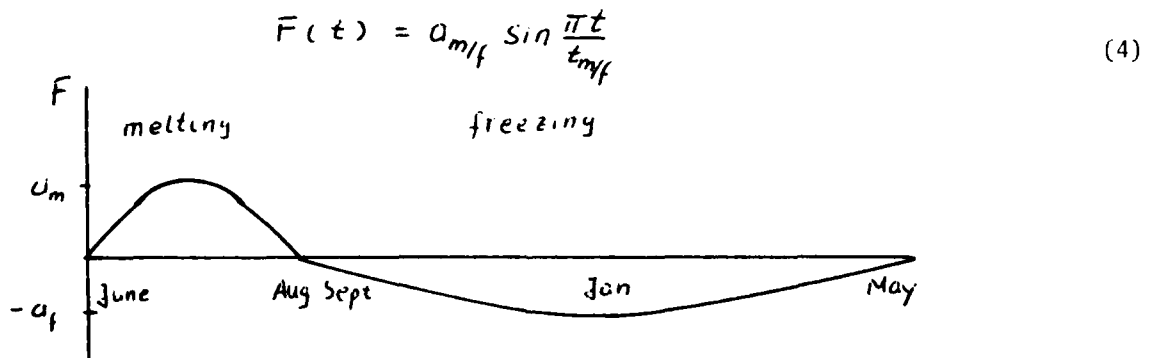


Fig. 1. Seasonal Variation of the Surface Fresh Water Flux

The amplitudes a_m and a_f in (4) can be determined by integrating F over the melting season ($t_m = 3$ months) and freezing season respectively ($t_f = 9$ months) and setting the result equal to the total fresh water flux

per season (1 m). The buoyancy flux B associated with this fresh water flux F is given by

$$B = -g \beta F(S-5) \quad (5)$$

where g is the gravitational acceleration and $\beta = \frac{1}{\rho} \frac{\partial \rho}{\partial S}$ describes the dependence of the water density ρ as a function of the salinity S of the mixed layer. For $T = 0^\circ\text{C}$ and $p = p_0$, $\beta \approx 0.8 \cdot 10^{-3} \left[\frac{1}{\text{o/oo}} \right]$ (Sverdrup, Johnson, Fleming, 1942).

c) Parameterization of the Dissipation

Not all of the kinetic energy supplied by the keel stirring is used to entrain water from below; some part of it is dissipated on its way to the mixed layer base. Besides the (poorly known) dependence on surface properties it seems to be appropriate to model the dissipation of kinetic energy due to mechanical mixing as a function of depth. It also seems reasonable to assume a cut-off depth H_0 at which all of the kinetic energy input is dissipated. With the assumption of a linear dependence on depth, the factor m in (2) is given by

$$m = m_1 - \frac{m_1 H}{H_0} \quad (6)$$

with $m_1 = c_w \cos \alpha$ (from Eq. 3).

During the freezing period, a certain amount of the convective energy (described by 1-n in Eq. (2)) is dissipated. From laboratory tank experiments Deardorff, Willis, and Lilly (1969) found that $n = 0.015$. Farmer (1975)

derived a mean of $n = 0.036$ from observations of a mixed layer under the ice of a frozen lake. Gill and Turner (1976) obtained the best agreement with observations of the mixed layer in the North Atlantic when convective stirring is non-penetrative ($n = 0$).

From the model described in the following sections, it is found that the assumption of a cut-off depth H_0 in (6) is necessary to obtain a finite and complete cyclical response of the mixed layer to forcing with cyclical B (Eq. (5)). The assumption of a cut-off depth is also necessary for n , since convection and keel stirring would otherwise continuously deepen the mixed layer from one cycle to the other. Therefore, during the freezing period, n is taken to be

$$n = 1 - \frac{H}{H_0} \quad (7)$$

otherwise $n = 1$.

d) Model Equations

Eq. (2) and the vertical integral of Eq. (1) rewritten as

$$w_e = \frac{2m u^3}{H \Delta b} - \frac{nB}{\Delta b} \quad (8)$$

$$\frac{dS}{dt} = \frac{w_e (\hat{S} - S)}{H} - \frac{FS}{H} \quad (9)$$

represent the two governing differential equations for the polar mixed layer. The buoyancy step Δb at the lower interface is proportional to the salinity step ΔS , $\Delta b = -g \beta \Delta S$, and no solar radiation penetrates through the ice, $I = 0$ in Eq. (2). In Eqs. (8) and (9) S stands for $S - S_{ice} = S - 5$.

As usual, it is assumed that the mechanical stirring is insufficient to produce entrainment ($w_e = 0$) during the period of increased melting (increased stability). In this case Eqs. (8) and (9) simplify to

$$H = \frac{A}{FS + \frac{A}{H_0}} \quad (10)$$

$$\frac{dS}{dt} = -\frac{F^2 S^2}{A} - \frac{FS}{H_0} \quad (11)$$

where $A = \frac{2 m_1 u^3}{g \beta}$.

Eq. (11) is a Bernoulli differential equation which, with the substitution $f = S^{-1}$, can be converted into a linear differential equation. The solution for S is then given by

$$S^{-1}(t) = e^{-a_1 \cos \pi t / t_m} \left[\frac{a_1^2}{A} \int_0^t e^{a_1 \cos \pi t' / t_m} \sin^2 \frac{\pi t'}{t_m} dt' + \frac{1}{S_0} \right] \quad (12)$$

where S_0 is the salinity at the end of the freezing period and $a_1 = -\frac{a_m t_m}{H_0 \pi}$ is half the ratio between the annual thickness of the fresh water layer and the maximum mixed layer depth. Since this ratio is very small, $a_1 \approx \frac{1}{200}$, the exponential in Eq. (12) can be approximated by 1. The integral is then easily evaluated and the final expression for the salinity S is:

$$S(t) = \frac{S_0}{1 + S_0 \frac{a_m^2}{2A} t - \frac{t_m}{2\pi} \sin \frac{2\pi t}{t_m}} \quad (13)$$

The mixed layer depth H is given by substituting (13) into (10).

The minimum mixed layer depth occurs in the middle of the melting season ($t_{m/2}$) when the fresh water flux F is a maximum.

In the second part of the melting season (decreasing stability) the mixed layer deepens again (entrainment), and the salinity and depth are given by integrating Eqs. (8) and (9), which can be rewritten as

$$\frac{dH}{dt} = \frac{A}{\beta - S} \left(\frac{1}{H} - \frac{1}{H_0} \right) - \frac{nFS}{\beta - S} \quad (14)$$

$$\frac{dS}{dt} = \frac{A}{H} \left(\frac{1}{H} - \frac{1}{H_0} \right) - (1 + n) \frac{FS}{H} \quad (15)$$

IV. Results

Depth and salinity of the mixed layer during the first part of the melting season (from Eqs. (13) and (10)) for different ice drift velocities are shown in Fig. 2. It is obvious that the mixed layer exhibits a fast retreat in the beginning, whereas the salinity slowly starts to change. For a larger kinetic energy input (larger u) the changes in both the mixed layer depth and the salinity are smaller.

Figure 3, showing salinity and depth for different seasonal fresh water fluxes F , clearly indicates that higher buoyancy flux (increased stability) results in larger changes for both depth and salinity.

Since the values for u and F in Figures 2 and 3 are quite reasonable and the retreated mixed layer depth and salinity roughly coincide with observations, it can be concluded that the keel stirring represents an effective mixing mechanism. If it were not effective, the mixed layer depth would rather quickly drop to zero.

From the time evolution of the mixed layer depth $H(t)$ and the salinity $S(t)$, shown in Figure 2, the structure of the halocline $S(H)$ after the retreat of the mixed layer can be derived. This is shown in Figure 4 for different ice velocities u . The shape of the salinity profile is in good agreement with observations (McPhee, 1979).

In order to infer the evolution of S and H during the rest of the annual cycle Eqs. (14) and (15) were integrated on a TI-59 pocket calculator

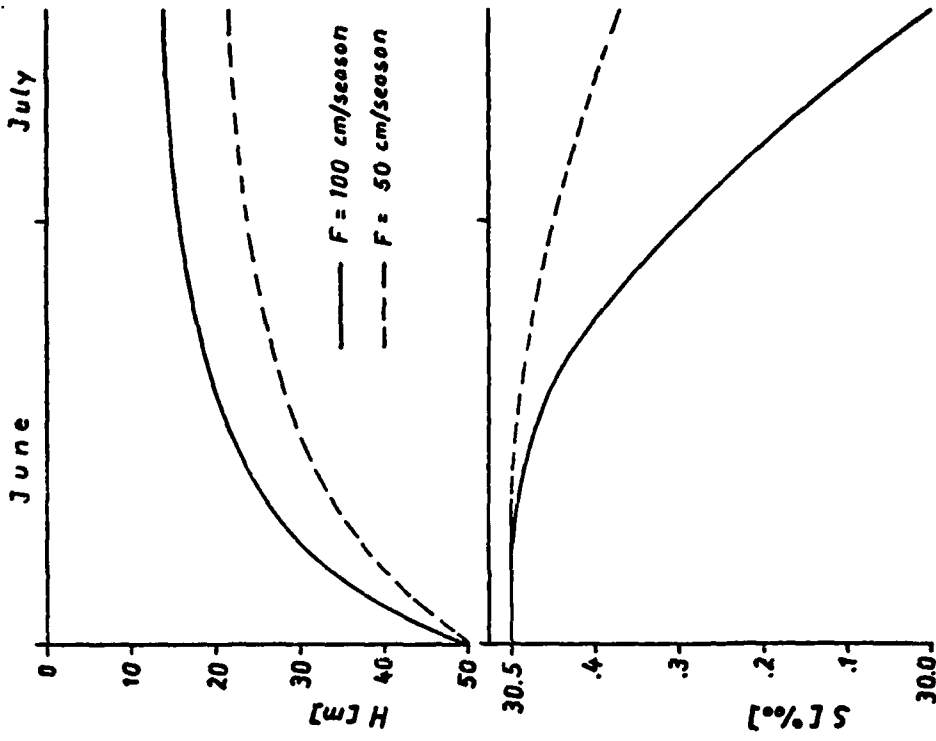


Fig. 3. Depth and salinity of the retreating mixed layer during increased melting for different fresh water fluxes ($u = 5$ cm/s).

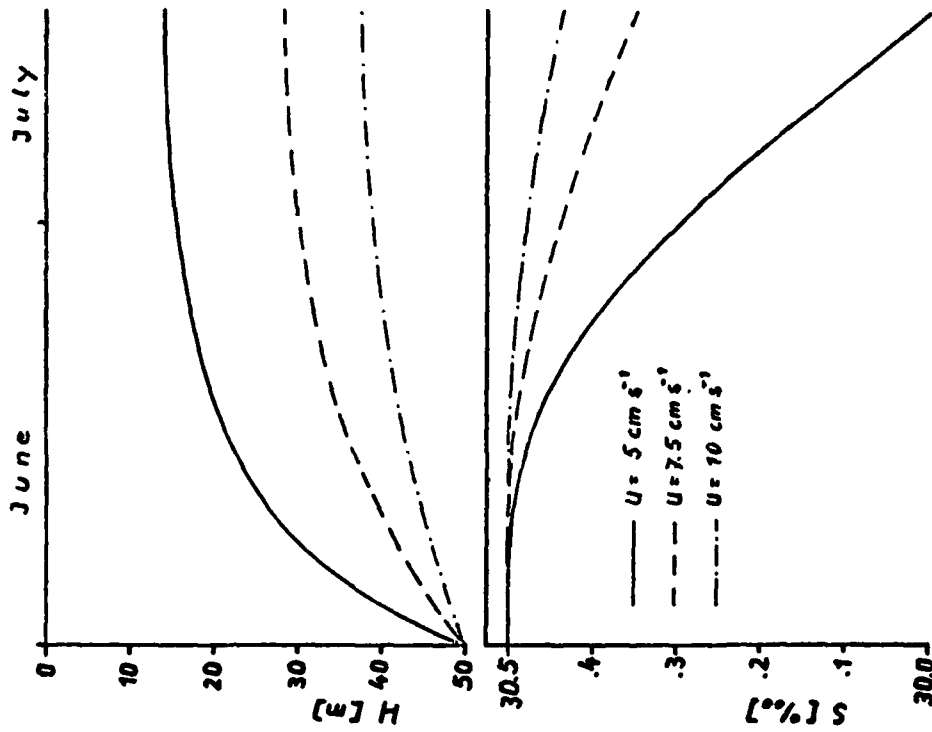


Fig. 2. Depth and salinity of the retreating mixed layer during increased melting for different ice drift velocities u ($F = 100$ cm/season).

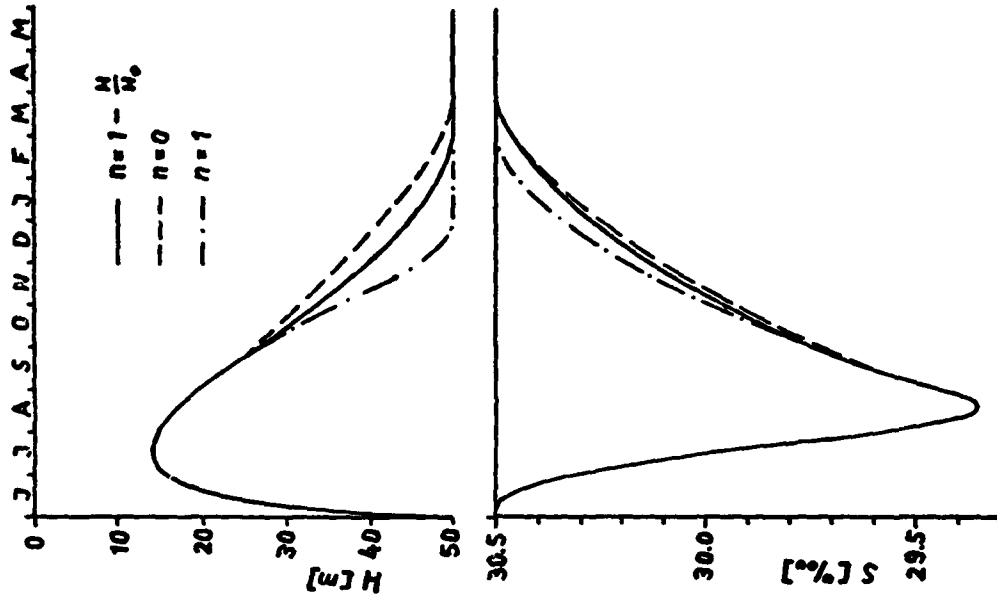


Fig. 5. Seasonal variation of the mixed layer depth H and salinity S for non-penetrative (dashed line), partly penetrative (solid line) and fully penetrative convection (dashed-dotted line). (Ice drift $u = 5$ cm/s, freshwater flux $F = 100$ cm/season).

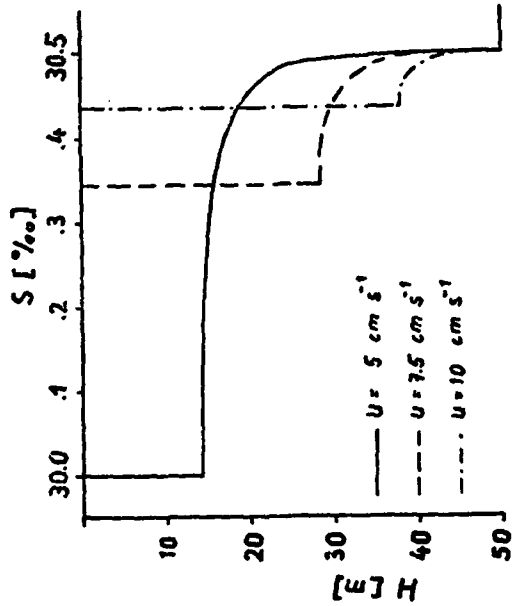


Fig. 4. Structure of the halocline after retreat of the mixed layer in the middle of the melting season for different ice drift velocities u .

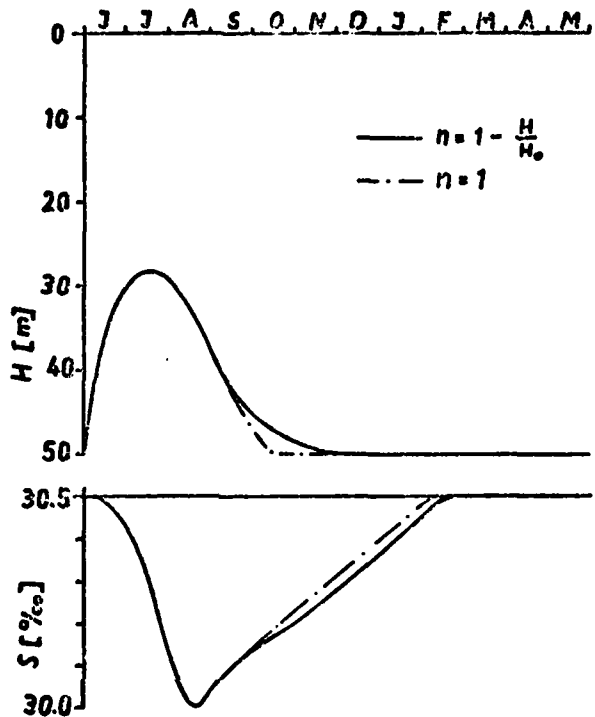


Fig. 6. Seasonal variation of the mixed layer depth H and salinity S for fully (dashed-dotted line) and partly penetrative convection (solid line). (Ice drift $u = 7.5$ cm/s; fresh water flux $F = 100$ cm/season.)

with a second order Runge-Kutta method. S is taken from Figure 4, i.e., the mixed layer entrains water, that it has left behind during the retreat. It is assumed that the salinity profile below the mixed layer remains undisturbed.

The results are shown in Figures 5 ($u = 5 \text{ cms}^{-1}$) and 6 ($u = 7.5 \text{ cms}^{-1}$) for fully penetrative convection (dashed-dotted line), partly penetrative convection (solid-line) and non-penetrative convection (dashed line). In the fully penetrative case an infinite salinity step at the bottom of the mixed layer is assumed. The seasonal variations of H and S are roughly in the range of observations, but the mixed layer depth seems to reach its maximum value too early in the freezing season, especially for larger ice velocities u (Fig. 6). Here the partly penetrative and non-penetrative convection are nearly identical. The reason for the fast deepening is probably the parameterization of the dissipation. Since there is obviously too much energy available for entrainment, the vertical integrated dissipation (Eq. (6) and (7)) should exhibit an exponential increase with depth rather than a linear increase.

Unfortunately, there are at this time, no annual time series of S , H , F and u available, in order to determine the dissipation by fitting this one-dimensional mixed layer model to the observed data. Therefore, the questions whether the brine convection is penetrative or non-penetrative cannot be answered at this stage.

V. Conclusions

The observations of the seasonal variation of the mixed layer in the Arctic Ocean can roughly be described by a one-dimensional model for the mixed layer depth and the salinity.

It is conclusively shown that the keel stirring represents an effective mixing mechanism for forming a mixed layer. The model should be extended by

including an equation for the mean horizontal velocity and for the temperature although the latter one does not seem to be very important. The parameterization of the dissipation has to be improved, perhaps by fitting models to observed data.

Acknowledgements

I would like to thank the GFD Staff, especially K. Hunkins, P. Killworth and A. Gill, for very stimulating discussions.

REFERENCES

- Deardorff, J. W., G. E. Willis and D. K. Lilly, 1969. Laboratory investigation of a nonsteady penetrative convection. J Fluid Mech., 35, 7-31.
- Farmer, D. M., 1975. Penetrative convection in the absence of mean shear. Quart. J. R. Met. Soc., 101, 869-891.
- Gill, A. E. and J. S. Turner, 1975. A comparison of seasonal thermocline models with observations. Deep-Sea Res., 23, 391-401.
- Hunkins, K., E. Bauer and A. Amos, 1977. Salinity and temperature measurements from AIDJEX manned array. Proc. of the Symposium on Sea Ice Processes and Models, Sept., 1977, Seattle.
- McPhee, M. G., 1975. The effect of ice motion on the mixed layer under Arctic pack ice. AIDJEX Bull., 30, 1-27.
- McPhee, M. G., 1978. AIDJEX Oceanographic Data Report, AIDJEX Bull., 39, 33-77.
- McPhee, M. G., 1979. Unpublished AIDJEX data, private communication.
- McPhee, M. G. and J. D. Smith, 1976. Measurements of the turbulent boundary layer under pack ice. Jour. Phys. Oceanogr., 6, 696-711.
- Niller, P. P. and E. B. Kraus, 1977. One-dimensional models of the upper ocean. In E. B. Kraus (ed.) Modelling and Prediction of the Upper Layers of the Ocean. Pergamon Press, 143-172.
- SCOR Working Group 58, 1979. The Arctic Ocean Heat Budget. Univ. of Bergen, Norway.
- Sverdrup, H. U., M. W. Johnson and R. Fleming, 1942. The Oceans, Prentice-Hall, N. J.

STEADY TWO-LAYER SOURCE-SINK FLOW

Lynne Talley

I. Introduction

Ocean circulation can be thought of as being forced almost entirely by heating and cooling, whether directly, as a result of heat transfer across the ocean surface, or indirectly by the winds which arise from heating and cooling of the atmosphere. In this paper we will be mainly interested in extremely idealized circulation produced directly by cooling and heating. Many simplifications are made with respect to the flow, the basin geometry and the type of forcing but it is hoped that insight will be gained into the circulation in regions where cooling and heating are particularly important. We specifically have in mind the circulation of the northern North Atlantic, the Norwegian-Greenland Sea and to a lesser extent, the Labrador Sea. The Norwegian--Greenland Sea is particularly well known as the source of the cold saline Bottom Water which enters the North Atlantic in deep western boundary currents and which contributes its characteristics to the North Atlantic Deep Water. Bottom Water is formed in the large cyclonic gyre occupying the Greenland Sea from inflowing Atlantic Water (Carmack and Aagaard, 1973) which enters the Norwegian Sea as the broad northward Norwegian Current. It subsequently appears to become more topographically controlled as it strengthens on the eastern flank of the Jan Mayen Ridge, flows through the gap in the East Jan Mayen Ridge and then along the eastern side of the Greenland Basin where it forms the eastern side of the cyclonic Greenland Sea gyre (Metcalf, 1960).

To some extent, there is a similar process in the Labrador Sea, although the dense water which is formed there is an Intermediate Water rather than

Bottom Water. There also, a cyclonic gyre is the scene of production of dense water, fueled by the inflow of Atlantic Water in the West Greenland Current and colder fresher water from the north.

The model discussed here is a steady extension of the time dependent two-layer model investigated analytically and numerically by Gill (1979b) and the time dependent axisymmetric model of Gill et. al. (1979). It is a steady two-layer model, intended for instance to model the upper Atlantic Water and deep Bottom Water of the Norwegian-Greenland Sea, in which cooling is introduced as simple mass and momentum transfer from a layer of density ρ_1 , to a layer of density ρ_2 . We will not concern ourselves with the actual mechanism for production of denser water, but rather with the resulting circulation. Steady linear solutions for the baroclinic mode will be sought for various types of distributed transfer in a meridional channel and then for point transfer in a horizontally infinite ocean, on the f and β planes, motivated by the apparent presence of large scale density currents and localized Bottom Water formation in the Norwegian-Greenland Sea. The effects of bottom friction and topography are not included.

Formulation in terms of a two-layer model is largely motivated by the apparent two component nature of the Norwegian-Greenland Sea circulation. We undoubtedly lose some information about the vertical structure of the flow but can, nevertheless, see the broad outlines of the forced solution.

We will see that inclusion of diffusion in a steady two-layer model implies the possibility of eastern boundary layers in both f and β plane steady ocean circulation models.

II. Equations

The two-layer system is illustrated in Fig. 1. h_1 is the variable height of the upper layer, H_2 its rest value and $h = H_1 - h_1 = h_2$ the height of

the interface above its resting value $h = 0$. ρ_1 is the density of the upper layer, p_1 its pressure and p the value of the pressure at the rigid lid. The depth integrated equations of motion and continuity for the two layers are:

$$\begin{aligned} \frac{Du_1}{Dt} - fv_1 &= -\frac{P_x}{\rho_0} - \epsilon_1^*(u_1 - u_2) + \tau^{(x)} \\ \frac{Dv_1}{Dt} + fu_1 &= -\frac{P_y}{\rho_0} - \epsilon_1^*(v_1 - v_2) + \tau^{(y)} \\ p_1 &= P + \rho_1 g(H_1 + H_2 - z) \\ \frac{Dh_1}{Dt} + H_1(u_{1x} + v_{1y}) &= -Q + \epsilon_2^* h \end{aligned} \tag{2.1}$$

$$\begin{aligned} \frac{Du_2}{Dt} - fv_2 &= -\frac{P_x}{\rho_0} - g'h_x - \epsilon_1^*(u_2 - u_1) \\ \frac{Dv_2}{Dt} + fu_2 &= -\frac{P_y}{\rho_0} - g'h_y - \epsilon_1^*(v_2 - v_1) \\ p_2 &= P + \rho_2 g(H_2 + h - z) + \rho_1 g(H_1 - h) \\ \frac{Dh_2}{Dt} + H_2(u_{2x} + v_{2y}) &= Q - \epsilon_2^* h \end{aligned}$$

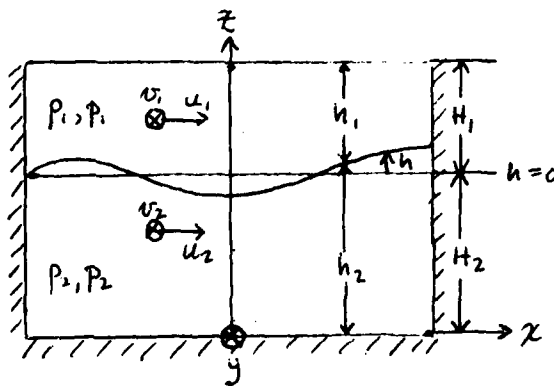


Fig. 1. Two-Layer Geometry.

We make the Boussinesq approximation and have already included hydrostatics in writing the x and y momentum equations where $g' = \frac{\rho_2 - \rho_1}{\rho_0} g$. Q is the mass transfer from the top to bottom layer, ϵ_1^* the coefficient of momentum transfer and ϵ_2^* the coefficient of diffusion. We have also included wind stress although, in the absence of bottom friction, the barotropic component of the flow can never be steady. The term $\epsilon_1^* h$ is absolutely crucial for the existence of steady solutions in the presence of a nonzero mass transfer Q since continual transfer without damping would imply continual spinup. One way of obtaining diffusion terms of this form is by using a normal mode analysis. If the buoyancy frequency N is constant, the variations in the vertical are sinusoidal with a fixed wave number m for each mode. Thus the operator

$$\frac{\partial}{\partial t} - \kappa \frac{\partial^2}{\partial z^2}$$

can be replaced by

$$\frac{\partial}{\partial t} + Km^2$$

for this particular mode, and the latter operator is the one used here. The coefficient Km^2 varies from mode to mode, but here only one is considered. The same method can be used if N is not constant, but only if the diffusion coefficient varies with height in a suitable manner.

We look for steady and linear solutions. The appropriate scaling for the problem is

$$\begin{aligned} [x, y] &\equiv R = \frac{\sqrt{g'H'}}{f} & [p] &= fUR\rho_0 & [Q] &= Q_0 \\ [u_1, u_2, v_1, v_2] &= U = \frac{QR}{H'} & [h] &= \frac{fUR}{g'} & [\tau] &= T_0 \end{aligned}$$

where $g' = g \frac{\rho_2 - \rho_1}{\rho_0}$ and $H = \frac{H_1 H_2}{H_1 + H_2}$.

The resulting nondimensional equations are

$$\begin{aligned}
 -v_1 &= -p_x - \epsilon_1(u_1 - u_2) + \frac{T_0}{fQ_0R} \tau^{(x)} \\
 u_1 &= -p_y - \epsilon_1(v_1 - v_2) + \frac{T_0}{fQ_0R} \tau^{(y)} \\
 u_{1x} + v_{1y} &= -\frac{H'}{H_1} Q + \frac{H'}{H_1} \epsilon_2 h
 \end{aligned} \tag{2.3}$$

$$\begin{aligned}
 -v_2 &= -(p+h)_x - \epsilon_1(u_2 - u_1) \\
 u_2 &= -(p+h)_y - \epsilon_1(v_2 - v_1) \\
 u_{2x} + v_{2y} &= \frac{H'}{H_2} Q - \frac{H'}{H_2} \epsilon_2 h
 \end{aligned}$$

where $\epsilon_1 = \frac{\epsilon_1^*}{f}$ and $\epsilon_2 = \frac{\epsilon_2^*}{f}$.

(If the primary driving force were the wind, velocity would be scaled according to wind stress T_0 and not mass transfer Q_0).

We would like to look separately at the baroclinic and barotropic flows and therefore form the sum and difference equations with $\bar{u} = u_1 + u_2$ and

$\hat{u} = u_2 - u_1$:

$$\begin{aligned}
 -\bar{v} &= -(2p + h)_x + \frac{T_0}{fQ_0R} \tau^{(x)} \\
 \bar{u} &= -(2p + h)_y + \frac{T_0}{fQ_0R} \tau^{(y)}
 \end{aligned} \tag{2.4a}$$

and

$$H_1(u_{1x} + v_{1y}) + H_2(u_{2x} + v_{2y}) = 0$$

$$\begin{aligned}
 -\hat{v} &= -h_x - 2\epsilon_1 \hat{u} - \frac{T_0}{fQ_0R} \tau^{(x)} \\
 \hat{u} &= -h_y - 2\epsilon_1 \hat{v} - \frac{T_0}{fQ_0R} \tau^{(y)} \\
 \hat{u}_x + \hat{v}_y &= Q - \epsilon_2 h
 \end{aligned} \tag{2.4b}$$

If we now introduce a stream function Ψ for the baroclinic solution which is

geostrophic to lowest order ($\psi^{(0)} = h$), and arbitrarily assume that $2\epsilon_1 = \epsilon_2 = \epsilon$, the baroclinic vorticity equation is approximately

$$\epsilon \nabla_H^2 h + \beta h_x - \epsilon h = -Q - \frac{T_0}{fQ_0} (\tau_x^{(y)} - \tau_y^{(x)}) \quad (2.5)$$

The boundary conditions are for no normal flow through any barriers, that is

$$\begin{aligned} \hat{u} = -h_y - \epsilon \hat{v} &= 0 & \text{at meridional barriers} & \quad (2.6) \\ \hat{v} = h_x + \epsilon \hat{u} &= 0 & \text{at zonal barriers} & \end{aligned}$$

(In general, the apparently more rigorous conditions $u_1 = u_2 = 0$ or $v_1 = v_2 = 0$ will be met by solutions with boundary conditions (2.6) as long as no extra conditions are put on the flow.)

III. Meridionally Uniform Flow

i) f plane, $\zeta = 0$

We will begin with the simplest possible case: steady, meridionally uniform forcing of the form $Q(x)$ on the f plane with no wind stress, in a channel of width $2L$ centered at $x = 0$. The f plane, y independent vorticity equation which must be satisfied is

$$\epsilon (h_{xx} - h) = -Q \quad (3.1a)$$

subject to the boundary conditions $u = -\epsilon h_x = 0$ at $x = \pm L$.

The simplest subcase of this is uniform sinking everywhere, $Q = A$. The equally simple result is that

$$h = \frac{A}{\epsilon} \quad (3.2)$$

In other words, the upward motion of the interface due to uniform sinking everywhere is balanced by upward diffusion everywhere. There are no velocities associated with this displacement.

If we allow for x variation in the forcing so that $Q = Ax$, the principle balance in the interior is still between forcing and diffusion (the particular solution to (2.5) is $h = \frac{Ax}{\epsilon}$). However, because the interface is now tilted, meridional geostrophic velocities are generated which have zonal $O(\epsilon)$ velocities associated with them. The resulting solution which satisfies the no normal flow boundary conditions at $x = +L$ is

$$h = \frac{A}{\epsilon} x - \frac{\sinh x}{\cosh L} \quad (3.3)$$

which is the interior particular solution corrected with boundary layers at the two walls. In the neighborhood of the wall $x = L$, the solution (3.3) is of the form $h = \frac{A}{\epsilon} (x - e^{x-L})$ with an exponential boundary layer correction. The dimensional width of the boundary layers is the Rossby radius $R = \frac{\sqrt{g'H'}}{f}$. If we had retained the separate friction and diffusion parameters $2\epsilon_1$ and ϵ_2 from 2.4b), the dimensional boundary layer width would be $\sqrt{\frac{2\epsilon_1}{\epsilon_2}} \sqrt{\frac{g'H'}{f}}$. As the "friction" $2\epsilon_1$ is increased the boundary layer width increases, and as "diffusion" ϵ_2 is increased, the boundary layer width decreases.

The boundary layers result from the deformation of the interface at the wall caused by the nonzero zonal velocities in the interior. As the interface is pushed up or down, geostrophic boundary currents are created which in turn have $O(\epsilon)$ zonal velocities associated with them which oppose the interior zonal

flow. A balance is achieved in the boundary layer where the up or downwelling caused by interior zonal velocities is exactly balanced by diffusion. A schematic diagram of this flow is shown in Fig. 2 where the velocities associated with the two parts of the solution are shown separately.

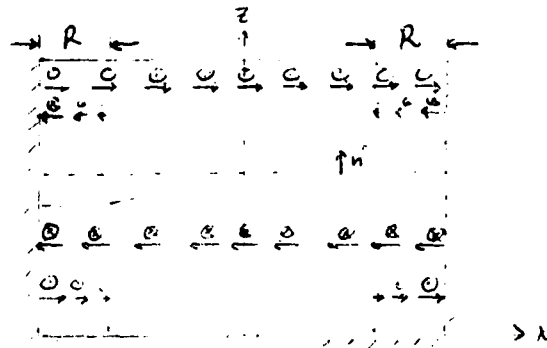


Fig. 2. Cross section of the flow associated with the sink $Q = Ax$, f plane. The upper row of velocities in each layer are the velocities associated with the interior solution while the lower row of velocities are associated with the boundary correction.

If we go to more complicated y independent forcing of the flow, the only additional result is that the interior flow gains relative vorticity in addition to an interface displacement. The boundary layer structure remains the same. An example of this is the flow due to the transfer $Q = A \sin kx$ which has the full solution

$$h = \frac{A}{\epsilon(1+k^2)} \left(\sin kx - \cos kL \frac{\sinh x}{\cosh L} \right). \quad (3.4)$$

The interior solution thus has both relative vorticity as well as an interface displacement while the boundary correction is still the familiar exponential correction.

(One further note is that $Q = A \sinh x$ causes a resonant response which no amount of damping can cause to be steady.)

(ii) f plane, $Q = 0$

If a north-south wind blows through the channel an additional component of zonal velocity is induced, namely, the Ekman flux at right angles to the wind. It is not strictly correct to include the wind in this model since there is no bottom friction to damp out the barotropic component of wind induced stress without further damping. Because a nonzero Ekman flux can arise from a uniform wind, we get interior $O(\epsilon)$ velocities for $O(1)$ boundary currents without interior interface displacement. If, for instance, $\tau = \hat{j} T_0$, the full solution is

$$\begin{aligned} h &= - \frac{T_0 \sinh x}{\epsilon \cosh L} \\ \hat{u} &= - T_0 \left(1 - \frac{\cosh x}{\cosh L} \right) \\ \hat{v} &= - T_0 \frac{\cosh x}{\epsilon \cosh L} \end{aligned} \tag{3.5}$$

in which the zonal velocity $\hat{u} = -T_0$ is compensated by boundary currents in

both sides. (The equations have been rescaled with $R = \frac{T_0}{f^2} \frac{H'}{H}$.)

iii) β plane

Inclusion of variations of the Coriolis parameter allows for the possibility of different vorticity balances, as is well known in studies of steady ocean circulation where interior change in planetary vorticity occurs more readily than interior change in relative vorticity. Inclusion of vortex stretching in steady β plane ocean circulation models can modify boundary layer and possibly interior balances, depending on the magnitude of the diffusion relative to the β effect.

The vorticity equation (2.5) is a steady statement of the potential vorticity equation

$$\frac{D}{Dt} \left(\frac{\nabla_H^2 h + f}{h} \right) = -Q - \epsilon \nabla_H^2 h + \epsilon h \quad (3.6)$$

where we allow for diffusion in addition to frictional dissipation. We can find solutions to (2.5) directly from the equation and boundary conditions or use the Longuet-Higgins transformation to get us back to an f plane type equation which has already been solved for various transfers Q . That is, letting $h(x,y) = \varphi(x,y)e^{\kappa x}$ where $\kappa = -\frac{\beta}{2\epsilon}$, equation (2.5) (without wind stress) becomes

$$\nabla_H^2 \varphi - (\kappa^2 + 1)\varphi = -\frac{Q}{\epsilon} e^{-\kappa x} \quad (3.7)$$

Uniform forcing $Q = A$ yields the same solution as on the f plane, $h = \frac{A}{\epsilon}$. The balance is still purely between the input of vorticity by the source-sink

and diffusion. Linear forcing $Q = Ax$ implies a slightly different particular solution

$$h_p = \frac{A}{\epsilon} \left(x + \frac{\beta}{\epsilon} \right)$$

which is the linear f -plane solution shifted to the west by the β effect.

Using (3.7) to obtain a full solution we find that

$$h = \frac{A}{\epsilon} \left(x + \frac{\beta}{\epsilon} \right) + \frac{A}{\epsilon} \left(k \frac{\cosh KL}{\cosh \sqrt{k^2+1} L} + \sqrt{k^2+1} \frac{\sinh KL}{\sinh \sqrt{k^2+1} L} \right) e^{kx} \cosh \sqrt{k^2+1} x \\ + \frac{A}{\epsilon} \left(k \frac{\sinh KL}{\sinh \sqrt{k^2+1} L} + \sqrt{k^2+1} \frac{\cosh KL}{\cosh \sqrt{k^2+1} L} \right) e^{kx} \sinh \sqrt{k^2+1} x .$$

Clearly, on the β plane it makes more sense to look at approximate solutions in various regions of the basin rather than solving the problem exactly.

The general solution from which (3.8) was obtained is

$$h = c_1 e^{\left(\sqrt{\frac{\beta^2}{2\epsilon} + 1} - \frac{\beta}{2\epsilon} \right) x} + c_2 e^{-\left(\sqrt{\frac{\beta^2}{2\epsilon} + 1} + \frac{\beta}{2\epsilon} \right) x} \quad (3.9)$$

Even without solving explicitly for c_1 and c_2 , we can see that near an eastern boundary, the dominant first term will yield a boundary layer width of

$$\frac{1}{\sqrt{\frac{\beta^2}{2\epsilon} + 1} - \frac{\beta}{2\epsilon}}$$

which is larger than the boundary layer width near a western boundary,

$$\frac{1}{\sqrt{\frac{\beta^2}{2\epsilon} + 1} + \frac{\beta}{2\epsilon}}$$

The term $e^{-\frac{\beta}{\epsilon} x}$ skews the entire solution to the west. For $\frac{\epsilon}{\beta} \ll 1$, the x dependence of the eastern and western boundary layer is approximately $e^{\frac{\epsilon}{\beta} x}$ and $e^{-\frac{\beta}{\epsilon} x}$ respectively, illustrating even more simply the shift to the west.

On the f plane, the vorticity balance in both the interior and boundary regions includes relative vorticity, diffusion and forcing, i.e. all of the

terms available, except in the case of especially simple forcing. On the β - plane, the extra planetary vorticity term has the effect of allowing different balances in different parts of the basin. If the interface height varies slowly with x , such that $x = \frac{\lambda}{\epsilon}$, the vorticity equation (2.5) becomes

$$\epsilon^3 h_{xx} + \epsilon (\beta h_x - h) = -Q$$

so the dominant balance is clearly

$$\beta h_x - h = -\frac{Q}{\epsilon} \quad (3.10)$$

whose solution corresponds to a broad eastern boundary layer, dominated by changes in planetary vorticity and vortex stretching.

If $\beta \gg \epsilon$ (2.5) becomes

$$\beta h_x = -Q \quad (3.11)$$

which is the classical Sverdrup balance. Diffusion is not at all important here and will also not be important in the western boundary layer. The Sverdrup balance can perhaps be thought of as a limiting case of the eastern boundary layer from (3.10).

In regions where the interface height varies rapidly with x , such that $x = \epsilon X$, the vorticity equation (2.5) becomes

$$h_{XX} + \beta h_x = 0 \quad (3.12)$$

whose solutions correspond to a narrow western boundary layer, dominated by changes in relative and planetary vorticity.

Thus, with the β term we can match solutions in various regions in addition to trying to solve the problem exactly. For example, the problem solved exactly above with $Q = Ax$ can be solved approximately with (3.10) and (3.12) and found to be

$$h = h_{east} + h_{west} \sim \frac{A}{\epsilon} \left(x + \frac{\beta}{\epsilon}\right) - \frac{A}{\epsilon} \frac{\beta}{\epsilon} e^{\frac{\epsilon}{\beta}(x-L)} - \frac{A}{\beta} \left(1 - e^{-\frac{2\epsilon}{\beta}}\right) e^{-\frac{\beta}{\epsilon}(x+L)}$$

a substantial simplification of (3.8) for $\frac{\epsilon}{\beta} \ll 1$.

On both the f and β planes we see that eastern and western boundary layers occur whenever the interior zonal velocity is nonzero, whether it is forced directly as an Ekman flux by the wind or more indirectly as a result of the geostrophic flow due to divergences created by mass transfer or wind stress curl. Steady solutions with this boundary layer structure are possible only because of the diffusion term ϵh which allows a damped form of vortex stretching to occur in steady flow.

With the structure of solutions on the f and β planes for meridionally uniform flow in mind, we move to forcing which may vary with latitude.

IV. Zonally Uniform Forcing in a Meridional Channel

What is the result of cooling which varies with latitude? As a simple case, we will consider cooling which is uniform and positive (transfer to the lower layer) in a northern basin and zero to the south with a transition region between which is wider than the Rossby radius but not as wide as $\frac{1}{\epsilon}$. (We could equally well choose any uniform value for the two halves of the basin.) We have in mind an enclosed sea like the Norwegian Sea but make the simplifications that a) the basin length is greater than $\frac{1}{\epsilon}$ and b) curvature of the basin occurs on a scale larger than the Rossby radius.

The geometry we are considering is illustrated in Fig. 3. For simplicity we will assume that $Q = A$ for $y > 0$, $Q = 0$ for $y < -M$ and $Q = A(1 + \frac{y}{M})$ in the transition region. This will necessarily lead to discontinuity in the zonal velocity at $y = 0, -M$ but is simple to solve, and has the essential features of a solution with smoother forcing.

The vorticity equation becomes

$$\epsilon(h_{xx} + h_{yy}) - \epsilon h = -Q \quad (4.1a)$$

subject to the boundary conditions

$$\begin{aligned} u &= -hy - \epsilon h_x = 0 \text{ at } x = \pm L \\ h &= 0 \quad \quad \quad \text{at } y = -M \\ h &\text{ continuous at } y = 0 \end{aligned} \tag{4.1b}$$

We consider the solution in three stages: i) solution for $-M < y < 0$ with no x dependence, ii) solution near $x = \pm L$ with large scale variation in y and iii) matching the solutions in the corner near $x = L, y = 0$. It will be seen that variation in forcing Q with latitude allows Kelvin wave-like disturbances to be found far to the north in the region of uniform Q which would otherwise be undisturbed. Thus we may in some way be able to model a more global forcing of the eastern boundary current in the Norwegian Sea than we could otherwise obtain with local winds and forcing.

i) The solution for $-M < y < 0$ with $\frac{\partial}{\partial x} = 0$ is just the particular solution

$$h = \frac{A}{\epsilon} \left(1 + \frac{y}{M} \right) \tag{4.2}$$

which has a zonal geostrophic velocity $u = -\frac{A}{\epsilon M}$ and meridional Ekman velocity $\hat{v} = -\epsilon h_y = -\frac{A}{M}$ associated with it. Thus for $A > 0$, there is an eastward (and northward) density current in the upper layer and the opposite in the lower layer.

ii) In the regions where $Q = A$ and $Q = 0$, we stretch the y coordinate by ϵ so that $y = \frac{Y}{\epsilon}$. The vorticity equation (4.1a) is then approximately (to $O(\epsilon)$)

$$h_{xx} - h = -\frac{Q}{\epsilon}$$

subject to the boundary conditions

$$\hat{u} = -\epsilon(h_y + h_x) = 0 \text{ at } x = \pm L.$$

Letting

$$h = \frac{A}{\epsilon} + C_1(Y)e^{x-L} + C_2(Y)e^{-(x+L)}$$

the only solution which decays away to the north, where $Q = A$, is

$$h = \frac{A}{\epsilon} + C_1 e^{-Y+x-L}$$

and likewise, the solution which decays away to the south, where $Q = 0$, is

$$h = c_2 e^{Y-(x+L)}$$

if there were a wall to the south at $x = -L$. These correspond to boundary layers with width equal to the Rossby radius R_0 and length of $\frac{R_0}{\epsilon}$, decaying away from the region of varying Q . Considering only the solution to the north, the constant c_1 can be determined by matching transports in the boundary layer at $y = 0$ with the eastward transport in $-M < y < 0$. We thus obtain

$$h = \frac{A}{\epsilon} (1 - e^{-\epsilon y + x - L}) \quad y > 0 \quad (4.3)$$

for the boundary layer decaying away to the north.

iii) In the corner near $y = 0$, $x = L$, the vorticity equation is

$$h_{xx} + h_{yy} - h = -\frac{A}{\epsilon} \left(1 + \frac{y}{M}\right)$$

subject to the boundary condition

$$\begin{aligned} \hat{u} = -h_y &= 0 && \text{at } x = L \\ h &= 0 && \text{at } y = -M \\ h &= \frac{A}{\epsilon} (1 - e^{x-L}) && \text{at } y = 0 \end{aligned}$$

The vorticity equation is separable and the solution which fits the boundary conditions is

$$h = \frac{A}{\epsilon} \left(1 + \frac{y}{M}\right) (1 - e^{x-L}) \quad -M < y < 0 \quad (4.4)$$

The full solution for the basin is

$$h = \begin{cases} \frac{A}{\epsilon} (1 - e^{-\epsilon y + x - L}) & y > 0 \\ \frac{A}{\epsilon} (1 + \frac{y}{M})(1 - e^{x-L}) & -M < y < 0 \\ 0 & y < -M \end{cases} \quad (4.5)$$

We note particularly that the zonal velocity is identically zero for $y > 0$ (a characteristic of a Kelvin wave) and that there is a nonzero geostrophic meridional velocity along the eastern coast for $y > 0$ which is solely due to the variation in Q from $-M < y < 0$. The upper layer velocities associated with the interface displacement (4.5) are shown schematically in Fig. 3.

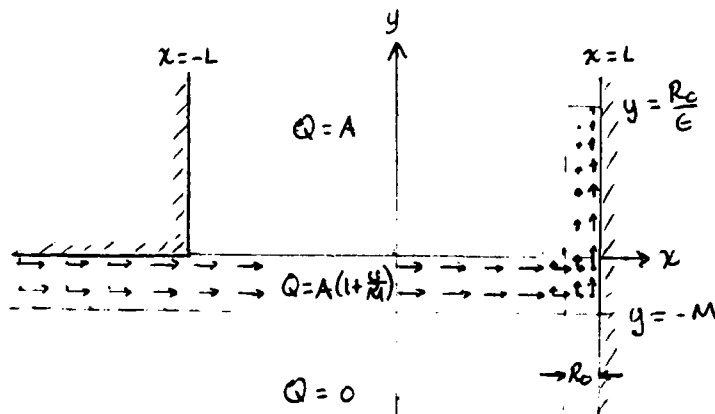


Fig. 3. Geometry and velocities when $Q = Q(y)$: specifically, $Q = A$ for $y > 0$, $Q = A(1 + \frac{y}{M})$ for $-M < y < 0$ and $Q = 0$ for $y < -M$.

It appears then that the steady signature of the Kelvin wave, which would arise in the time dependent case and travel up the eastern coast to the north, is a boundary current which eventually damps out to the north due to friction. Therefore, even in a region where variation in forcing is too weak to provoke a flow, there can be flow due to variation in the forcing elsewhere

(if variation is on a scale less than $\frac{1}{\epsilon}$). The mechanism is quite simple: the eastward flowing density current (upper layer) reaches the wall and causes a downward displacement of the interface which eventually reaches a diffusive equilibrium. Geostrophic velocities to the north (upper layer) along the boundary result and damp out on the frictional scale $\frac{1}{\epsilon}$. (The Ekman velocity associated with the geostrophic velocity in the region $-M < y < 0$ balances the incoming flow so that it is zero at the wall). Zonal Ekman velocities in the northward extension which are generated by the geostrophic northward velocities are exactly balanced by geostrophic zonal velocities due to the variation in interface height with latitude y (as a result of damping).

Extension of these results to the β plane is quite simple and involves expanding the eastern boundary layer width by $\frac{\epsilon}{\beta}$ (for $\frac{\epsilon}{\beta} \ll 1$), the familiar skewing of the circulation to the west. Damping to the north also occurs over a scale expanded by $\frac{\epsilon}{\beta}$. If we think of the boundary current as a damped Kelvin wave, the extension of the layer to the west can perhaps be thought of as damped nondispersive Rossby waves.

Combination of variation of forcing with both latitude and longitude can thus give rise to wide eastern boundary currents and narrow western boundary currents. Forcing in the Norwegian-Greenland Sea is irregular but the general trend is for much higher heat flux to the north (Bunker and Worthington, 1976) and a general cyclonic wind stress pattern. The wide northward flowing eastern boundary current which is observed in the southern Norwegian Sea (Metcalf, 1960) may be the result of latitudinal variation in cooling and/or wind stress south of the entrance to the Norwegian Sea, local northward or cyclonic wind stress, or local cooling. We note that an eastern boundary current at a particular latitude can be caused only by 1) local forcing which

produces a zonal flow that must be compensated at the boundaries or 2) variations in forcing to the south of that latitude which produces a damped Kelvin wave northward of the variation. Therefore, variations in forcing or forcing itself to the north of that latitude have no influence on the eastern boundary current there.

V. Point Transfer on the f and β planes

Bottom Water formation may occur locally and sporadically near the center of cyclonic gyres where the stratification is weakest due to doming of the previously formed Bottom Water. It may be possible to model some aspects of the flow due to Bottom Water formation with the steady model considered so far. For this purpose, we will simply assume that mass and momentum transfer is a delta function and look for steady solution. No account is taken of wind stress, preconditioning, or the spin up or spin down which *must undoubtedly* occur with a time dependent process. Modification of the flow by the β effect is considered. In reality, the Greenland gyre may be very strongly influenced by topography since it appears to sit squarely in the Greenland Basin.

On the f plane, the vorticity equation for a point source $Q = \frac{\delta(r)}{r}$ with no angular dependence is

$$\frac{1}{r} \frac{\partial}{\partial r} \left(r \frac{\partial h}{\partial r} \right) - h = -\frac{\delta(r)}{\epsilon r} \quad (5.1)$$

which has solutions $K_0(r)$ and $I_0(r)$ with the jump condition

$$\left[r \frac{\partial h}{\partial r} \right] = -\frac{1}{\epsilon} \quad \text{at } r = 0.$$

Choosing the exponentially decaying solution $h = AK_0(r)$, the interface height and azimuthal and radial velocities for large r are

$$\begin{aligned} h &\sim A \sqrt{\frac{\pi}{2r}} e^{-r} \\ \hat{u}_\theta &\sim \frac{\partial h}{\partial r} \sim -A \sqrt{\frac{\pi}{2r}} e^{-r} \\ \hat{u}_r &\sim -\epsilon \hat{u}_\theta \sim \epsilon A \sqrt{\frac{\pi}{2r}} e^{-r}. \end{aligned} \tag{5.2}$$

This corresponds to outward velocity, clockwise rotation and cyclonic vorticity in the lower layer and the opposite in the upper layer, as illustrated in Fig. 4. Cyclonic vorticity in the lower layer arises from point vortex stretching at $r = 0$. The vorticity decreases away from the center as the water parcels move outward and are squashed. Clockwise rotation in the lower layer clearly arises from outward motion of water parcels in a counterclockwise rotating system due to angular momentum conservation.

On the β plane, the flow is skewed to the west as expected. Using the Longuet Higgins transformation, the interface height is easily seen to be

$$h = AK_0(\sqrt{\kappa^2 + 1} r) e^{\kappa x} \quad \text{where} \quad \kappa = -\frac{\beta}{2\epsilon}.$$

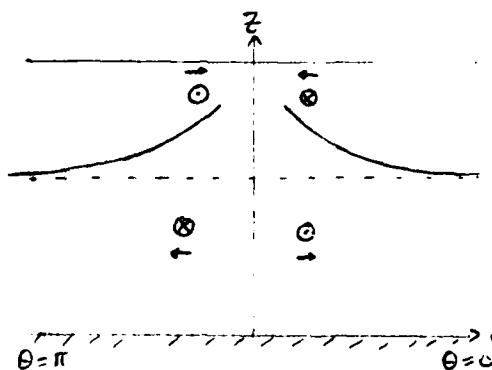


Fig. 4. Interface height h and velocities associated with $Q = \frac{\delta(r)}{r}$ on the f plane.

For large r , this becomes

$$h \sim A \sqrt{\frac{\pi}{2\sqrt{k^2+1}}} e^{r(-\sqrt{k^2+1} + k \cos \theta)}$$

If $|k| = \frac{\beta}{2\epsilon}$ is sufficiently large, we have

$$h \sim A \sqrt{\frac{\pi\epsilon}{\beta r}} e^{r \frac{\beta}{2\epsilon} (1 - \cos \theta)}$$

The loci of constant phase $r(1-\cos \theta)$ are parabolas which open to the west (Rhines, 1979 lecture notes) and mass transfer is clearly predominantly to the west.

Thus, on both the f and β planes, a point transfer of mass and momentum generates a steady counterclockwise flow in the upper layer and clockwise flow in the lower layer with the highest velocities near the transfer point. This type of flow in the upper layer accords with observations of counterclockwise flow in the Greenland Sea (Metcalf, 1960). It is, however, not to be forgotten that the wind stress in this region also yields a counterclockwise gyre, so perhaps the effects reinforce each other in the production of the gyre and in Bottom Water formation.

VI. Summary

Inclusion of a representation of diffusion in the continuity equation appears to be a useful way of damping the circulation resulting from a steady transfer of mass and momentum from one layer to another. With this term included in the vorticity equation it is possible to meet boundary conditions on the flow with boundary layers since the interface displacement at the boundaries can be an equilibrium between upwelling and diffusion.

The usual steady circulation models on the β plane cannot have eastern

boundary layers because there is no way to balance relative vorticity accession and changes in planetary vorticity on the eastern boundary. It is for this reason that boundary layers occur only in the west while the balance elsewhere is between forcing and changes in planetary vorticity (Sverdrup balance), in the usual β plane models. Inclusion of damping of vortex stretching in the form of the diffusion term ϵh in the vorticity equation allows the presence of western and eastern boundary layers. The western boundary layer still has the same structure as before, but the interior (eastern) solution includes diffusion as well, as long as $\frac{\epsilon}{\beta}$ is not too small.

Application of these results to the actual flow in the Norwegian-Greenland Sea may be somewhat tenuous but two features deserve mention. The first is the broad northward Norwegian Current which may possibly be modelled as the northern damped Kelvin wave extension of an eastward density or wind driven current in the northern North Atlantic. The second is the counterclockwise circulation in the Greenland Basin which may be partially driven by the formation of Bottom Water at its center and may be roughly modelled by the point transfer of Topography and wind may play a very large role in determining the actual circulation, which itself probably undergoes large seasonal variation.

Acknowledgements

I would like to express my gratitude to Dr. Adrian Gill for his patience in outlining the problem and help in understanding some of the rudiments of ocean modelling. The advice that he and other members of the Staff gave for formulating, carrying out, and talking about a research problem is much appreciated.

REFERENCES

- Bunker, A. F. and L. V. Worthington, 1976. Energy exchange charts of the North Atlantic Ocean. Bull. Am. Meteor. Soc., 57, 670-678.
- Carmack, E. and K. Aagard, 1973. On the deep water of the Greenland Sea DSR, 20, 687-715.
- Gill, A. F., J. M. Smith, R. P. Cleaver, R. Hide and P. R. Jonas, 1979. The vortex created by mass transfer between layers of a rotating fluid. Geophy. and Astrophy. Fluid Dynamics, 12, 195-220.
- Gill, A., 1979. GFD Lectures.
- Rhines, P., 1979. Class notes from "Mesoscale Ocean Dynamics".

A Study of Thermal Convection in a Rotating Annulus
with Applied Wind Stress and Surface Velocity

David Topham

I. Introduction

The circulation arising from a non-uniform distribution of surface temperature was suggested by Stommel as a model of oceanic circulation. It was proposed that heating at the equator would produce a thermocline in which downward thermal diffusion was balanced by upward convection flows. The sinking convective flows were confined to a small region at the poles (Stommel, 1958).

The broad features of this model were confirmed by laboratory experiments for a nonrotating system by Rossby (1965) who applied a linear temperature gradient to the bottom of a box, insulated on its other surfaces. The heat exchange was confined to a thin boundary layer at the bottom, while the convectively driven flow rose in a narrow plume against the hot wall. The interior fluid was almost uniform with a temperature excess approaching 70% of the maximum imposed temperature difference.

The corresponding problem in a rotating annulus has been solved by Stern (1975) for strong rotation with a linear temperature distribution. While Killworth (1979) considers the general problem and derives scaling parameters which identify six distinct flow regimes, ranging from the nonrotation case of Rossby to a limiting case of very strong rotation for which the convection flows are suppressed and a purely diffusive heat balance obtains. Killworth presents numerical computations of a special similarity solution ranging from no rotation to medium rotation conditions. The general effect of rotation is to inhibit the radial velocities and confine them to narrow Ekman layers.

This restriction of the convective flows causes a thickening of the thermal layer and a reduction of heat transfer in the system. In the strong rotation case considered by Stern the interior region of the fluid outside the thermal boundary layer assumes the temperature of the hottest end of the heated boundary. The rotating annulus has been explored in the laboratory by Hignett (1979) up to the medium rotation range. A wave-like instability was found for the higher rotation rates.

The problem addressed here is a modification of the rotating annulus in which additional boundary conditions are imposed, over and above that of the surface temperature distribution. In particular, two modifications of the conditions at the heated boundary are considered, an imposed distribution of surface velocity and an imposed distribution of surface stress. These additional boundary conditions can be arranged to either enhance or oppose the thermally driven flows; both cases are discussed. Both temperature and mechanical boundary conditions are considered to be applied at the bottom of the annulus.

2. Analysis

The following hierarchy of problems has been considered:

i) The rotating annulus with an applied variation of surface velocity and very small temperature difference, such that the heat can be regarded as a passive contaminant.

ii) The strong rotation case with strong thermal effects and small changes in the bottom velocity distribution, ie., weak mechanical driving.

iii) The limiting case of (ii) with strong mechanical driving

a) to enhance the thermal flows

b) to oppose the thermal flows.

iv) The strong rotation case with strong thermal effects where the boundary condition imposed is one of stress rather than velocity.

The notation employed follows that of Killworth (1979). The annulus is taken to have a radial separation L and height H , curvature is neglected and the origin is taken at the bottom lefthand corner, with the x -axis horizontal and the z -axis vertical. The imposed temperature along the x -axis (bottom) has its cold end at the origin. There is no variation of any of the parameters in the y direction. The buoyancy is defined as

$$\Delta' = -g \frac{(\rho' - \rho'_0)}{\rho_0}$$

where ρ'_0 is the density at the origin, g is the acceleration due to gravity, and primes denote dimensional variables.

The following seven dimensional quantities determine the system:

- Δ_m , the maximum imposed buoyancy difference
- L, H , the dimensions of the annulus
- ν , the kinematic viscosity
- κ , the thermal diffusivity
- f , the Coriolis parameter
- v'_s the maximum velocity imposed at the bottom boundary or in the case of stress driven systems $\frac{\partial N_s}{\partial z}$ is imposed.

From these the following nondimensional parameters can be formed:

$$\frac{\Delta_m L^3}{\nu \kappa} \equiv R_a \quad , \text{ the Rayleigh number} \quad (2.1)$$

$$\frac{\nu}{f L^2} \equiv E \quad , \text{ the Ekman number} \quad (2.2)$$

$$\frac{\nu}{\kappa} \equiv \sigma, \quad \text{Prandtl number} \quad (2.3)$$

$$\frac{H}{L} \equiv \gamma, \quad \text{the aspect ratio} \quad (2.4)$$

$$\frac{L v_s}{\kappa} \equiv P_v, \quad \text{Peclet number, velocity} \quad (2.5)$$

boundary condition

$$\frac{L^2 \left(\frac{dv_s}{dz} \right)_{z=0}}{\kappa} \equiv P_\tau, \quad \text{Peclet number, stress} \quad (2.6)$$

boundary condition

In addition, the form of the applied distribution of Δ , v_s and $\left(\frac{dv_s}{dz} \right)_{z=0}$ will influence the problem.

The following additional parameters are defined to facilitate comparison with the thermal driven results. Killworth demonstrates that the ratio of the thicknesses of the thermal and Ekman layers is the fundamental parameter determining the character of the thermally driven flows and defines

$$Q = Ra^{-2/5} E^{-1} \quad \text{or} \quad Q \equiv \frac{L^{4/5} \kappa^{2/5}}{\Delta_m^{2/5} \nu^{2/5}} f \quad (2.7)$$

Q therefore is a measure of the rotation rate of the system. Rossby showed that the thermal thickness scaled as $Ra^{-1/5}$ and the Ekman layer scales as $E^{1/2}$, Q is the square of the ratio of these thicknesses.

It is also convenient to introduce the parameter F in the case where a velocity boundary condition is imposed, where

$$F = \frac{v_s}{L f} = \sigma^{-1} E P_v \quad (2.8)$$

In the laboratory the use of water as a working medium gives the following orders of magnitude of the above parameters:

$$\begin{aligned} R_a &\sim 10^8 \\ E &\sim 10^{-4} \\ \sigma &\sim 10 \\ \gamma &\sim 1 \\ P_v &\sim 2 \times 10^2 \\ F &\sim 10^{-1} \text{ to } 1 \end{aligned}$$

The equations of motion can be written in the form

Vorticity

$$\nu \nabla^4 \psi' = \Delta'_x - f v'_z - J(\psi', \nabla^2 \psi') \quad (2.9)$$

Zonal momentum

$$\nu \nabla^2 v' = f \psi'_z + J(v', \psi') \quad (2.10)$$

Buoyancy

$$\kappa \nabla^2 \Delta + J(\psi', \Delta) = 0 \quad (2.11)$$

The absence of variation in the y direction implies the stream function ψ' , such that

$$u' = \psi'_z \quad w = -\psi'_x \quad (2.12)$$

∇^2 is the Laplacian operator $\left(\frac{\partial^2}{\partial x^2} + \frac{\partial^2}{\partial z^2}\right)$ and J the Jacobian operator $J(a,b) = a_x b_z - a_z b_x$, where the coordinate z takes on its appropriate scaled form for the different regimes considered.

For the case where the surface velocity v_s is prescribed the boundary conditions are

$$\begin{aligned} \psi' = \psi'_z = v' = v'_s(x') = \Delta' - \Delta'_0(x') = 0 \quad \text{at } z' = 0 \\ \psi' = \psi'_z = v' = \Delta'_z = 0 \quad \text{at } z' = H \\ \psi' = \psi'_x = v' = \Delta'_x = 0 \quad \text{at } x = 0, L \end{aligned} \quad (2.13)$$

An additional constraint is that there be no net heat flux from the fluid, expressed as

$$\int_0^L \Delta'_z dx' = 0 \quad \text{on } z' = 0 \quad (2.14)$$

Killworth (1979) and Killworth and Manins (1979) consider that the solution of the horizontal boundary layers and the interior is fully determined without a detailed consideration of the structure of the sidewall boundary layers. The same will be assumed for the modified bottom boundary conditions considered here.

3. Weak Heating with Imposed Surface Velocity

This can be considered as a small perturbation of the classic solution of a small differential rotation between top and bottom surfaces (Greenspan, 1968). The differential rotation produces Ekman layers on the horizontal surfaces, with a constant vertical Ekman suction velocity in the interior, which is in solid body rotation at one-half the differential rotation rate. The radial mass flow is transported from one Ekman layer to another via a side-wall shear layer of thickness of $O(E^{1/3})$. The flow pattern is illustrated in Fig. 1.

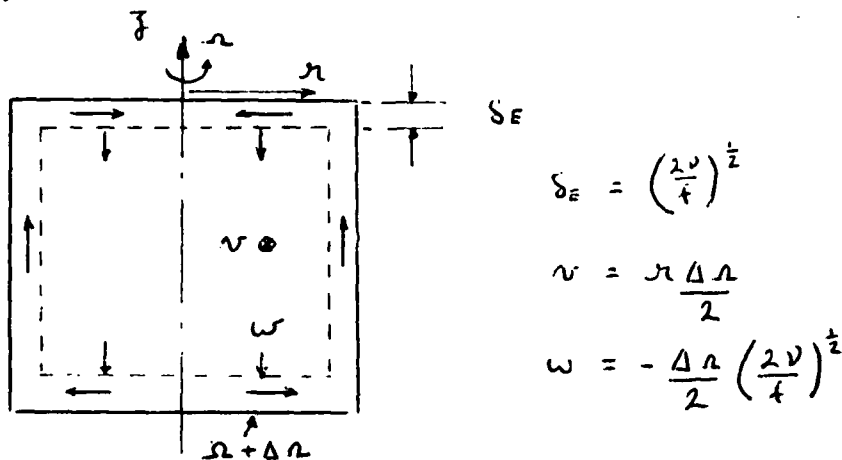


Fig. 1. The differentially rotating cylinder.

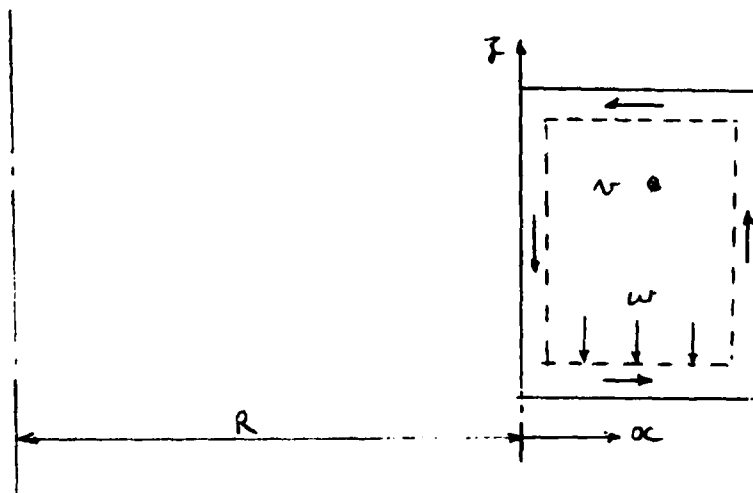


Fig. 2. The differentially rotating annulus.

If the annulus is considered as a geometrical extension of the differentially rotating cylinder, the velocity distribution on the bottom is given as $v_s = \Delta\Omega (R + x)$; the mass flow in the Ekman layers and the interior flow v increase as $(R + x)$ and the vertical velocity w is unchanged. The interior wall now requires a second vertical shear layer to balance the flow in the Ekman layers (Fig. 2). In the work which follows the geometrical constraint on the form of the imposed surface velocity, namely $v_s = \Delta\Omega (R+x)$ is relaxed and more general velocity distributions considered.

In practice it is found that the linear distribution $v_s = \alpha_0 x'$ affords the greatest mathematical simplification while retaining the essential physical features of the problem. In particular, it provides a vertical velocity which is independent of x , which affords considerable simplification in the strongly heated cases. The effects of weak heat addition to such a velocity driven system are now considered; the lower limit in which the heat acts as a passive contaminant is defined as the point where the velocity field is unaffected by the temperature field. Consider now the scaling appropriate to such a limit, where the imposed surface velocity is given by the relationship

$$v_s = \alpha_0 x'$$

The vertical velocity associated with this is

$$\frac{\psi'}{x'} = -w = \frac{\alpha_0}{2} \left(\frac{2\nu}{f} \right)^{1/2}$$

Making use of the definition of Ekman number (2.2) and the parameter F (2.8), yields the appropriate scaling for the stream function.

$$\psi' = K \sigma F E^{1/2}$$

The accompanying scaling for v' and Δ' are

$$v' = \nu FL^{-1} v \text{ and } \Delta' = \Delta_m \Delta, \text{ with a thermal layer.}$$

$$\delta_{TH} = L F^{-1} E^{-1/2}, \text{ where appropriate.}$$

Take equations of motion in the interior, where both x' and z' are scaled with L , take the form

Vorticity

$$E^{3/2} \nabla^4 \psi = Ra E F^{-1} \sigma^{-1} \Delta_x - v_z - E^2 F J(\psi, \nabla^2 \psi) \quad (3.1)$$

Zonal Momentum

$$E^{1/2} \nabla^2 v = \gamma_z + FE J(v, \psi) \quad (3.2)$$

Buoyancy

$$\nabla^2 \Delta + FE^{1/2} J(\psi, \Delta) = 0 \quad (3.3)$$

For the interior flows to be undisturbed it requires that

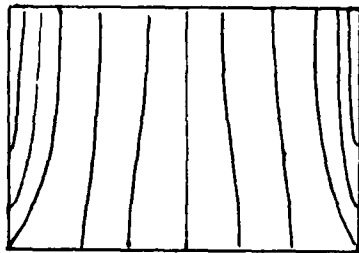
$$E \ll 1, F \ll E^{-1} \text{ and } Ra \ll FE^{-1}$$

if the low Rossby number velocity field is to be retained.

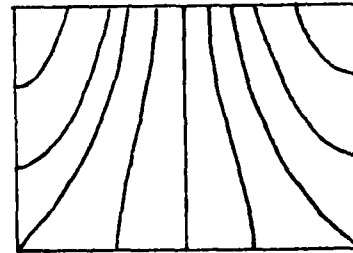
For the typical laboratory values quoted for water in the introduction the first two conditions are satisfied and the third requires that $Ra \ll 10^3$, say 10^2 , which would correspond to a maximum temperature difference of 10^{-5} °C across a 10 cm annulus, a weak heating indeed! There are two possibilities for the balance of the thermal layer; firstly, that the imposed vertical velocity is away from the heated wall, in which case no convective-

diffusive balance is possible and the thermal layer spreads over the interior, and secondly, that with the vertical velocity reserved a diffusive-convective equilibrium can be attained.

In the case where the thermal effects spread over the interior, the thermal balance will be diffusive if $F \ll E^{-1/2}$; increases in F above this limit will bring the convection terms into the balance, but will also introduce nonlinear terms into the equations of motion. The buoyancy distribution will be a modification of the purely diffusive case, where the convective term tries to reduce the vertical gradients. Figure 3 sketches the probable changes to a diffuse balance appropriate for a linear temperature distribution along the bottom of the annulus.



a) diffusive



1) diffusive & vertical convection

Fig. 3. Isotherms for a linear temperature distribution.

The flow within the Ekman layers is obtained by rescaling the equations in terms of a stretched vertical coordinate based on the expected Ekman layer, of thickness $O(E^{1/2})$. The above requirements for a passive thermal role then ensure the normal Ekman layer balance and give a diffusive thermal balance within the Ekman layer.

The second possibility, now arising from an Ekman section velocity towards the heated boundary, requires a further scaling of the equations to account for the smaller thermal layer thickness, now assumed to be small, compared to the height and of order κ/w .

$$\text{Thus } \delta_{th}/L \sim \kappa/LW \sim \kappa/L \psi'_z \sim F^{-1} E^{-1/2}$$

and the rescaled equations become

Vorticity

$$F^3 \nabla^4 \psi = Ra F^{-2} E^{5/2} \Delta_x - v_z - F^3 J(\psi, \nabla^4 \psi) \quad (3.4)$$

Zonal Momentum

$$F \nabla^2 v = \psi'_z + FJ(v, \psi) \quad (3.5)$$

Buoyancy

$$\nabla^2 \Delta + J(\psi, \Delta) = 0 \quad (3.6)$$

For a distinct thermal layer to exist, with an interior region above it, we require that $\delta_{th}/L < 1$ and also if the Ekman layer is to be thin, that $E^{1/2} \ll 1$. The condition that $\delta_{th}/L = F^{-1} E^{1/2} < 1$ can only be obtained for large values of F , which in turn implies that the nonlinear terms play a part in the equations of motion. Thus it is not possible to retain the low Rossby number flows of the mechanically driven system and have a distinct thermal layer with heat acting as a passive contaminant. For low Rossby number flows it is only possible to have a distinct thermal layer when the thermal effects play an active part in the dynamic balance. The coupled system is considered in detail in the next section.

4. Strong Rotation and Heating with Weak Mechanical Driving

This is an extension of the case treated by Stern (1975) and by Killworth for which an explicit solution can be obtained. The qualifications of strong heating and strong rotation ensure that the Ekman layer is thin compared to the thermal layer, which in return is thin compared to the height of the annulus.

Killworth's scaling for this case is

$$\begin{aligned}\psi' &= \kappa Ra^{1/5} Q^{-3/4} x \\ v' &= \kappa Ra^{2/5} Q^{-1/4} L^{-1} \hat{v}\end{aligned}$$

with the buoyancy layer of thickness $\delta_{TH} = L Ra^{-1/5} Q^{3/4}$.

The interior equations become

Vorticity

$$\nabla^4 x = Ra^{4/5} Q^{3/4} \Delta x - Ra^{3/5} Q^{3/2} \hat{v}_z - Ra^{1/5} Q^{-3/4} \sigma^{-1} J(x, \nabla^2 x) \quad (4.1)$$

Zonal Momentum

$$Ra^{-1/5} Q^{-1/2} \nabla^2 \hat{v} = \chi_z + \sigma^{-1} Q^{-5/4} J(\hat{v}, \chi) \quad (4.2)$$

Buoyancy

$$\nabla^2 \Delta + Ra^{1/5} Q^{-3/4} J(\chi, \Delta) = 0 \quad (4.3)$$

The requirement that there is to be no thermal wind in the interior is that

$$Ra^{4/15} \gg Q \gg 1$$

which yields a homogeneous interior with $\chi_z = \hat{v}_z = 0$.

Within the thermal layer a new stretched coordinate is defined

$$\mu = z' L^{-1} Ra^{1/5} Q^{-3/4}$$

and the rescaled equations become

Vorticity

$$Q^{-5/4} \nabla^4 \chi = \Delta_x - \hat{v}_\mu - Q^{-5/4} J(\chi, \nabla^2 \chi) \quad (4.4)$$

Zonal Momentum

$$Q^{-5/4} \nabla^2 \hat{v} = \chi_\mu + \sigma^{-1} Q^{-5/4} J(\hat{v}, \chi) \quad (4.5)$$

Buoyancy

$$\nabla^2 \Delta + J(\chi, \Delta) = 0 \quad (4.6)$$

or since the thermal layer is thin

$$\Delta_{\mu\mu} + J(\chi, \Delta) = 0$$

A further scaling appropriate to the Ekman layer of thickness $\delta_E = LE^{1/2}$,

defines the stretched coordinate as $\theta = z' L^{-1} Ra^{1/5} Q^{1/2}$

yielding

$$\chi_{\theta\theta\theta\theta} = -\hat{v}_\theta + o(Q^{-5/4}) \quad (4.7)$$

$$\hat{v}_{\theta\theta} = \chi_\theta + o(Q^{-5/4}) \quad (4.8)$$

$$\Delta_{\theta\theta} = -Q^{-5/4} (\chi_x \Delta_\theta - \chi_\theta \Delta_x) \ll 1 \quad (4.9)$$

Thus the Ekman layers are unchanged by the buoyancy to leading order.

Consider now that an arbitrary distribution of velocity is specified on the heated boundary

$$\hat{v}_s = \alpha(x)$$

The Ekman layer solutions become

$$(\hat{v} - \alpha) = (\hat{v}_0 - \alpha) \left[1 - e^{-\theta/\sqrt{z}} \cos \frac{\theta}{\sqrt{z}} \right] \quad (4.10)$$

$$\chi = -\sqrt{2} \chi_0 e^{-\theta/\sqrt{z}} \cos \left(\frac{\theta}{\sqrt{z}} - \frac{\pi}{4} \right) \quad (4.11)$$

$$u = \chi_0 = \sqrt{2} \chi_0 e^{-\theta/\sqrt{z}} \sin \frac{\theta}{\sqrt{z}} \quad (4.12)$$

$$\hat{v}_0 - \alpha = -\sqrt{2} \chi_0 \quad (4.13)$$

where the subscript zero denotes conditions just outside the Ekman layer.

In the thermal layer, the buoyancy equation (4.6) becomes

$$\Delta_{\mu\mu} + \chi_x \Delta_{\mu} - \chi_{\mu} \Delta_x = 0$$

or since $\chi_{\mu} = 0$, χ_x becomes $(\chi_I)_x$, where the subscript I denotes the interior conditions, and

$$\Delta_{\mu\mu} = -(\chi_I)_x \Delta_{\mu}$$

which has the solution

$$\Delta = \Delta_I + \left[\Delta_o(x) - \Delta_I \right] e^{-(\chi_I)_x \mu} \quad (4.14)$$

The lower boundary condition has been taken to be that of the heated boundary, by (4.9).

After differentiating (4.14) with respect to x , the thermal wind equation (4.4) can be integrated to give the v -component of velocity in the thermal layer.

$$\hat{v} - \hat{v}_o = - \frac{(\Delta_o)_x}{(\chi_I)_x} \left[e^{-(\chi_I)_x \mu} - 1 \right] - (\chi_I)_{xx} \left[\frac{(\Delta_o - \Delta_I)}{(\chi_I)_x} \frac{1 - e^{-(\chi_I)_x \mu}}{(\chi_I)_x} - \mu e^{-(\chi_I)_x \mu} \right] \quad (4.15)$$

The Ekman layer at the top boundary gives a second compatibility condition.

$$\hat{v}_I = \sqrt{2} \chi_I \quad (4.16)$$

where \hat{v}_I is the interior v -component of velocity.

Since $\chi_\mu = 0$ in the thermal layer, (4.13) gives

$$\hat{v}_o = \alpha - \sqrt{2} \chi_I$$

and substituting this value into (4.15), gives an equation for the interior value of the stream function.

$$2^{3/2} \chi_I - \alpha(\chi) = \left[\frac{\Delta_o(x) - \Delta_I}{(\chi_I)_x} \right]_x \quad (4.17)$$

This is a nonlinear second order equation in χ_I and Stern's (1975) solution corresponds to $\alpha = 0$ and a linear distribution of boundary temperature. Here, the approach of Killworth (1979) is followed in which

(4.17) is regarded as a linear equation for $(\Delta_0(x) - \Delta_I)$ in which $\chi_I(x)$ and $\alpha(x)$ are specified. In particular, both distributions are taken to be linear.

$$\alpha = \alpha_0 x, \quad \chi_I = \left(c + \frac{\alpha_0}{2\sqrt{2}} \right) x$$

equation (4.17) then becomes

$$\Delta_0(x) = \frac{c(2\sqrt{2}c + \alpha_0)x^2}{2}$$

if the boundary conditions on $\Delta_0(x)$ of $\Delta_0(0) = 0$ and $\Delta_0(1) = 1$ are imposed,

$$c = \frac{-\alpha_0}{4\sqrt{2}} + \sqrt{\frac{\alpha_0^2 + 16\sqrt{2}}{4\sqrt{2}}}$$

and

$$\Delta_0(x) = x^2$$

the form required for the similarity solution of Killworth and Manins (1979) and Killworth (1979).

Thus

$$\chi_I = \left[\frac{x}{4\sqrt{2}} \alpha_0 + \sqrt{\alpha_0^2 + 16\sqrt{2}} \right] \quad (4.18)$$

Killworth has shown that for the strong heating and strong rotation case considered here, the interior temperature Δ_I is that of the largest imposed values, here $\Delta_I = 1$.

The buoyancy distribution then becomes

$$\Delta = 1 + (x^2 - 1) \exp - \left[\frac{\alpha_0 + \sqrt{\alpha_0^2 + 16\sqrt{2}}}{4\sqrt{2}} \right] \mu \quad (4.19)$$

and the \hat{v} -component of velocity

$$\hat{v} = -\sqrt{2} \chi_I + \alpha_0 x - \frac{x^2}{(\chi_I)_x} \left(e^{-(\chi_I)_x \mu} - 1 \right) \quad (4.20)$$

In particular

$$\hat{v}_r = \frac{x}{4} \left[\alpha_0 + \sqrt{\alpha_0^2 + 16\sqrt{2}} \right] \quad (4.21)$$

$$\hat{v}_0 = -\frac{x}{4} \left[\sqrt{\alpha_0^2 + 16\sqrt{2}} - 3\alpha_0 \right] \quad (4.22)$$

$$w = -\frac{1}{4\sqrt{2}} \left[\alpha_0 + \sqrt{\alpha_0^2 + 16\sqrt{2}} \right] \quad (4.23)$$

The heat transfer from the heated boundary can be obtained by integrating (4.9) across the Ekman layer

$$\Delta_\theta = -Q^{-5/4} \frac{\partial}{\partial x} \left[\chi_r (\Delta_\theta(x) - \Delta_r) \right] \quad (4.24)$$

where the term $\chi_x \Delta_\theta$ has been neglected in comparison with $\chi_\theta \Delta_x$.

For the distributions of Δ_θ and α considered

$$\Delta_\theta = \frac{-Q^{-5/4}}{4\sqrt{2}} \left[\alpha_0 + \sqrt{\alpha_0^2 + 16\sqrt{2}} \right] (3x^2 - 1) \quad (4.25)$$

which changes sign at $x = 1/\sqrt{3}$.

The heat transfer efficiency is defined by the ratio of the actual heat transfer to that which would occur by diffusion alone, this defines the Nusselt Number for the system. Since there is no net heat loss from the system, the modulus of the heat flux is taken to define the Nusselt number.

$$Nu = \kappa \frac{1}{2} \int_0^L \left| \frac{d\Delta}{dz} \right| dx \bigg/ \kappa \frac{1}{2} \int_0^L \left| \frac{d\tilde{\Delta}}{dz} \right| dx$$

where $\partial \bar{\Delta} / \partial z$ is the gradient corresponding to a purely diffusive system, evaluated by Killworth and Manins for a $\Delta_0 = x^2$ buoyancy distribution and aspect ratio 1.0 as

$$\frac{1}{2} \int_0^L \left| \frac{\partial \bar{\Delta}}{\partial z} \right| dx = 0.312 K \Delta_m$$

Integration of (4.25) yields $\frac{1}{2} \int_0^1 \left| \frac{d\Delta}{dz} \right| dz = \frac{Q^{-5/4}}{6\sqrt{6}} \left[\alpha_0 + \sqrt{\alpha_0^2 + 16\sqrt{2}} \right]$

To express this in terms of Nusselt Number the scaling must be returned to dimensional form and in particular, the scaling of the parameter α_0 defined.

Now at $x = 1$, $\hat{v}_{z=0} = \alpha_0$, or introducing the scaling for velocity

$$\alpha_0 = (v_s')_{x=1} L K^{-1} Ra^{-2/5} Q^{1/4}$$

From the definitions (2.5) and (2.8)

$$\alpha_0 = \sigma F Q^{5/4} \quad (4.26)$$

and the heat transfer law can be expressed as

$$Nu = 0.218 \left[1 + \sqrt{1 + \frac{16\sqrt{2}}{F^2 Q^{5/2}}} \right] Ra^{1/5} Q^{1/2} F \quad (4.27)$$

when $F = 0$. this reduces to the strong rotation result of Killworth (1979)

$$Nu = 1.037 Ra^{1/5} Q^{-3/4}$$

The limiting forms of the solution will now be examined for the cases of large positive and negative values of F . If F is made increasingly large and positive, that is, the mechanically driven flows enhance the thermal flows, the solution becomes

$$\hat{v}_z = \hat{v}_0 = \frac{\alpha_0 x}{2}, \quad w = \frac{-\alpha_0}{2\sqrt{2}}$$

and
$$Nu = 0.436 Ra^{1/5} Q^{1/2} F$$

The velocity field therefore approaches that of the differentially driven system with no heat transfer, suggesting that the thermal layer has become the same thickness as the Ekman layer. In this extreme limit the scaling employed is no longer appropriate.

If, on the other hand, F becomes large and negative the mechanically driven flows will thicken the thermal layer by opposing the thermal flows. For negative values of F , the factor

$$\left[\alpha_0 + \sqrt{\alpha_0^2 + 16\sqrt{2}} \right] = \alpha_0 \left[-1 + \sqrt{1 + \frac{16\sqrt{2}}{\alpha_0^2}} \right]$$

Expanding the square root.

$$\left[\alpha_0 + \sqrt{\alpha_0^2 + 16\sqrt{2}} \right] \rightarrow \frac{8\sqrt{2}}{\alpha_0} \quad \text{as } \alpha_0 \rightarrow -\infty$$

and

$$\hat{v}_0 \rightarrow \frac{-\alpha_0 x}{2}, \quad v_x \rightarrow \frac{2\sqrt{2} x}{\alpha_0} \quad \text{and} \quad w \rightarrow \frac{-2}{\alpha_0}$$

and

$$Nu \rightarrow 2.466 Ra^{1/5} Q^{-2} F^{-1}$$

Thus it appears that it is not possible to reverse the thermally driven flows, only to weaken them. The effect of the ever increasingly negative surface velocity on the Ekman suction is cancelled by complimentary increases in the thermal wind velocity in the same direction. Again, the scaling is expected to break down for the extreme values.

It is of some interest to examine a numerical example in the context of a hypothetical experiment using the typical values of the parameters quoted in the Introduction. In both cases a value of σ_0 of 20 makes the limiting forms a good approximation. Taking a value of Q of 10, typical of laboratory conditions, and $F = 0.1$ would make about a tenfold change in the thickness of the thermal layer. It could thus seem feasible to exercise considerable control over the depth of the thermal layer. The nature of the mechanical driving is such that it is immaterial as to whether the heated boundary or the opposite one is driven. The limiting cases will not be explored in the light of more appropriate scalings.

5.0. The Limiting Case of Strong Positive Driving

As the thermal layer approaches the Ekman layer a new scaling is sought to relate the stream function to the mechanical driving. The following is found to be appropriate.

$$\begin{aligned}\psi' &= \kappa \sigma R a^{1/5} Q^{1/2} F \chi \\ v' &= \kappa \sigma R a^{2/5} Q F L^{-1} \hat{v} \\ z' &= L R a^{-1/5} Q^{-1/2} \theta\end{aligned}$$

The equations of motion in the thermal layer become

$$\begin{aligned}\chi_{\theta\theta\theta\theta} &= \sigma^{-1} F^{-1} Q^{-5/2} \Delta_x - \hat{v}_\theta - F J(\chi, \nabla^2 \chi) \\ \hat{v}_{\theta\theta} &= \psi_\theta + F J(\hat{v}, \chi)\end{aligned}$$

and the buoyancy equation

$$\Delta_{\theta\theta} + \sigma F J(\chi, \Delta) = 0$$

If Q is large and F small compared to unity the equations of motion are

uncoupled from the buoyancy equation and are the normal Ekman balances. For large Prandtl number the buoyancy equation has convection terms with the Ekman layer velocity distributions, solvable in principle, but difficult in practice.

If, however, the thermal layer can be reduced still further in height, the velocity distributions become linear as the bottom of the Ekman layer is approached. In this context it should be pointed out that the solution of the previous section indicates that the greater the value of Q , the smaller the value of F required to change the thermal layer by a given amount. Thus for large values of Q , F can still remain small and drastically reduce the height of the thermal layer.

Consider now a further scaling of the vertical coordinate suitable for the region where the velocity distributions are approximately linear. The thickness of the thermal layer δ_{TH} is of order κ/w_{TH} where w_{TH} is the vertical velocity at the edge of the layer, hence

$$\delta_{TH} \approx \frac{\kappa}{w_{TH}} \approx \frac{\kappa}{w_E} \left(\frac{\delta_E}{\delta_{TH}} \right)$$

where w_E is the Ekman suction velocity, $-\psi_x$ and

$$\frac{\delta_{TH}^2}{\delta_E} = \frac{\kappa}{w_E} \cdot \frac{1}{\delta_E} = \frac{\kappa}{\psi_x} \cdot \frac{1}{\delta_E}, \quad \text{where } \delta_E = LE^{1/2} \text{ applying the}$$

scaling for ψ' , $\psi' = \kappa \sigma Ra^{1/5} Q^{1/2} F$ and using the definition for Q ,

(2.7) gives a new vertical scaling

$$\zeta = \theta \sigma^{1/2} F^{1/2}$$

The Ekman layer velocity distributions (4.12), (4.11) for small values of become

$$u = \frac{\alpha_0 \theta x}{2\sqrt{z}} \quad \text{and} \quad w = - \frac{\alpha_0 \theta}{2}$$

Where the driving parameter must be interpreted in terms of the present scaling for v' giving

$$\alpha_0 = 1$$

The buoyancy equation now becomes

$$\frac{\partial^2 \Delta}{\partial \zeta^2} + \frac{\zeta}{2} \frac{\partial \Delta}{\partial \zeta} - \sigma^{-1/2} F^{-1/2} \frac{\zeta x}{2\sqrt{z}} \frac{\partial \Delta}{\partial x} = 0$$

For large values of $\sigma^{1/2} F^{1/2}$ as implied by the scaling, the terms in x become negligible and the equation reduces to the ordinary differential equation

$$\frac{d^2 \Delta}{d\zeta^2} + \zeta \frac{d\Delta}{d\zeta} = 0$$

subject to the boundary conditions $\Delta = \Delta_0(x)$ at $x = 0$ and to the integral constraint

$$\int_0^1 \frac{d\Delta}{d\zeta} d\zeta = 0 \quad \text{at} \quad \zeta = 0$$

For the boundary distribution $\Delta_0 = x^2$, the solution can be expressed in terms of the error function as

$$\Delta = x^2 + \frac{(1-3x^2)}{3} \operatorname{erf} \zeta \tag{5.1}$$

the interior buoyancy as $\zeta \rightarrow \infty$ is $1/3$.

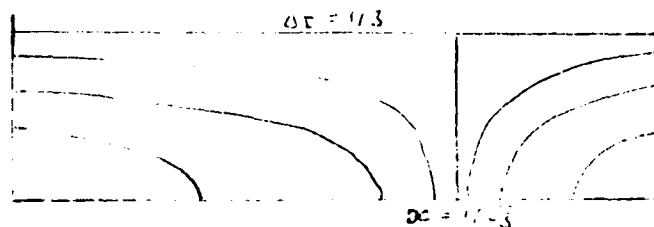
Equation (5.1) can be differentiated directly to give the boundary heat flux, and an integration along the boundary then yields.

$$\int_0^1 \left| \frac{d\Delta}{d\zeta} \right| dx = \frac{4}{9\sqrt{3\pi}}$$

After making the appropriate scaling changes the following expression is obtained for the Nusselt number.

$$Nu = 0.464 Ra^{1/5} Q^{1/2} F$$

The form of the isothermals appropriate to equation (5.1) are shown below (Fig. 4).



This solution is only valid for very large Prandtl numbers since if it becomes of order unity, the nonlinear terms play a part in the Ekman layer equations.

6.0 The Limiting Case of Strong Negative Driving

When the imposed surface velocities are such as to oppose the thermally driven flows, a new scaling must be found for the case where the thermal layer has become of the same order as the annulus height. The limiting case of section 4.0 suggests that the Ekman suction velocity w scales inversely with the parameter α_0 .

$$\psi' = \kappa Ra^{1/5} Q^{-2} F^{-1} \Psi, \quad v' = \kappa Ra^{2/5} Q F \hat{v}$$

$$\text{with } \delta_{TH} = Ra^{-1/5} Q^2 F L^{-1}$$

The scaled equations then become

$$\begin{aligned} Ra^{-3/5} Q^{-4} F^{-2} &= Ra^{1/5} Q^{-2} F^{-1} \Delta_x - \hat{v}_\mu - Ra^{-2/5} Q^{-6} F^{-3} \sigma^{-1} J(\psi, \nabla^2 \psi) \\ Ra^{-1/5} Q^2 F^2 \nabla^2 \hat{v} &= \psi_\mu + F \sigma^{-1} J(\hat{v}, \psi) \\ \nabla^2 \Delta + Ra^{1/5} Q^{-2} F^{-1} J(\psi, \Delta) &= 0 \end{aligned}$$

If the thermal layer is thinner than the depth of the annulus this gives uniform conditions in the interior. If, on the other hand, the thermal layer is of the same order of thickness as the height, ($Ra^{-1/5} Q^2 FL^{-1} \gg 1$), and $Ra^{1/5} Q^2$ is large, F remains small and the equations reduce to the thermal wind equation and a diffusive advective balance for the buoyancy equation. If the driving parameter F is increased further, the viscous terms in the zonal momentum equation play a part in the balance. The system can no longer respond by increasing the depth of the thermal layer, and the Ekman suction is controlled by the mechanical driving, the sign of w can reverse and blow away from the heated wall.

The situation has become similar to the passive case discussed in section 3.0 with the main circulation dictated by the mechanical driving, but a thermal wind throughout the annulus with a small zonal component u . The buoyancy balance is increasing dominated by the z directed velocity, with the heat transfer continuing to be reduced.

Summary of Results

Explicit solutions have been obtained for the case when the strongly heated, strongly rotating annulus has a linear distribution of surface velocity imposed on a horizontal boundary.

When the boundary condition is in the same rotation sense as the main rotation, the thermal layer is reduced in thickness with an increase in heat transfer. A solution has been obtained for the case of very strong mechanical driving where the thermal layer becomes very thin compared with the Ekman layer. In this case, the interior of the fluid attains the mean temperature of the heated wall rather than its hottest point, as is the case for zero to medium driving water.

In the case when the mechanically driven flows oppose the thermal flows the thermal layer is increased in height, due to a decrease in the vertical velocity component. The change most directly associated with the reversed boundary velocities is an increase in the thermal wind velocity just outside the Ekman layer. This progressively decreases the velocity difference across the Ekman layer as the surface velocity become increasingly negative, which in turn decreases the w-velocity component. When the thermal layer has increased in thickness to the point when it envelopes the opposite boundary, the velocity field becomes more directly controlled by the mechanical driving and the Ekman suction velocity can reverse.

The heat transfer results can be summarized in terms of the single parameter $Q^{5/4}F$, which represents the degree of mechanical driving in the system. It is, in fact, the nondimensional parameter $\alpha_0 \sigma^{-1}$ in the case of medium driving

Thermal driving only (Killworth, 1979)

$$\text{NuRa}^{-1/5} Q^{3/4} = 1.037$$

Medium driving, $1 \gg \delta_{TH} \gg \delta_E$

$$Nu Ra^{-1/5} Q^{3/4} = 0.218 \left[1 + \sqrt{1 + \frac{16J^2}{F^2 Q^{5/2}}} \right] Q^{5/4} F$$

Limit $F \rightarrow +\infty$

$$Nu Ra^{-1/5} Q^{3/4} \rightarrow 0.436 Q^{5/4} F$$

Limit $F \rightarrow -\infty$

$$Nu Ra^{-1/5} Q^{3/4} \rightarrow 2.466 Q^{-5/4} F^{-1}$$

Strong positive driving

$$Nu Ra^{1/5} Q^{3/4} = 0.464 Q^{5/4} F$$

These are shown as a single curve on Fig. 5. It should be remarked that the strong heating, strong rotation régime is found to be unstable in the laboratory, wave-like instabilities appearing for values of Q above about 3.4 (Hignett, 1979), and thus the régime for which the explicit solutions are valid may be inaccessible in the laboratory.

The case of a stress driven circulation will be treated in an appendix as an explicit solution can only be obtained for the case where applied stress is large.

Acknowledgments

My thanks are due to Dr. Melvin Stern and Dr. Peter Killworth for their suggestions and guidance during the course of this work. Also to the Staff, Visitors and Fellows of the G.F.D. Summer School for providing a most pleasant introduction to the subject.

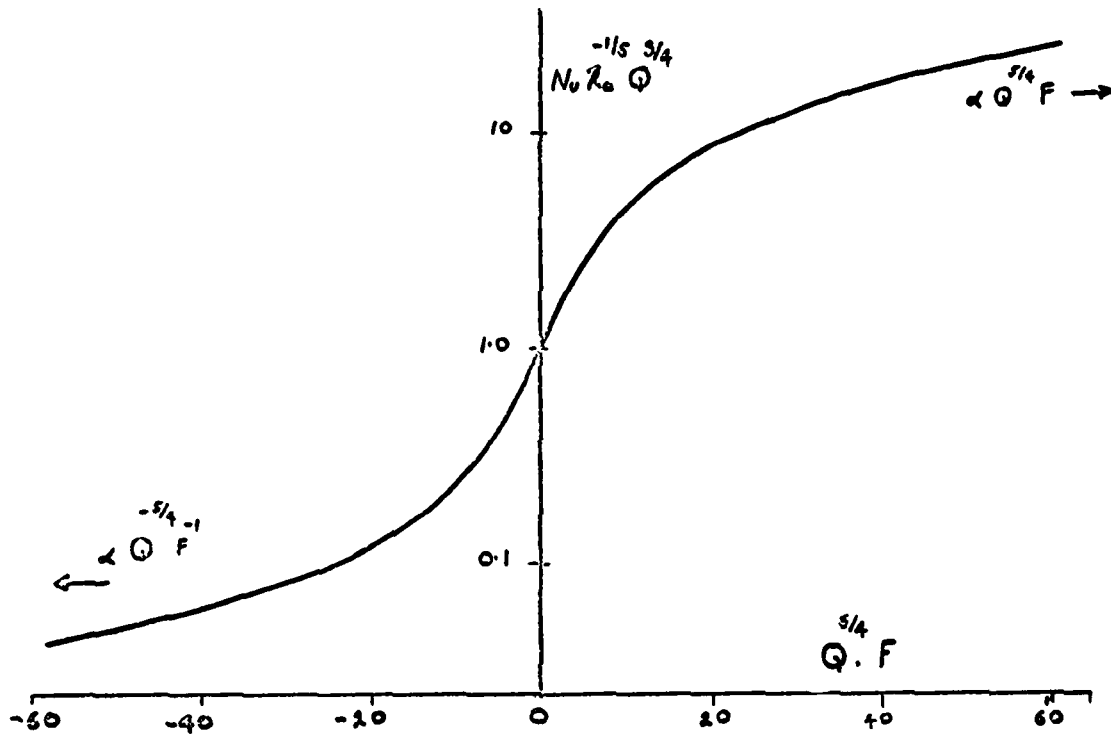


Fig. 5. Variation of Heat Transfer with Mechanical Driving

REFERENCES

- Greenspan, H. P., 1968. The theory of rotating fluids. Cambridge Univ. Press, London and New York.
- Hignett, P., 1979. Experiments on thermal convection in a rotating fluid annulus, driven by non-uniform heating from below. Phd. thesis, Univ. of Reading, England.
- Killworth, P. D. and Manins, 1979. A model of confined thermal convection driven by nonuniform heating from below. J.F.M. (in press).
- Rossby, H. T., 1965. On thermal convection driven by nonuniform heating from below: an experimental study. Deep-Sea Res., 12, 9-16.
- Stern, M. E., 1975. Ocean circulation physics. Academic Press, New York, San Francisco, London.
- Stommel, H., 1958. The abyssal circulation, Deep-Sea Res., 5, 80-82.

APPENDIX: THE STRESS DRIVEN CASE

Killworth (1979) discusses briefly the stress free boundary condition for the heated boundary, and gives the appropriate scaling parameters as

$$\psi' = \kappa Ra^{1/5} Q^{-2} \chi, \quad v' = \kappa Ra^{3/5} Q L^{-1}$$

with a thermal layer of thickness $LRa^{-1/5} Q^2$. The lack of stress at the boundary has reduced the mass flux in the bottom Ekman layer and the interior vertical velocity. The scaled equations then become for the thermal layer

$$\begin{aligned} Q^{-10} \nabla^4 \chi &= \Delta_x - \hat{v}_\mu - \sigma^{-1} Q^{-7} J(\chi, \nabla^2 \chi) \\ \nabla^2 \hat{v} &= \chi_\mu + \sigma^{-1} J(\hat{v}, \chi) \\ \nabla^2 \Delta + J(\chi, \Delta) &= 0 \end{aligned}$$

There is a thermal wind balance, but now the viscous and nonlinear terms become important in the zonal momentum equation, introducing u components of velocity. Thus, there is no analog of the simple solution obtained for the case with boundary stress.

For the case where the applied driving stress is strong enough to produce the same Ekman layer flows, as in the mechanically driven case, we may use the same equations and develop a "strong" stress driven solution.

The mass flux in the bottom Ekman layer is now given directly by the boundary stress, $\tau(x)$. In terms of the scaled parameters this can be written directly in terms of the stream function

$$\chi_o = \tau(x)$$

where the subscript o again denotes conditions at the bottom of the thermal layer. Since the equations of motion of section 4.0 yield $\chi_\mu = 0$, the interior value of the stream function is given as

$$\chi_I = \tau(x)$$

If a linear stress distribution is assumed

$$\tau = \tau_o x$$

the buoyancy equation has the solution

$$\Delta = \Delta_I + (\Delta_o(x) - \Delta_I) e^{-\tau_o \mu}$$

and integration of the thermal wind equation across the thermal layer gives

$$v_I - v_o = \int_0^\infty \frac{d\Delta}{dx} d\mu = \frac{(\Delta_o)_x}{\tau_o}$$

Hence we obtain, from the top Ekman layer

$$v_I = \sqrt{2} \chi_I = \sqrt{2} \tau_o x, \quad v_o = \sqrt{2} \tau_o x - (\Delta_o)_x / \tau_o$$

For the parabolic buoyancy distribution $\Delta_o = x^2$ and the interior buoyancy value $\Delta_I = 1.0$, as for the mechanically driven case, the boundary heat flux (4.25) becomes

$$\Delta_o = -Q^{-5/4} \frac{d}{dx} \left[\tau_o x (x^2 - 1) \right]$$

and

$$\int_0^1 \Delta_0 dx = -Q^{-5/4} \tau_0 \cdot 2/3\sqrt{3}$$

Changing to dimensional variables and dividing by the purely diffusive heat flux yields the heat transfer in terms of Nusselt number

$$N_u = 1.234 E P_\tau$$

where

$$P_\tau = \left[\frac{L^2}{\kappa} \left(\frac{dv'}{dz'} \right)_{z=0} \right]$$

$$\tau_0 = P_\tau Ra^{-3/5} Q^{-1/4}$$

The conditions under which this result is expected to hold are those when the Ekman suction velocity w_E , derived from the stress driving, is of the same order as that which would exist for the strong rotation case with heating and zero velocity boundary conditions. The solution for this case gives

$$w_{TH} = -2^{-1/4}$$

and with stress driven boundary conditions we have

$$w_E = -\tau_0$$

For there to be of the same order

$$\tau_0 \sim 2^{1/4} = 0.84$$

and the stress driven solution is valid when $\tau_0 = P_\tau Ra^{-3/5} Q^{-1/4}$ is of order one.

CYCLING POLYNYA STATES IN THE ANTARCTIC

Douglas G. Martinson

1. Introduction

A remarkable feature of the winter sea ice distribution in the Weddell Sea is the presence of an irregularly occurring polynya. This is a rather unexpected presence as it appears during periods of winter cooling in the center of an otherwise ice covered region. It is important to understand this feature as it might also be expected to have a moderating effect on the local heat flux which substantially increases in areas of open water.

The polynya is a large ($\sim 10^6 \text{ km}^2$) open water feature which contains as much as 15% ice and occurs quasi-periodically in the winters near the southeastern limits of the Weddell Sea (approximately 65°S , 0°E). On a gross scale the polynya appears to be present for three years, then missing for three. This suggested cycle is based on an extremely short satellite record relative to the cycling time and on scattered observational data. This paper will address three major questions pertaining to the polynya: 1) Why does it occur? 2) Why is its occurrence quasiperiodic (as opposed to full time) and 3) why does it always seem to occur in the vicinity of approximately 65°S , 0°E ?

2. The Theory

Most ideas concerning the origin of the polynya attribute its existence to the upwelling of warm deep water as it was assumed to form at the center of a cyclonic gyre system where upwelling would be maximum. This appears not to be the case, however, as shown by the wind driven circulation scheme of Gordon, Martinson and Taylor (in press) which shows the gyre center

to be almost 10° north of the usual polynya position (Fig. 1).

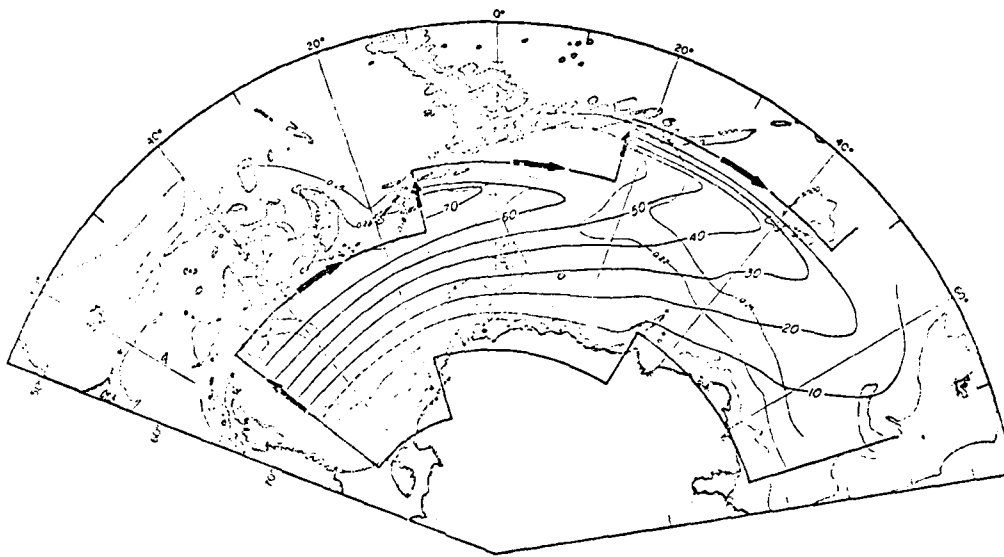


Fig. 1. Streamlines representing cyclonic flow in Weddell-Enderby basins. Maximum upwelling occurs in gyre center east of 30°E . Maud Rise is seamount located at 65°S , 0°W (Gordon, Martinson and Taylor, in press).

Corresponding Ekman upwelling values clearly show the maximum upwelling to occur to the north and east of the polynya area (Gordon, 1979).

In light of the above results an alternative theory has been put forth by Gordon (oral communication). The theory suggests that a preconditioning is required which would raise the pycnocline and hence bring the deep water close to the surface. Here it can respond to upper layer buoyancy changes due to atmospheric cooling or salt ejection during ice formation. When the upper layers become as dense as the deep water, overturning will occur and the warm, salty deep water will mix with the cold, fresh surface layer. The large

volume of deep water will dominate the overturned temperature and salinity characteristics resulting in warm, salty water which will then melt the ice and form the polynya. A fresh water input at the surface (see section 4) would then slowly stabilize the system again and the process repeats itself.

A likely candidate for the preconditioning is Maud Rise, a seamount located at 65°S , 0°E (Fig. 1) over which a portion of the polynya always seems to occur. Maud Rise comes to within 600 m of the surface and geologically is rich in diatomaceous ooze (vs. clay ooze in the surrounding sediments), possibly suggesting the polynya has been located in this same position over geological time.

3. The Model

For the purpose of modelling, the system has been simplified to two levels in the vertical with nonhorizontal variations. The vicinity of the polynya appears to be an exceptionally good location for two level approximations as can be seen by the Sigma-t vs. depth profiles in the belt from 65° - 70°S and 0° - 40°W (Fig. 2). The approximation has several other advantages. By using two distinct levels with averaged characteristics the effects of a steady state upwelling will be incorporated into the model (through either the thickness chosen for the upper level or the temperature of the upper level) and the dynamics and cause of the preconditioning can be ignored as its effects will also be incorporated into the levels.

We chose an upper level depth of 200 m for several reasons. First, 200 m is a good approximation to the observations - at least in summertime. Second, in a continuously stratified model of cooling near the polynya region, Killworth (1979) showed that overturning almost invariably took place after mixing had reached 195-200 m. Of course, in times of summer heating, a thin surface mixed layer would form, with a depth determined presumably by Monin-Obukhov

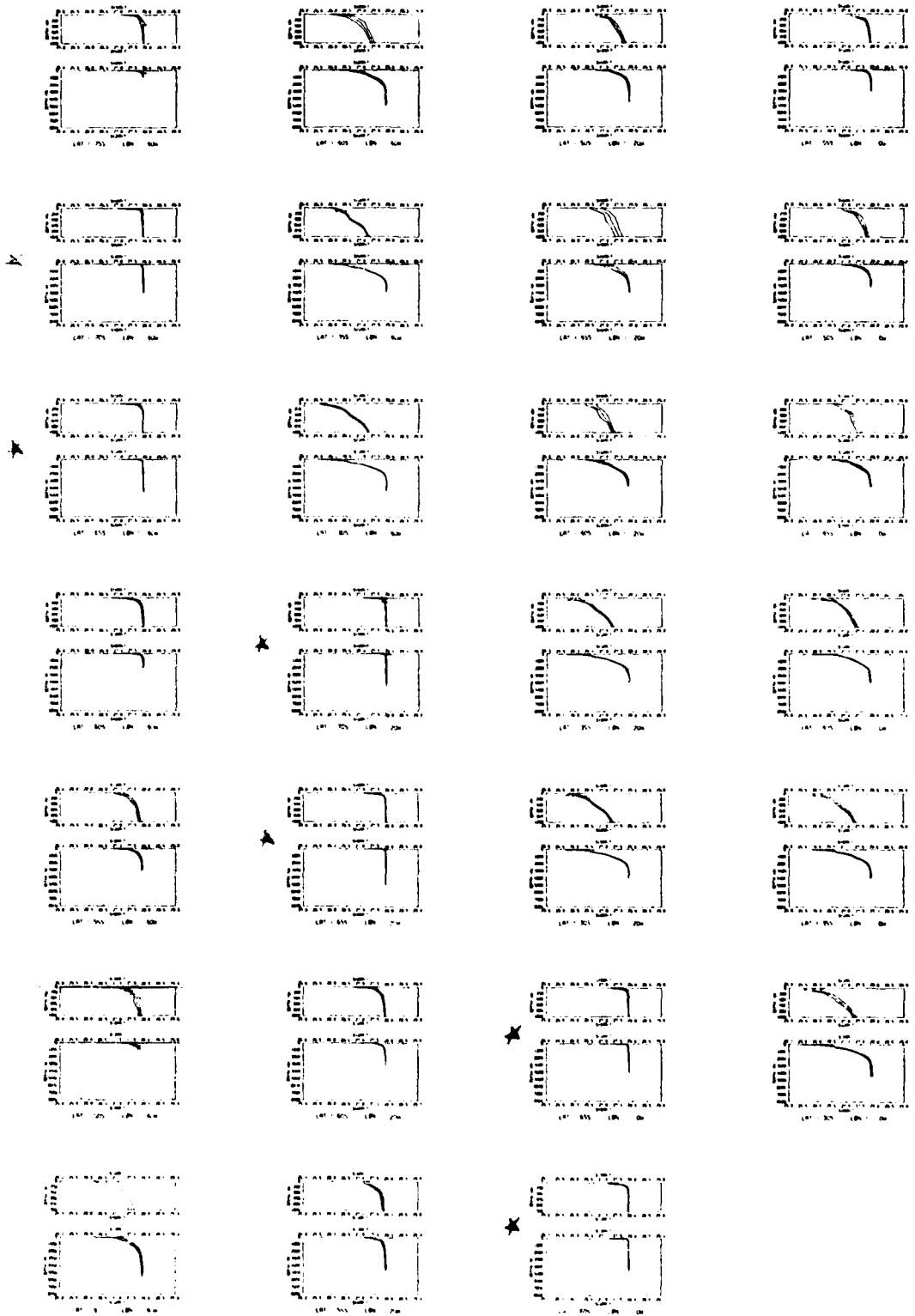


Fig. 2. Sigma-t vs. depth profiles at 5° latitudes and 20° longitudes from 75°-30°S and 0°-40°W. Profiles with asterisks are where a two level approximation is best.

scalings. The model ignores such a layer; however, the conservation of heat and salt within the system ensures that the main physical features of such a continuously stratified system are reproduced by the model, with at worst a minor variation in time scales. If successful results can be obtained using this system, the importance of a preconditioning can then be examined by evaluating the system using different thicknesses of the upper level.

The actual model considers four states (Fig. 3); a discussion of the physical processes involved will be given in Section 4.

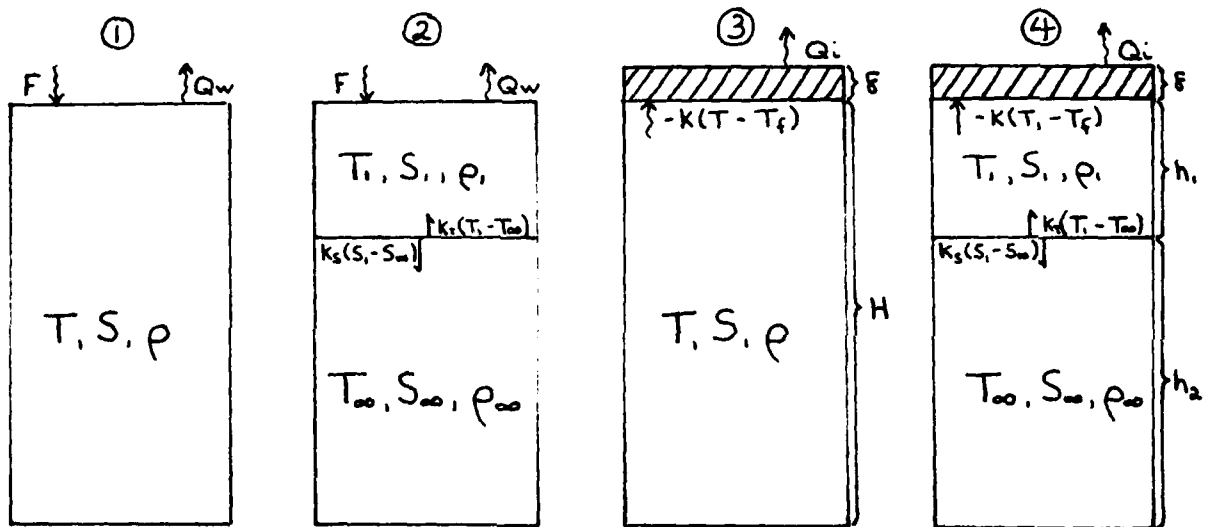


Fig. 3 Schematic of the four states used in the model. See text for discussion.

State 1 is an ice free overturned state which will gain or lose heat (Q_w) and will gain fresh water (F). State 2 is also ice free and has Q_w and F fluxes as well as some (possibly) double diffusive exchange between the two levels (K_T is the heat and K_S the salt transfer coefficients). The lower level is an infinite reservoir of temperature T_∞ and salinity S_∞ . State 3 is the ice covered overturned state which gains or loses a smaller (due to insolation by the ice cover) heat flux (Q_1) and has a turbulent flux of heat (coefficient K) melting the ice from below. State 4 is the ice covered equivalent

of state 2.

The corresponding governing equations are as follows:

State 1

$$1a \quad H \frac{\partial T}{\partial t} = \frac{Q_w}{\rho C_p}$$

$$1b \quad H \frac{\partial S}{\partial t} = -F$$

$$1c \quad \delta = 0$$

State 2

$$2a \quad h_1 \frac{\partial T_1}{\partial t} = \frac{Q_w - K_T(T_1 - T_\infty)}{\rho C_p}$$

$$2b \quad h_1 \frac{\partial S_1}{\partial t} = -K_S(S_1 - S_\infty) - F$$

$$2c \quad \delta = 0$$

State 3

$$3a \quad H \frac{\partial T}{\partial t} = \frac{-K(T - T_f)}{\rho C_p}$$

$$3b \quad H \frac{\partial S}{\partial t} = \sigma \frac{\partial \delta}{\partial t}$$

$$3c \quad \frac{\partial \delta}{\partial t} = \frac{-Q_i - K(T - T_f)}{\rho_i L}$$

State 4

$$4a \quad h_1 \frac{\partial T_1}{\partial t} = \frac{-k(T_1 - T_f) - k_r(T_1 - T_\infty)}{\rho C_p}$$

$$4b \quad h_1 \frac{\partial S_1}{\partial t} = \sigma \frac{\partial \delta}{\partial t} - k_s(S_1 - S_\infty)$$

$$4c \quad \frac{\partial \delta}{\partial t} = \frac{-Q_i - k(T_1 - T_f)}{\rho_i L}$$

where ρ = density of water; C_p = specific heat of water;

ρ_i = density of ice; L = latent heat of ice;

σ = (35 o/oo - salinity of sea ice) and T_f = freezing point of seawater.

The equation of state (with ρ_0 a reference density) is:

$$\frac{\rho}{\rho_0} = -\alpha T + \beta S$$

where α and β are constants defined at 200 m depth.

The nonlinearities between states are circumvented by physically employing the governing set of equations determined by the following transitions:

State 1

$$\textcircled{1} \rightarrow \textcircled{2} \quad \text{if} \quad -\alpha \frac{\partial T}{\partial t} + \beta \frac{\partial S}{\partial t} < 0$$

initial conditions: $T_1 = T$; $S_1 = S$

$$\textcircled{1} \rightarrow \textcircled{3} \quad \text{if} \quad T = T_f$$

i.c.: $\delta = 0$

State 2

$$\textcircled{2} \rightarrow \textcircled{1} \quad \text{if} \quad -\alpha(T_1 - T_\infty) = \beta(S_\infty - S_1)$$

i.c.: $T = \frac{1}{H}(h_1 T_1 + h_2 T_\infty)$

$S = \frac{1}{H}(h_1 S_1 + h_2 S_\infty)$

$$\textcircled{2} \rightarrow \textcircled{4} \quad \text{if} \quad T_1 = T_f$$

i.c.: $\delta = 0$

State 3:

$$\textcircled{3} \rightarrow \textcircled{1} \quad \text{if } \xi = 0$$

$$\text{i.c. } T = T; S = S$$

$$\textcircled{3} \rightarrow \textcircled{4} \quad \text{if } -\alpha \frac{\partial T}{\partial t} + \beta \frac{\partial S}{\partial t} < 0$$

$$\text{i.c. } T_1 = T; S_1 = S$$

State 4

$$\textcircled{4} \rightarrow \textcircled{3} \quad \text{if } -\alpha (T_1 - T_\infty) = \beta (S_\infty - S_1)$$

$$\text{i.c. } T = \frac{1}{H} \cdot (h_1 T_1 + h_2 T_\infty);$$

$$S = \frac{1}{H} \cdot (h_1 S_1 + h_2 S_\infty)$$

$$\textcircled{4} \rightarrow \textcircled{2} \quad \text{if } \xi = 0$$

$$\text{i.c. } T_1 = T_1;$$

$$S_1 = S_1$$

Figure 4 summarizes these possible transitions.

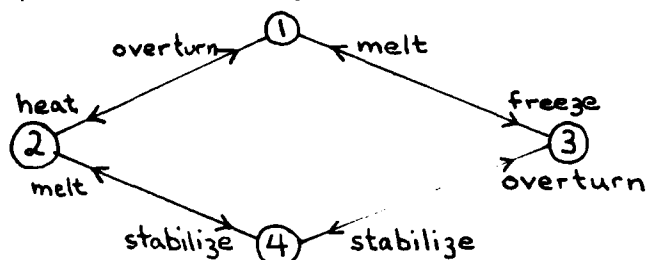


Fig. 4. Schematic representation of the possible transitions which can occur in the model.

Solutions

$$1a. T = \frac{1}{H \rho c_p} \int Q_w dt + T_0$$

$$1b. S = -\frac{F}{H} \Delta t + S_0$$

$$2a. T_1 = \frac{1}{h_1 \rho c_p} e^{-k_T/h_1 \rho c_p} \int Q_w e^{+k_T/h_1 \rho c_p} dt + (T_{10} - T_\infty) e^{-k_T \Delta t/h_1 \rho c_p} + T_\infty$$

$$2b. S_i = \left(S_{i0} - S_{\infty} + \frac{F}{k_s} \right) e^{-k_s \Delta t / h_i} + S_{\infty} - \frac{F}{k_s}$$

$$3a. T = (T_0 - T_f) e^{-k \Delta t / H \rho c_p} + T_f$$

$$3b. S = \frac{\sigma}{H} (\delta - \delta_0) + S_0$$

$$3c. \delta = -\frac{1}{\rho_i L} \int Q_i dt + \frac{H \rho c_p}{\rho_i L} (T_0 - T_f) (e^{-k \Delta t / H \rho c_p} - 1) + \delta_0$$

$$4a. T_i = \frac{k T_f + k_r T_{\infty}}{k + k_r} + \left(T_0 - \frac{k T_f + k_r T_{\infty}}{k + k_r} \right) e^{-(k + k_r) \Delta t / h_i \rho c_p}$$

$$4b. S_i = -\frac{\sigma}{h_i \rho_i L} e^{-k_s t / h_i} \int Q_i e^{k_s t / h_i} dt + S_{\infty} (1 - e^{-k_s \Delta t / h_i}) - \frac{\sigma k}{h_i \rho_i L} \left[\frac{h_i k_r (T_{\infty} - T_f)}{k_s (k + k_r)} (1 - e^{-k_s \Delta t / h_i}) + \frac{h_i (T_{i0} - (k T_f + k_r T_{\infty}) / (k + k_r))}{k_s - (k + k_r) / \rho_i c_p} (e^{-(k + k_r) \Delta t / h_i \rho c_p} - e^{-k_s \Delta t / h_i}) \right] + S_{i0} e^{-k_s \Delta t / h_i}$$

$$4c. \delta = -\frac{1}{\rho_i L} \int Q_i dt + \frac{k k_r (T_{\infty} + T_f)}{\rho_i L (k + k_r)} \Delta t + \frac{k h_i \rho c_p}{\rho_i L (k + k_r)} \left(T_{i0} - \frac{k T_f + k_r T_{\infty}}{k + k_r} \right) (e^{-(k + k_r) \Delta t / h_i \rho c_p} - 1) + \delta_0$$

4. Parameter Values

The values of Q_w and Q_i are obtained from Gordon (1979) with modifications to the summer insolated values. These modifications arise from the fact that

Gordon's Q_i summer values are for dry, white reflecting ice. In nature, as Q changes its sign to positive the upper surface of the ice begins to melt, making a thin surface layer of water or wet ice. The result is a rapid decrease in the effect of the albedo and hence the modified values for summer are the same as the summer Q_w values. The actual value is probably some compromise between the two extremes. This modification of Q is necessary, to prevent year round ice cover in the event of no overturning as the ice generated during the winter could not melt during summer using the white reflecting ice values (Gordon, 1979, GFD, Lecture 2).

The value of K (turbulent heat flux transfer coefficient into the ice from the water) is taken from Killworth (1979) in which he derives a value of 2.59×10^3 cal/cm²°C day. Values of T_∞ and S_∞ are taken from observations and are 0°C and 34.66 o/oo respectively. The initial values of T_1 and S_1 (the computations begins in state 4 on first day of May) are also from observations for May first and equal -1.9° and 34.40 o/oo respectively. The ice is just beginning to grow so $\xi = 0$. Values for ρ_i , L , σ and T_f are taken from Killworth (1979) and are .9 g/cm³, 60 cal/g, 30 o/oo and -1.9°C respectively.

The values of K_T and K_S are more difficult to obtain and of the two methods used to derive their values here, agreement is only within an order of magnitude. The first method from which K_T can be derived represents an upper limit. Assuming no overturning, one can set K_T at the value necessary to balance the yearly loss of heat from the upper level. When solving for K_T in this manner a value of 6 cal/cm² °C day is obtained. Alternatively, K_T can be solved for by constructing a seasonal ice cycle. For the ice to disappear by the beginning of summer, as is usually observed, an

overturning must occur at the end of spring. Working backwards from here and using an iterative approach a seasonal cycle can be constructed (see section 5) in which K_T is considered the only unknown. In this manner, for various values of F , the value of K_T is $O(1)$ in these units. The actual value of K_T used for most of the results presented here is $6 \text{ cal/cm}^2 \text{ }^\circ\text{C day}$. Sensitivity of the equations to these parameters is discussed in a later section. K_S is in all cases taken to be 15% of K_T as suggested by Turner (oral communication).

The input of fresh water into the system is essential to the model. As can be easily seen, with no fresh water entering the overturned state the high salinity would persist and each year following the summer heating cycle, overturning would occur as soon as the temperature of the upper level cooled to T_∞ . The fresh water flux required to stabilize the system can enter it in two ways. Precipitation is an obvious source. Estimates of precipitation over evaporation for this area are of the order of 50 cm/yr.

Another possible source of F arises from the fact that in years when a polynya occurs there is essentially a 10^3 Km^3 volume of ice not formed which normally acts as a fresh water sink. If one assumes that the ice (or some fraction of it) which frequently forms in the polynya area melts elsewhere than in polynya years, no ice forming would represent a fresh water input. An upper limit for this case (assuming all the ice melts elsewhere) is approximately 100 cm/year for polynya years (and 0 for the nonpolynya years).

In this model F is converted to a fresh water flux ($50 \text{ cm/yr} \approx 4.9 \text{ o/oo cm/day}$) and is input to the system only during periods of open water.

5. How Important are the Parameter Values Used?

The sensitivity of the results to the values of the parameters can best be evaluated by nondimensionalizing the governing equations. Scales may be

defined as: $t^* = tK/H\rho c_p$; $\phi_1 = K/K_T$; $\phi_2 = (K + K_T)/K_T$
 $= 1 + \phi_1$; $\epsilon = H/h$; $T^* = T/T_f$; $S^* = S/S_\infty$;
 $P^* = F/K_S S_\infty$; $\delta^* = \delta/H$; $Q^* = Q/T_f K$;
 $\gamma = K_S \rho c_p / K$; $\nu = T_f \rho c_p / \rho_i L$ and $\eta = \sigma/S_\infty$.

The resulting equations take the form:

1a. $\frac{\partial T^*}{\partial t^*} = Q^*$

1b. $\frac{\partial S^*}{\partial t^*} = \gamma P^*$

1c. $\delta^* = 0$

2a. $\frac{\partial T_i^*}{\partial t^*} = \epsilon Q^* - \epsilon \phi_1 (T_i^* - T_\infty^*)$

2b. $\frac{\partial S_i^*}{\partial t^*} = -\epsilon \gamma (S_i^* + P^* - 1)$

2c. $\delta^* = 0$

3a. $\frac{\partial T^*}{\partial t^*} = 1 - T^*$

$$3b. \frac{\partial S^*}{\partial t^*} = -\eta v(Q^* + T^* - 1)$$

$$3c. \frac{\partial \delta^*}{\partial t^*} = -v(Q^* + T^* - 1)$$

$$4a. \frac{\partial T_i^*}{\partial t^*} = -\epsilon \phi_2 T_i^* + \epsilon(1 + \phi_1 T_\infty^*)$$

$$4b. \frac{\partial S_i^*}{\partial t^*} = -\epsilon \eta v(Q^* + T_i^* - 1) - \epsilon \gamma (S_i^* - 1)$$

$$4c. \frac{\partial \delta^*}{\partial t^*} = -v(Q^* + T_i^* - 1)$$

With analytic solutions:

$$1a. T^* = \int Q^* dt^* + T_0^*$$

$$1b. S^* = \gamma P^* \Delta t^* + S_0^*$$

$$2a. T_i^* = \epsilon e^{-\epsilon \phi_1 t^*} \int Q^* e^{\epsilon \phi_1 t^*} dt^* + (T_{i0}^* - T_\infty^*) e^{-\epsilon \phi_1 \Delta t^*} + T_\infty^*$$

$$2b. S_i^* = (S_{i0}^* + P^* - 1) e^{-\epsilon \gamma \Delta t^*} - P^* + 1$$

$$3a. T^* = (T_0^* - 1) e^{-\Delta t^*} + 1$$

$$3b. S^*(T^*) = -\eta v \left[\int Q^* dt^* - (T_0^* - 1) e^{-\Delta t^*} + T_0^* - 1 \right] + S_0^*$$

$$S^*(\delta^*) = \eta (\delta^* - \delta_0^*) + S_0^*$$

$$3c. \delta^* = -v \left[\int Q^* dt^* - (T_0^* - 1) e^{-\Delta t^*} + T_0^* - 1 \right] + \delta_0^*$$

$$4a. T_1^* = \left(T_{10}^* + \frac{T_{\infty}^* - 1}{\phi_2} - T_{\infty}^* \right) e^{-\epsilon \phi_2 \Delta t^*} + T_{\infty}^* - \frac{T_{\infty}^* - 1}{\phi_2}$$

$$4b. S_1^* = -\epsilon \eta e^{-\epsilon \gamma t^*} \left\{ \int Q^* e^{\epsilon \gamma t^*} dt^* - \frac{\phi_1 \eta v (T_{\infty}^* - 1)}{\gamma \phi_2} + 1 \right. \\ \left. + \left[-\frac{\eta v T_{10}^*}{(\phi_2 - \gamma)} + \frac{\eta v (T_{\infty}^* \phi_1 + 1)}{\phi_2 (\phi_2 - \gamma)} + \frac{\phi_1 \eta v (T_{\infty}^* - 1)}{\gamma \phi_2} + S_{10}^* - 1 \right] \right. \\ \left. \cdot e^{-\epsilon \gamma \Delta t^*} + \frac{\eta v}{(\phi_2 - \gamma)} \left(T_{10}^* + \frac{T_{\infty}^* - 1}{\phi_2} - T_{\infty}^* \right) e^{-\epsilon \phi_2 \Delta t^*} \right.$$

$$4c. \delta^* = -v \left[\int Q^* dt^* - \left(\frac{T_{10}^* - T_{\infty}^*}{\epsilon \phi_2} + \frac{T_{\infty}^* - 1}{\epsilon \phi_1} \right) e^{-\epsilon \phi_2 \Delta t^*} \right. \\ \left. + \left(T_{\infty}^* - 1 - \frac{T_{\infty}^* - 1}{\phi_2} \right) \Delta t^* + \frac{T_{10}^* - T_{\infty}^*}{\epsilon \phi_2} + \frac{T_{\infty}^* - 1}{\epsilon \phi_1} \right] + \delta_0^*$$

These solutions can now be simplified by expanding the exponentials in ϕ_1 , ϕ_2 , and γ into Taylor series and neglecting the higher order terms. This is valid for the calculated range of ϕ_1 and γ .

The resulting simplifications (nondimensional and dimensional) are then as follows for states 2 and 4 (states 1 and 3 are unchanged):

$$2a. T_1^* = T_{10}^* - [\phi_1 (T_{10}^* - T_{\infty}^*) - Q^*] \epsilon \Delta t^*$$

or $T_1 = T_{10} - [k_T (T_{10} - T_{\infty}) - Q] \Delta t / h_i \rho c_p$

$$2b. S_1^* = S_{10}^* - [\gamma (S_{10}^* - 1) + F^*] \epsilon \Delta t^*$$

or
$$S_1 = S_{10} - [K_s(S_{10} - S_\infty) + F]\Delta t/h,$$

4a.
$$T_1^* = (T_{10}^* - 1)(1 - \epsilon\phi_1\Delta t^*)e^{-\epsilon\Delta t^*} + 1$$

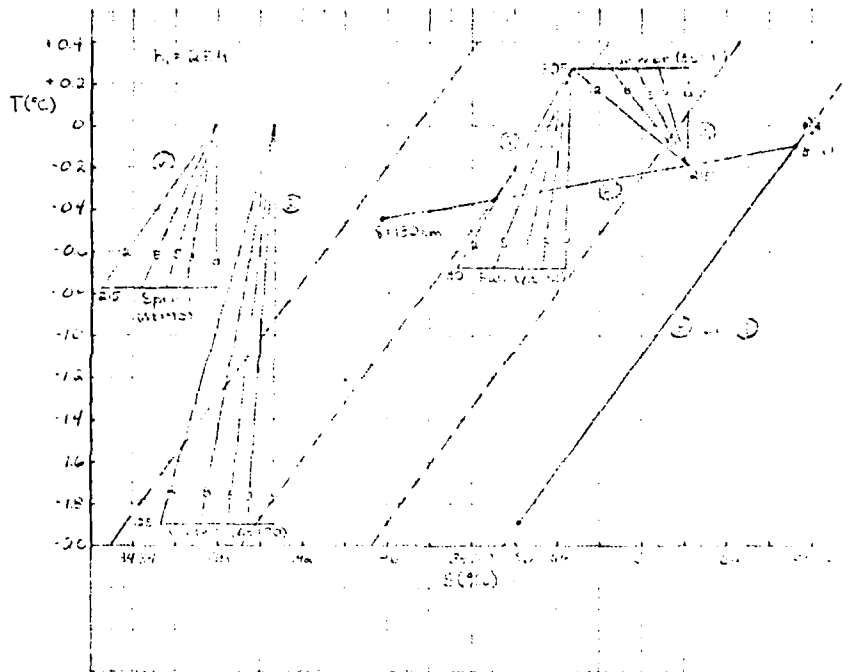
or
$$T_1 = (T_{10} - T_f)(1 - K_T \frac{\Delta t}{h_1\rho c_p})e^{-K\Delta t/h_1\rho c_p} + T_f$$

4b.
$$S_1^* = -\eta\nu[(T_{10}^* - 1)(1 - \epsilon\phi_1\Delta t^*)e^{-\epsilon\Delta t^*} + T_{10}^* - 1 + T_\infty^*\phi_1] \\ + S_{10}^* - [\eta\nu Q^* + \eta\nu\phi_1(T_\infty - 1) + \gamma\eta\nu T_\infty^*\phi_1 \\ - \eta\nu\gamma(T_{10}^* - 1) + \gamma S_{10}^* - \gamma]e\Delta t^*$$

or
$$S_1 = \frac{\sigma\rho c_p}{\rho_i L} \left[(T_{10} - T_f)(1 - K_T \frac{\Delta t}{h_1\rho c_p})e^{-K\Delta t/h_1\rho c_p} + T_{10} - T_f \right. \\ \left. + T_\infty \frac{K_T}{K} \right] - \left[\frac{Q}{\rho_i L} + K_T(T_\infty - T_f) + \frac{K_s K_T \rho c_p}{K \rho_i L} (T_\infty - T_{10} + T_f) \right. \\ \left. + \frac{K_s}{\sigma} (S_{10} - S_\infty) \right] \frac{\sigma \Delta t}{K h_1 \rho c_p} + S_{10}$$

This reduces state 2 solutions to simple linear functions and state 4 solutions reduce to exponentials with time scales of the order of 10 days in K. Comparing this to K_T time scales of the order of 10,000 days in state 4 and two orders of magnitude less than the Q_w term in state 2 suggests that the effects of K_T are essentially negligible. The effects of the diffusive transfer of salt (K_s), however, is not negligible as $\frac{K_s}{F} (S_{10} - S_\infty) = 0(1/5)$.

The effects of the other parameters can best be seen by examining their effects on the slopes and time scales for the various states on a T-S diagram which evolves with time (Fig. 5).



THIS PAGE IS BEST QUALITY FRAGMENTABLE FROM COPY FURNISHED TO BDC

Fig. 5. T-S diagram showing various slopes as a function of season (Q), F (value written on each line), state (circled number) and for state 4, ice thickness (Y). Large cross is value of deep water, Sov is value at which overturning occurs in state 4, dashed lines represent isopycnals.

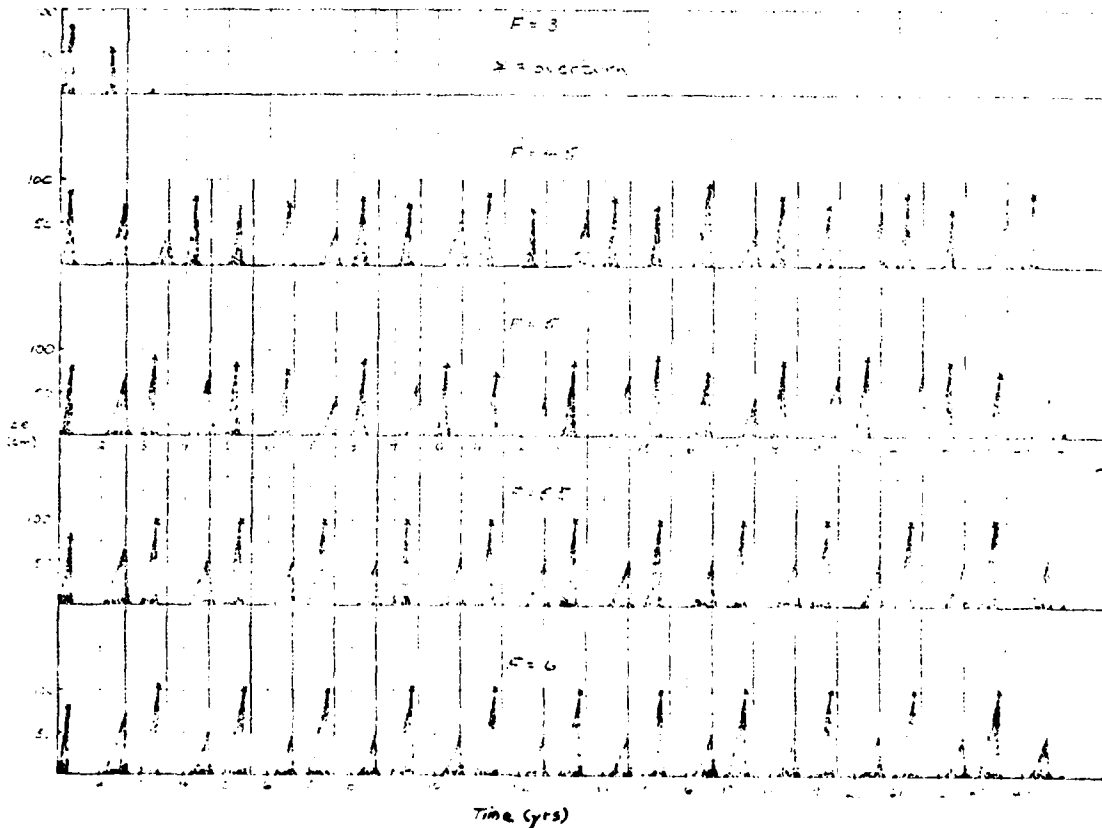


Fig. 6. Model results as a function of F, plotted as ice thickness vs. year. "Regular" nonpolynya season would have ice begin to form near the first of the model year and melt by the vertical lines drawn.

The slopes and time scales are given as:

State 2

$$5. \frac{\partial T}{\partial S} = - \frac{Q}{F \rho c_p} = - \frac{Q}{F \rho} \quad (\rho = c_p = 1)$$

$$6. \Delta t = \frac{h_i \rho c_p}{Q} \Delta T = - \frac{h_i}{F} \Delta S$$

State 4

$$7. \frac{\partial T}{\partial S} (\text{ice melt}) = \frac{\rho_i L}{\sigma \rho c_p} = 1.8$$

if $K(T_1 - T_f) \gg Q$, not true when $T_1 \approx T_f$ during freezing.

$$8. \Delta t (\text{ice melt}) = - \frac{\rho_i L}{K(T_1 - T_f)} \Delta S$$

$$9. \Delta t (\text{overturn}) = \frac{h_i \rho_i L}{\sigma Q_i} \Delta S$$

where $\Delta S = S_{ov} - S_1$ ($S_{ov} = 34.522$ o/oo).

For state 2, however, the position of the upper level (in T-S space) is a function of the slope (F, Q) and the time scale for the given slope (which is a function of h_i , Q and F). The slopes for state 2 shown in Fig. 5 are shown as a function of the value of F and the lengths assume a full season time scale. The salinity at which state 4 is therefore entered will depend directly on the combinations and time scales spent on the different slopes in state 2. Once in state 4 ($T_f = 1.9^\circ\text{C}$), $dT/dS = 0$, the length of time until overturning will depend on the distance from S_{ov} (ΔS_{ov}) as well as the time of year freezing began (which sets the value of Q_i) and the thickness

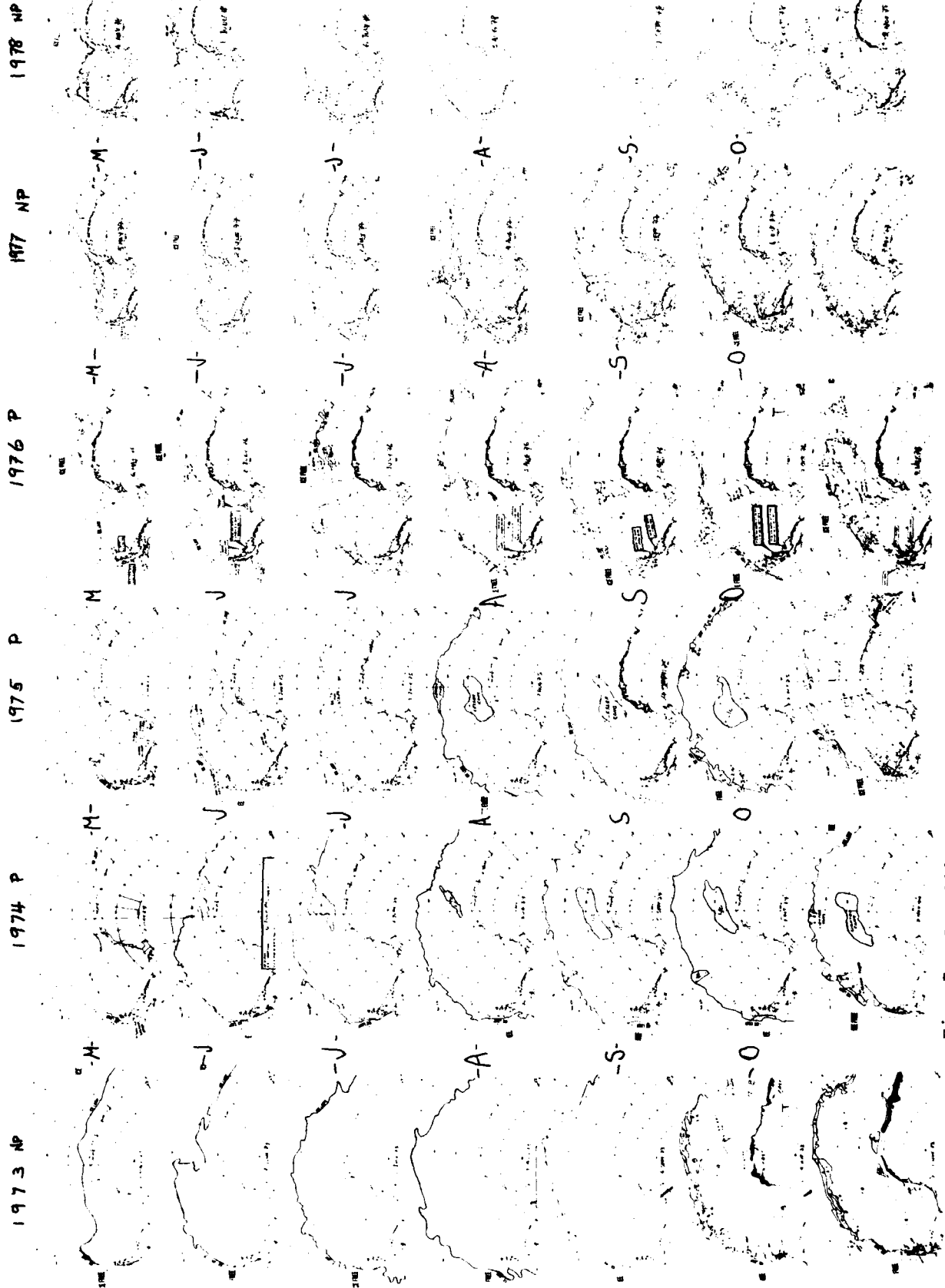


Fig. 7. Satellite record of ice distribution for May-November (= day 1 to the vertical lines of Figure 6 in the model) from 1973-1978.

THIS PAGE IS BEST QUALITY PRACTICABLE
FROM COPY FURNISHED TO DDC

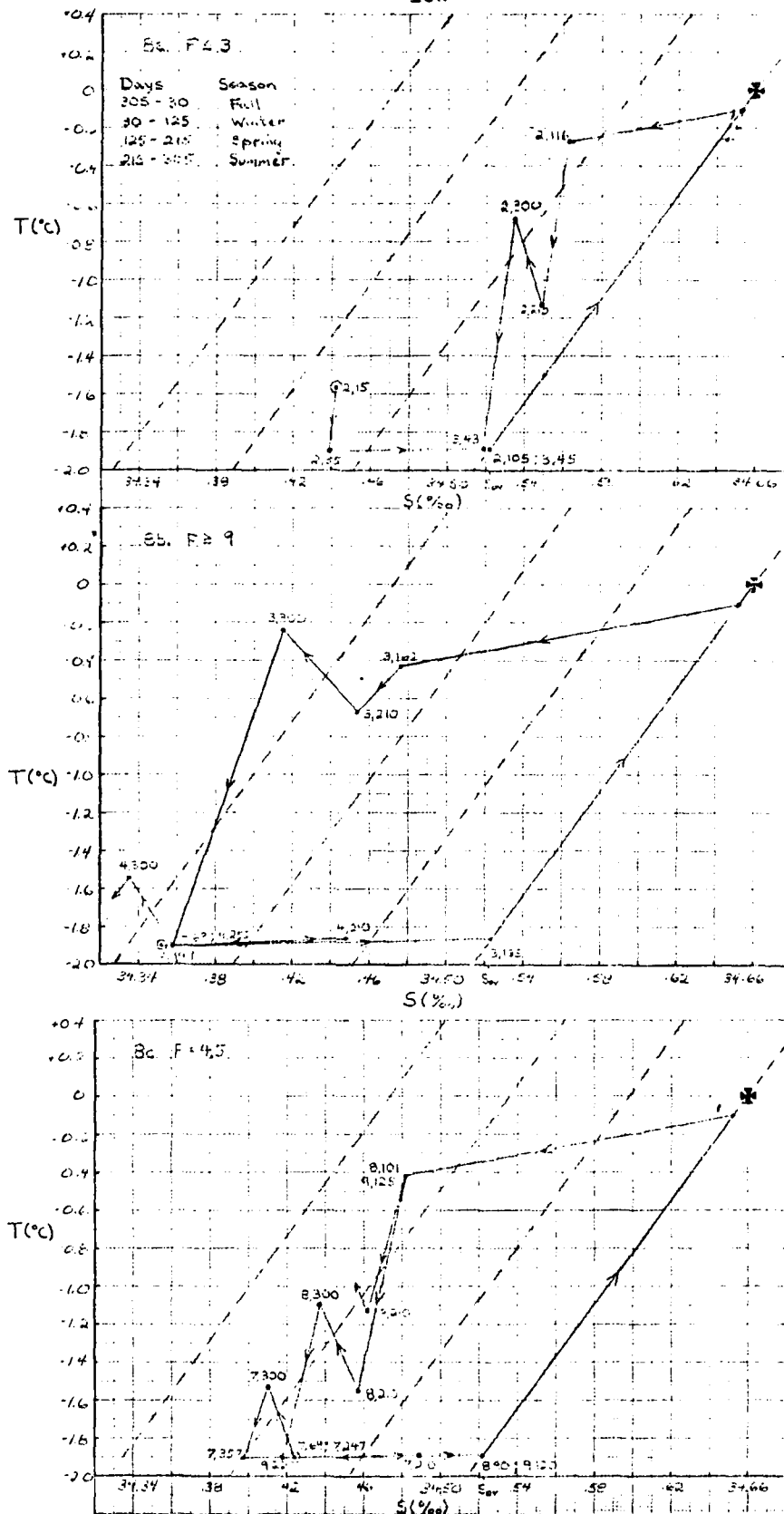
assumed for the upper level (h_1). If overturning occurs the slope in T-S space during melting is constant, but the distance down the slope depends on the amount of ice melted. If overturning does not occur, the melting ice will simply return to the position on the T_f line at which state 4 began and the effects of summer heating and subsequent fall cooling back to the freezing point will result in a net decrease in salinity. The new freezing period will therefore have to produce more ice before overturning and the ice melt slope will then increase relative to the prior overturned year.

From this it can be seen that the resulting T-S position after each change in Q is very sensitive to the values of F, Q and h. A slight change in the length of time on a slope directly affects the positions of the following slopes which may cause overturning to occur earlier or not at all.

6. Model Results

The model results for various values of F are given in Fig. 6 as plots of ice vs. time with the first of each year corresponding to the first of May. Figure 7 shows ice conditions (from satellite images) for the months of May - November from 1973 - 1978. It can be seen that for values of $F \leq 3$ the fresh water input is too low to overcome the high salinity resulting from overturning.

This is easiest seen in Figure 8a which shows that after the ice melts following year 2 the slopes in state 2 are not shallow enough (due to low F) to move to a position of low salinity; hence, when ice forms in year three only a few centimeters are necessary before overturning. The ice melt slope is then barely traveled and any cooling now results in almost immediate overturning. The slopes in state 2 are too steep for the system to ever recover and hence ice never forms again.



THIS PAGE IS BEST QUALITY FRAGMENTABLE FROM COPY FURNISHED TO DDC

Fig. 8. T-S diagram which evolves in time. Numbers represent year followed by the day, cross is position of deep water, Sov is salinity for overturning in state 4, circled position is starting point. Plots are as functions of F: a) F = 3, b) F = 9 and c) F = 4.5.

F values of 5.5 to 9 result in overturning every other year with the only differences in the results being the amount of ice built up and the seasonal extent of the ice cover. For $F = 5.5$ overturning occurs in August at which time a polynya would form whereas for $F = 6$ the overturning occurs almost a month later.

For values of $F \geq 9$ the system receives too much fresh water input and the upper level quickly becomes too stable for overturning (Fig. 8b). In this case the slopes are so shallow that the position on the T-S diagram is toward low salinities very rapidly and eventually not enough ice can form in the cooling season to overcome the fresh water input.

Values of 4.5 - 5 for F (see Fig. 8c) seem to result in an irregular cycling where polynas form at various times of the year and some years not at all. Comparing the results of these two cases with the observed seasonal ice distribution (Fig. 7) reveals many striking similarities. The previously considered "regular cycle" is now observed as being irregular. Overturning is seen to occur at different times each year and as late as August (1979), October (1973) and November (1978). This is reproduced in the model results as is an irregular cycle in the time when the ice begins to form (compare ice growth for August 1973 with August 1977). Another result from the model is that years in which a polynya forms are often followed by years of late ice formation and thin ice thickness. This is seen in the data by examining the 1977 season, which follows the full polynya of 1976. Ice growth does not cover the region of the polynya until as late as July with an areal extent which is much smaller than years of full polynyas like 1974 and 1975. Whether the ice was as thick as 1977, however, is unknown. The model also shows a high number of years in which overturning occurs at some time before the end

of the normal ice season. Previous examinations of the data had only considered such years as 1974-76 as overturning polynya years and the other years as non overturning. In light of the model results, however, it can be seen that in the last six years (including 1979) overturning has occurred before summer in five of them (vs. four of six years in the model results).

Finally, because the data show that overturning occurs (e.g. October 1973), it lends support to the model's use of a large discontinuity in the equation of state which preconditions overturning as opposed to a continual thickening of an upper layer with no overturning.

7. Sensitivity to Varying Parameters

The model has been tested for the effects of natural variations in the parameters of Q and F. This has been done in a variety of ways which includes the following:

1) Shocking the system. The values of Q were increased and decreased by 10% on the twelfth year of the run for the entire twelfth year. The values of Q were then increased, decreased and alternatively increased, decreased every fourth year of the run by 10%. These tests were then done to F and finally to both Q and F.

2) Stochastic variation. The values of Q were changed daily stochastically by as much as $\pm 20\%$ for the entire 25-year run. This was then done to F and finally to both Q and F together.

3) Stochastic variation and shocking the system. The final testing was various combinations of the previous tests concluding with a run which included all the perturbations on both Q and F together.

The purpose of perturbing the system was to subject the model to various perturbations which might be expected in nature (a suggestion of a four-year

cycle can be observed in the SANAE meteorological data from the Weddell Sea area). These results can then be compared to the basic results presented in Fig. 6 to see the effects which these variations may induce. In all cases ($F=4.5, 5$ and 5.5) the perturbations only effects were to change the timing of the overturning and beginning of the ice growth by a few days over a period of six years. This would eventually result in the missing of a polynya, addition of a polynya year, etc. after a 25-year run in some cases. On a gross scale, however, the model results were unchanged and a natural variation of the meteorological parameters would therefore not be expected to significantly change the model results from the steady case.

8. Effects of Preconditioning

The significance of preconditioning can be checked by evaluating the effects of the thickness of the upper level (h_1) on the model results (the preconditioning may actually be the creation of the large discontinuity in the equation of state in which case an examination of the region containing the discontinuity should be substituted for an evaluation of a varying h_1). By examining equations 6 and 9 it is seen that h_1 affects only the time scales of the system and not the slopes. This has an unexpected effect, however, on the entire system. Figure 9a shows an evolving T-S diagram which includes a steady seasonal cycle for $h_1 = 200$ m in which ice forms and melts in a roughly nonpolynya area cycle. Plotted with this are runs with the same parameters values as the seasonal plot with the exception of h_1 which has been both increased and decreased. Figure 9b shows the corresponding ice vs time plot.

For both variations it can be seen that the salinity of the upper layer is such that a full overturning is no longer possible and a steady seasonal cycle is maintained. These results can be explained by examining the effects of h_1 on the

THIS PAGE IS BEST QUALITY PRACTICABLE
FROM COPY FURNISHED TO DDC

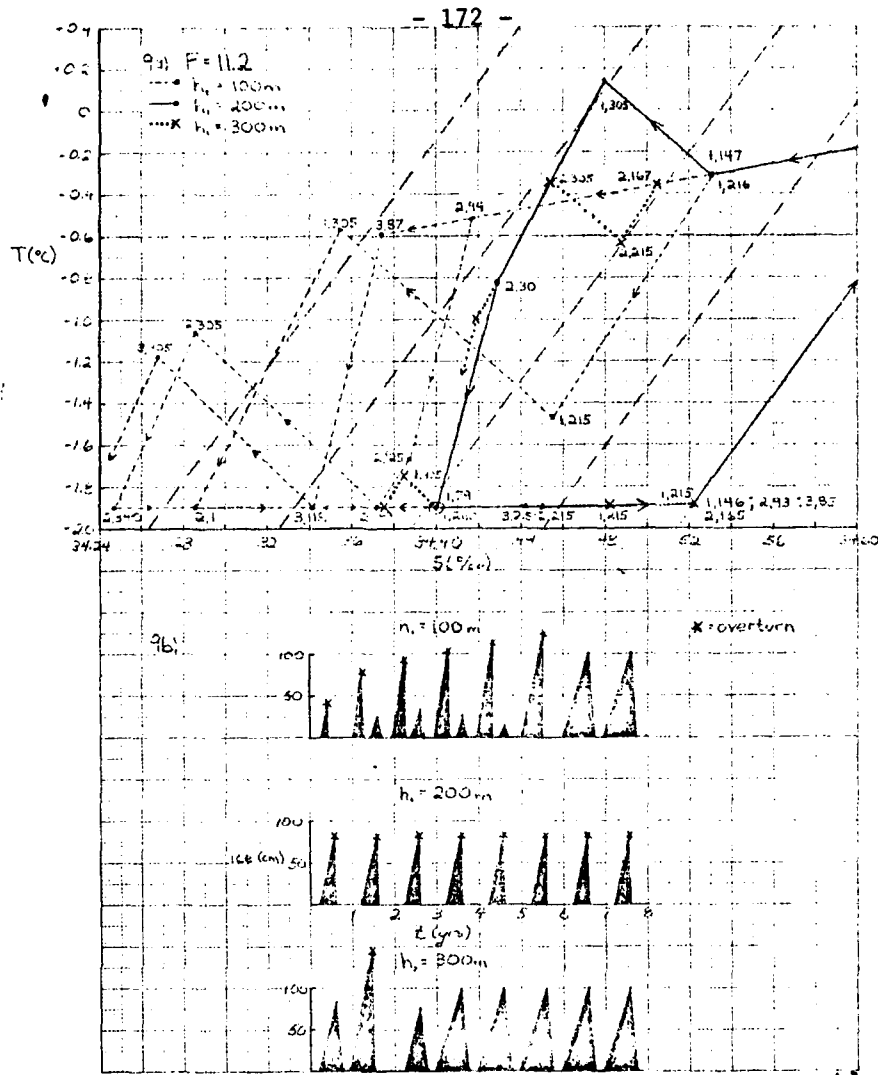


Fig. 9. a) T-S diagram as in Figure 8 only for varying values of the upper level thickness h_1 , all other parameters equal. Position of deep water not shown. b) Corresponding plot for the above cases as ice thickness vs. year.

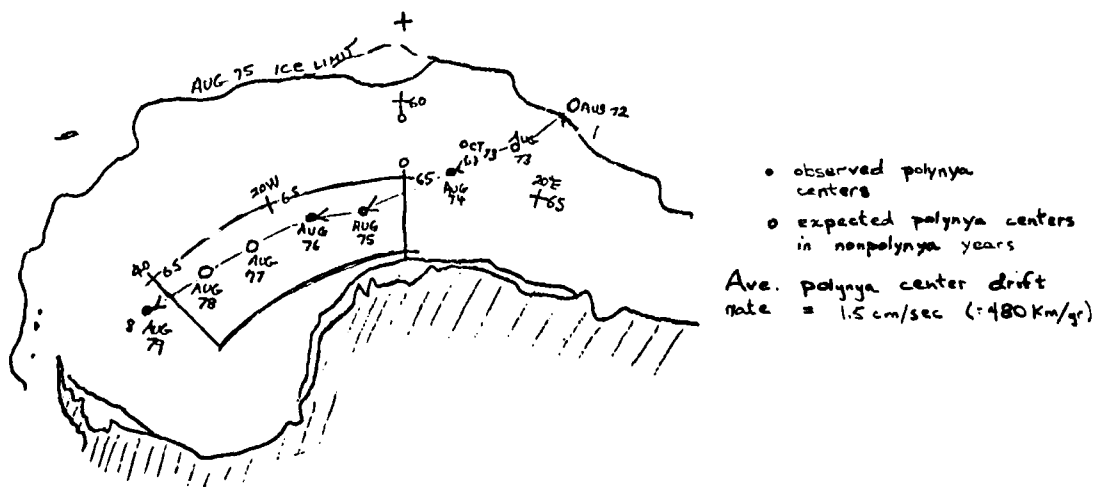


Fig. 10. Positions of observed and predicted polynya centers for 1972-1979. Box outlined represents region enclosing the stations with asterisks in Figure 2.

time scale. In state 2 a reduction of h_1 by one-half has the same effect as doubling F , although the time scale is now also halved before freezing will occur. Therefore the same amount of fresh water as usual should enter the system. During the freezing cycle, however, overturning will occur twice as fast and there is then a period of winter which is normally ice covered which will be receiving (at its increased rate) an input of F . The net effect over the year is to receive a much higher input of F . This F is persistent and not removed by overturning because after overturning there is still enough cooling left for late spring ice formation. Summer heating removes this ice and during the remaining summer and fall cooling more F is input resulting in lower salinity and more ice formation needed until overturning. The effects therefore of increasing F is not removed as more F is being stored in the larger volume of ice. The salinity decreases yearly until overturning is no longer possible.

Increasing of h_1 slows the response time and decreases the effects of F in the equations. In this case, however, the same amount of ice formation as for smaller h_1 is not enough to overturn the system and more ice is required. The time scale of ice formation has not been affected by varying h_1 so the system does not overturn until late in the season. The overturned water is now very warm and after the summer heating requires too much of the cooling cycle to refreeze. By the time it does start to form ice there is not enough cooling season left to generate the ice necessary for overturning. Therefore the effects of F have not been compensated and the upper layer slowly becomes fresher until overturning is impossible.

It can therefore be concluded that the effects of preconditioning are important. It is also interesting to note that in Fig. 10 the polynya which has formed during the time at which this paper was being written is not in the vicinity of Maud Rise but is in the belt previously mentioned. The implications of this have not been evaluated as yet, but it is worthy of mention that the polynya center appears to be drifting westward at the same rate as the mean calculated current of 1.5 cm/sec from their 1974 position over Maud Rise.

9. Conclusion

The model at this stage seems to contain the necessary basic physics required to simulate a quasi-periodic polynya situation. It would also appear to offer plausible answers to the three questions originally addressed. These are as follows:

1) The polynya occurs because of haline induced overturning due to the ejection of salt during ice buildup into a preconditioned upper level. This also suggests that there will be more ice production during polynya years.

2) The polynya occurs quasi-periodically because of the sensitive nature of the time scales on the various slopes on the T-S diagrams, especially for particular ranges of fresh water input. Some slight variation may also occur due to the variability of Q and F in nature.

3) Finally, the polynya occurs in the belt in which it has been observed because of a preconditioning responsible for positioning the depth of the surface layer at the position in which it is most susceptible to overturning for the amount of fresh water entering the system.

Acknowledgements

The author is extremely indebted to the entire GFD Staff and Fellows for helpful discussions, comments and suggestions. In particular thanks are due P. D. Killworth, who offered continual assistance and ideas. Also A. L. Gordon, G. Veronis and M. E. Stern contributed much in the way of ideas and suggestions which were incorporated into the paper.

REFERENCES

- Gordon, A. L., 1979. Meridional heat and salt flux in the Southern Ocean, GFD Lecture 2.
- Gordon, A. L., D. G. Martinson and H. Taylor, 1979. Wind driven circulation of the Weddell Gyre, in press.
- Killworth, P. D., 1979. On chimney formation in the ocean. Jour. Phys. Oceanogr., 531-544.

EXPERIMENT WITH DOUBLE DIFFUSIVE INTRUSIONS IN A ROTATING SYSTEM

Bert Rudels

Introduction

It is well established that the difference in the molecular diffusivities for heat and salt (or any other solutes) may create gravitational instabilities and convection in a stably stratified fluid (Stern, 1975; Turner, 1973). These instabilities most likely play an important part in the mixing and transformation of water masses in the ocean.

In the last couple of years experimental and theoretical work have been devoted to the effect of horizontal variations of heat and salt concentrations. Double diffusive intrusions have been studied (Turner, 1977). Compared to a nondiffusive intrusion the most striking effect is the much larger volume of fluid affected by the intrusion. Layers are created which move into the surrounding fluid driven by horizontal pressure gradients set up by the double diffusive convection. Because the greater mass flux across a "finger" interface compared to a "diffusive" interface the density changes in the layers and the flow will be across isopycnals. These effects may be of importance in frontal regions of the ocean where large lateral variations of salinity and temperature occur.

Works with double diffusive systems in a rotating frame, however, have been scanty. The experiments described below were initiated by some preliminary runs done by Stewart Turner at GFD earlier this summer, using salt and sugar. Some of these experiments showed a large-scale instability disrupting the intrusion. The experiments, in a crude way simulate an oceanic vortex. If instabilities occur due to double diffusion, the destruction of oceanic vortices may be enhanced. It is therefore important to explore the

evolution of the intrusion and the conditions favorable for instability. To accomplish this has been the aim of this work.

Experiments

A. Introduction

The work was done in the laboratory in Walsh Cottage. A square tank 38x38 cm was used and the fluid height was approximately 20 cm in each run. The experiments were done using salt (T) and sugar (S). A linear density gradient was set up by stirring a two-layer system with a screen while rotating, after which the density was measured at three levels, 15 cm, 10 cm, and 5 cm with a densimeter and the density gradient was computed. This method of creating a linear gradient seemed to work surprisingly well. Moreover, by using the grid the spin-up time could be reduced considerably. The injection was always at its own density level and kept as close to the center (vertically and horizontally) as possible. Because of the difficulty of making measurements while the experiments were running the main work was done by varying the initial parameters:

$$\text{Basic density stratification} = \frac{d\bar{\rho}}{dz}, \quad 0.001 < \frac{d\bar{\rho}}{dz} < 0.006 \text{ g cm}^{-4}$$

$$\text{Density of the intrusion} \quad \rho' = 1 + \rho_s \quad \rho' = 1.05, 1.07, 1.10 \text{ g cm}^{-3}$$

where ρ_s is the density due to sugar in the intrusion

$$\text{Rotation rate} \quad f = \frac{4\pi}{\text{period}} \quad 0.25 < f < 2.10 \text{ sec}^{-1}$$

Total amount of injected fluid = $Q(t) \text{ ml}$

The rate of flow was kept fairly constant at a rate of 1.5 ml/min.

The evolution of the quantities listed below were measured from photographs taken during the experiment:

R = radius of the well defined central core

h = height of the well defined central core

R_1 = maximum radius of intrusion

H = height of the convecting salt finger region above the central core

The flow profile was qualitatively explored by dropping dye into the tank. The main object of study, however, was the occurrence and evolution of the instability as a function of the initial conditions. A total of 29 runs were recorded in this way. Most of the experiments were with sugar solution injected into a salt stratification but some experiments (6) were done by injecting salt into sugar.

B. Description

1) Control

An injection without double diffusion will create motion in the system. Since the fluid is injected at the center it has no angular momentum and it will therefore start spinning anticyclonally as it is moving outwards. Also, because the density surfaces will be compressed above and below the intrusion, the whole fluid will gain relative negative vorticity.

A control experiment with salt into salt, for instance, was necessary. This experiment showed a stable perfectly axisymmetrical disc. The

vertical cross section seemed to be deviating slightly from a perfect ellipsoid and the radius was increasing faster than the Rossby radius computed from the amount of injected fluid. This more rapid increase may be due to viscous effects which slow down the zonal velocity of the disc and make it spread faster. The importance of viscosity was apparent because the relative angular velocity decreased rather than increased with distance from the source, as it would if only conservation of angular momentum was taken into account.

2) Experiments with Double Diffusion

a) Basic Features

When double diffusion was present the nature of the intrusion changed markedly. Because of the convection the vertical extent of the region affected by the intrusion was greatly increased. It was still possible, except in extremely unstable cases, to observe a well defined central core. This central core was assumed to represent the size and shape of the injected fluid and distinguished from the ambient fluid affected by the diffusive processes. When no instabilities were observed the central core had a distinct ellipsoid form. Above and below this core a large region of fluid was transformed by the double diffusive convection. The depth of this region was greater at the side of the salt fingers (we use the term salt fingers even if sugar fingers would be a more correct term to use in these experiments) where it assumed a cylindrical or flattened dome shape. The much shallower penetration on the "diffusive" side was terminated with a horizontal "diffusive" interface with roughly the same width as the core. More than one interface could be present in the vertical. Layering was also observed on the "finger" side. The number of layers was markedly lower and appeared to be more horizontal (when stable) than in the nonrotating case. The presence of

salt fingers greatly increases the exchange of momentum between the injected fluid and its surroundings, thereby distributing the added negative angular momentum over a larger volume, making it spin anticyclonally as a whole. Velocities were largest near the center of the tank, and decreased outwards. In this general anticyclonal flow there were regions where relative cyclonal flow was present. In cases where instability occurred, this cyclonal flow was stronger than the basic rotation having absolute cyclonal velocity.

b) The Instability

Apart from the regions of increased cyclonal zonal velocity, two features were distinct when the intrusion became unstable.

1) The instability occurred near the center of the intrusion and appeared like thrown out arms. These arms usually formed one by one, but in some cases when the salt was injected into sugar, they occurred in pairs.

When moving outwards the arms roughly kept their aximuthal position, indicating that regions with cyclonal velocity were thrown out. This belief was strengthened by the fact that the tip of the arms sometimes changed into vortices with weak but positive vorticity.

2) The whole intrusion seemed to become twisted vertically, giving the intrusion a beautiful helical shape. The twisting seemed to occur more than once, creating a number of intertwining helices, making the appearance of the intrusion more and more chaotic with time.

An observational connection between the arms and the helices could not be made for certain. In the most unstable cases the central core was totally disrupted and only the "halo" created by the diffusion could be seen.

Organization of Observations

The experiments indicated that the instability occurred most easily for low rotation rates and low stability, and for high concentration of the injected solute $S, (\tau)$ (differences in concentrations should be used if the injected solute is present in the ambient fluid).

In diagrams 1 and 2 the occurrence of instability is shown on a $\frac{N}{f}$ plane where $N = \left(\frac{g}{\rho'} \frac{d\bar{\rho}}{dz} \right)^{1/2}$ is the Brunt Vaisala frequency, ρ' kept constant. Diagram 3 shows the experiments on a ρ'/f -plane for constant density stratification.

The dependence upon ρ_s and $\frac{d\bar{\rho}}{dz}$ was expected, but the stabilizing effect of the rotation was rather surprising. These matters will be discussed further below.

To be able to order the observations we introduce the concept of an ideal intrusion. This intrusion is at each instant (each $Q(t)$) at its Rossby radius and we then have by definition

$$R_T = \left[\frac{g}{\rho'} \frac{d\bar{\rho}}{dz} h_T^2 \right]^{1/2} f^{-1} \tag{1}$$

$$Q(t) = \pi R_T^2 h_T \tag{assuming cylindrical shape}$$

which gives

$$R_T = \left[\frac{g}{\rho'} \frac{d\bar{\rho}}{dz} \right]^{1/6} \left[\frac{Q}{\pi f} \right]^{1/3} \tag{2}$$

$$h_T = \left[\frac{Q f^2 \rho'}{\pi g \frac{d\bar{\rho}}{dz}} \right]^{1/3}$$

By forming $\frac{R-R_T}{R_T}$ and $\frac{h-h_T}{h_T}$ we can then compare the evolution of the central core as a function of $Q(t)$ with this ideal case.

From the diagrams it can be seen that the observed radius is greater than R_T for large $Q(t)$ and the difference increases with Q . The opposite is true of the observed height h which is less than h_T and, here too the difference increases with Q .

These observations seem to indicate that volume is roughly conserved within the core and corresponds to the amount of injected fluid. The differences $R-R_T$, $h-h_T$ may be due to the changing density in the core and the changed density gradient in the convecting region which would give a different theoretical value of the Rossby radius. This cannot be the explanation for the salt injected into salt case which shows the same features. Here the difference is most probably due to viscous effects. The disc is slowed down and then spreads out faster. The shape also deviates from an ellipsoid which may explain why volume does not seem to be conserved in this case (h is measured at the center).

Diagram 6 shows $\frac{R_1 - R_T}{R_T}$, the maximum horizontal radius of the intrusion compared to the Rossby radius. As expected, R_1 is much larger than R_T and the difference increases with $Q(t)$. As a whole the observations show great scatter, especially at the start of each experiment (small Q), but they become less scattered with increasing Q .

To get a vertical scale H_T of the convecting region, which compares with its observed vertical extent H , we make the following idealizations of the double-diffusive convection.

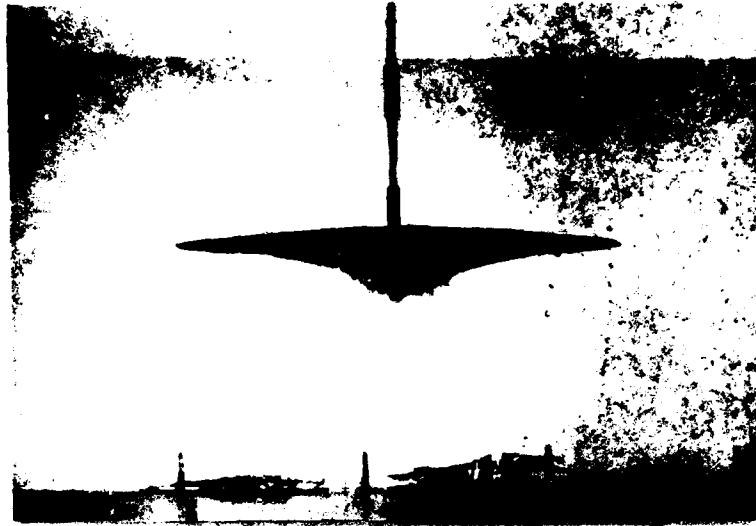


Fig. 1. Salt solution is injected, at its own density level, into a linear salt gradient

$$\rho' = 1.100 \text{ g/cm}^3, \quad \frac{d\bar{\rho}}{dz} = 0.002 \text{ g/cm}^4, \quad f = 0.80\text{s}^{-1}$$

Black tape on pipe - 2 cm. (The same on all figures)

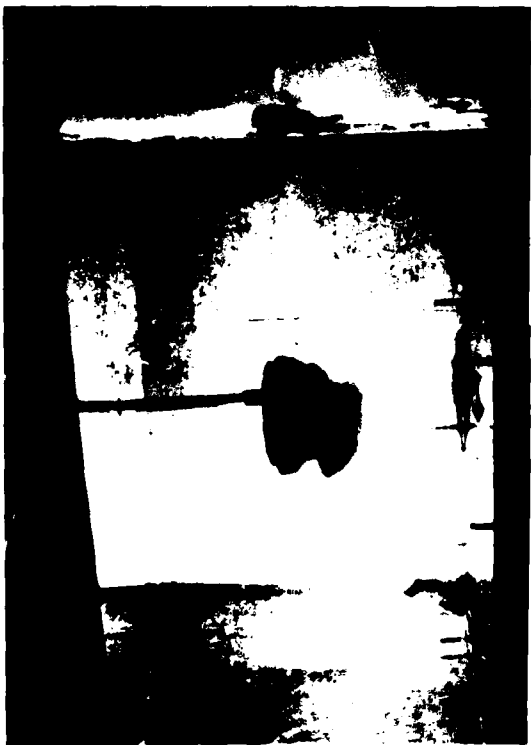


Fig. 2. Sugar solution is injected, at its own density level into a linear salt stratification.

$$\rho' = 1.100 \text{ g/cm}^2, \quad \frac{d\bar{\rho}}{dz} = 0.002 \text{ g/cm}^4, \quad \text{No rotation.}$$



3



4



5

Figs. 3-5. Sugar solution is injected, at its own density level, into a linear salt stratification.

$$\rho' = 1.100 \text{ g/cm}^3, \quad \frac{d\rho'}{dz} = 0.004 \text{ g/cm}^4, \quad f = 1.60\text{s}^{-1}.$$

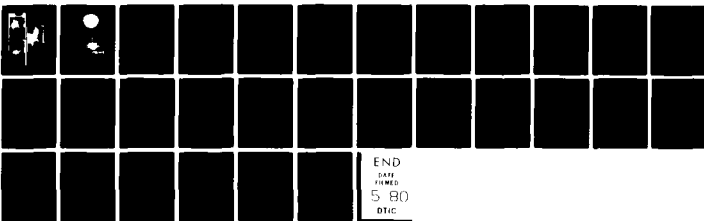
The exposures show the time evolution of a marginally stable run. Approximate time between the exposures are 5 minutes.

AD-A082 455

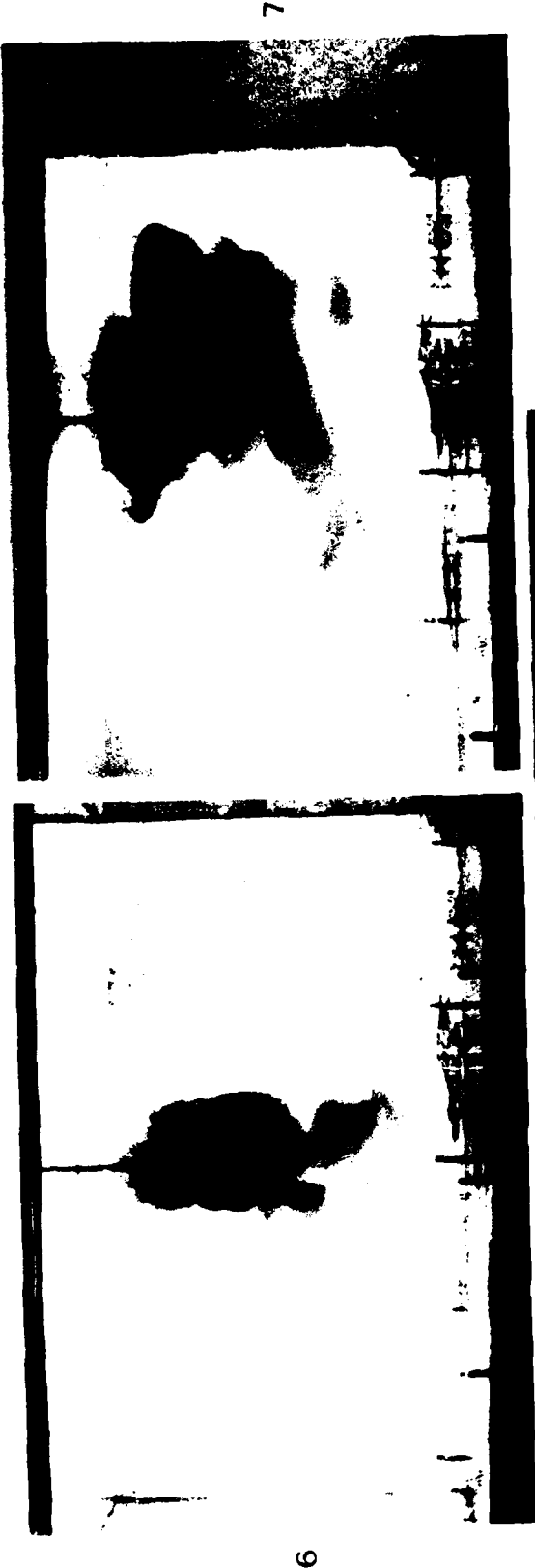
WOODS HOLE OCEANOGRAPHIC INSTITUTION MASS F/8 8/3
1979 SUMMER STUDY PROGRAM IN GEOPHYSICAL FLUID DYNAMICS AT THE --ETC(U)
NOV 79 M E STERN, F K MELLOR N00014-79-C-0671
UNCLASSIFIED WHOI-79-84-VOL-2 NL

3 1 3

W
207 107



END
DATE
FILMED
5 80
DTIC



Figs. 6-8. Sugar solution is injected, at its own density level, into a linear salt stratification.

$$\rho' = 1.100 \text{ g/cm}^3, \quad \frac{\Delta \rho}{\Delta z} = 0.001 \text{ g/cm}^4, \quad f = 0.50 \text{ s}^{-1}.$$

The exposures show the time evolution of a strongly unstable run. Approximate time between the exposures are 5 minutes.

The dye streaks on Fig. 8 indicate a strong zonal flow and a vertical shear. The motion is cyclonal at mid level, otherwise anticyclonal.

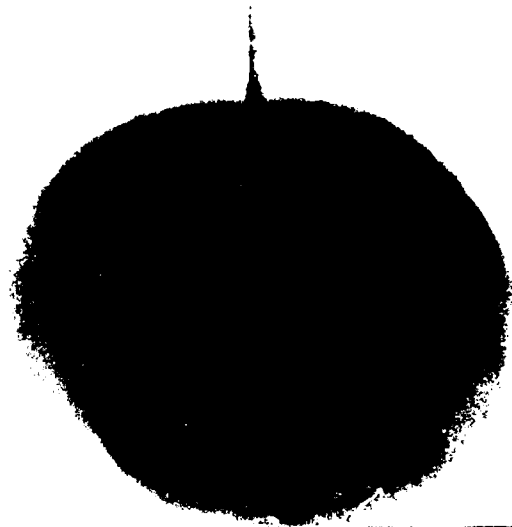


Fig. 9. Plan view of the same run (Figs. 6-8) showing evidence of one ejected "arm".



Fig. 10. Sugar solution is injected, at its own density level, into a linear salt gradient.

$$\rho' = 1.070 \text{ g/cm}, \quad \frac{d\rho}{dz} = 0.002 \text{ g/cm}^4, \quad f = 0.25\text{s}^{-1}.$$

The exposure shows clearly the helical features of the intrusion.

a) Only the mass transport carried by the fingers is considered important.

b) All ρ_s in the intrusion is exchanged for ρ_T with the ambient fluid. The flux F_s of sugar can be estimated from the relation $F_s = K(\rho_s)^{4/3}$, $K \approx 10^{-2} \text{ cm}^2\text{sec}^{-1}$ found by Stern and Turner (1969). We find that the fingers are capable of transporting the injected amount of sugar into the surrounding fluid during the time of an experimental run (~ 30 minutes). For the mass flux M between the intrusion and the ambient fluid the relation $M = \Delta\rho' h_T$ holds. $\Delta\rho'$ is the change of density in the intrusion.

c) The ratio F_T / F_s between the fluxes of salt and sugar is 0.9 (Stern and Turner, 1969). Using this value the density change in the intrusion can be written as

$$\Delta\rho' = \frac{1}{h_T} \left[\int_0^\infty F_T dt - \int_0^\infty F_s dt \right] = \frac{1}{h_T} \left[0.9 \rho_s h_T - \rho_s h_T \right] = 0.1 \rho_s$$

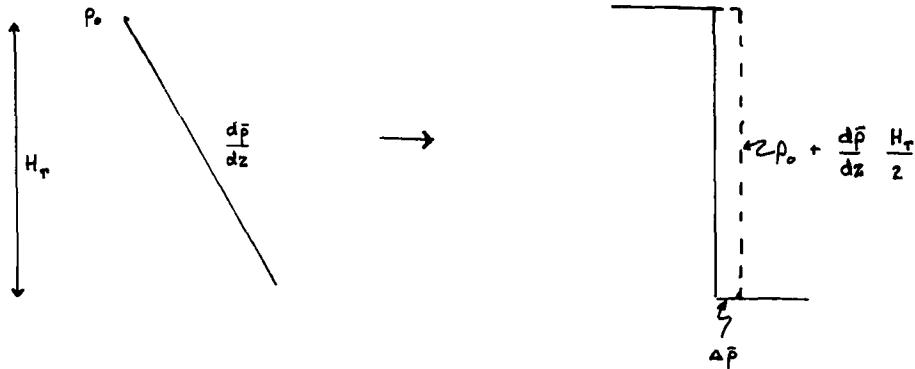
Note that the sign of $\Delta\rho'$ depends upon if salt or sugar is injected. In (a) and (b) we have neglected the concentration changes in the ambient fluid. If these are taken into account, the total exchange would be less by a factor of h_T / H_T .

d) There is no radial variation of the diffusion. This should be justified when the lateral scale of the intrusion is small, that is, for large δ and small $\frac{d\bar{p}}{dz}$.

(e) All release of buoyancy by the fingers is used to rearrange the density field from a linear gradient into a step profile. This is a dangerous assumption because of the high viscosity of the fingers.

However, all assumptions except (d) should tend to give an overestimate of the height H_T compared to the observed value.

Apply the conservation of energy to the system



we get

$$\int_0^{H_T} g \left[\rho_0 + \frac{d\bar{p}}{dz} z \right] z dz = \int_0^{H_T} g \left[\rho_0 + \frac{d\bar{p}}{dz} \frac{H_T}{2} - \Delta\bar{p} \right] z dz - \int_0^{H_T} g m(z) z dz \quad (3)$$

where $\Delta\bar{p}$ is the change of mean density in the fluid between zero and H_T and $m(z)$ is the vertical mass flux/unit depth and area.

Because of the linear initial gradient we assume

$$m(z) = c(H_T - z)$$

and since

$$\Delta\bar{p} = \frac{1}{H_T} \int_0^{H_T} m(z) dz$$

we get

$$m(z) = \frac{2(H_T - z)}{H_T} \Delta\bar{p}$$

which inserted into the energy equation gives

$$H_T = \frac{10 \Delta\bar{p}}{\frac{d\bar{p}}{dz}} \quad (4)$$

since we have

$$\Delta \bar{p} = \frac{h_T}{H_T} \Delta p' = \frac{h_T}{H_T} 0.1 \rho_s$$

we may write H_T as a function of the initial conditions

$$H_T = \rho_s^{1/2} \left[\frac{Q \rho}{\pi g} \right]^{1/6} f^{1/3} \frac{d\bar{p}}{dz}^{-2/3} \quad (5)$$

The expression shows that H_T increases slower with Q than R_T and h_T .

We see that H_T is an overestimate of the convecting region H as it should be, but the difference $H - H_T$ diminishes when f and $\frac{d\bar{p}}{dz}$ become large. This is the case when (d) becomes most violated. The other assumptions do not depend upon variations of these quantities so they should be as good or as bad for all f and $\frac{d\bar{p}}{dz}$. The variation with $Q(t)$ is not as great as the diagram seems to indicate. Instead $H - H_T$ tends to approach a constant value when Q becomes large. For the most part the scatter is due to variation of initial parameters especially f and suggesting that the functional dependence of these parameters given by (5) is not quite correct in describing the evolution of depth of the convecting region.

Qualitative Criteria for Instability

Because of double diffusion the whole volume of the intrusion has become a center of high relative vorticity. The strength of this vorticity ζ should be compared to the basic vorticity f . To find ζ/ρ we need to get an estimate of the zonal flow induced by the change in the density

field. We will assume a geostrophically balanced flow

$$-fv = -\frac{1}{\rho} \frac{\partial p}{\partial r} \quad \left(\text{ignoring the term } \frac{v^2}{r} \right) \quad (6)$$

and compute the pressure gradient due to the vertical mass flux. The vertical mass flux per unit area that can be carried by the fingers is given by

$$M = \int_0^{\infty} m(z) dz = 0.1 \rho_s h_T = \frac{0.1 \rho_s Q}{\pi R_T^2}$$

Here assumptions (a) and (b) above have been used. We may note that to get the mass transport it is not necessary to assume anything about the amount of energy being used to change the density profile. The pressure gradient is then estimated by

$$\frac{\partial p}{\partial r} = \frac{0.1 \rho_s g Q}{\pi R_T^3}$$

and the zonal velocity becomes

$$v = \frac{0.1 \pi \rho_s g^{1/2}}{\left[\rho' \frac{d\rho}{dz} \right]^{1/2}} = \frac{0.1 \pi \rho_s}{N} \quad (7)$$

when R_T is expressed by the initial parameters. Surprisingly the zonal velocity appears to be independent of the rotation rate. It was not possible in the experiment to find if this actually was the case since other effects, due to the injection of fluid and to the instability itself, prevented good estimates. It seems, however, to agree with the observed fact that a low rotation rate was destabilizing.

Approximating the relative vorticity with

$$\xi = \frac{v}{R_r}$$

we find that

$$\frac{\xi}{f} = \frac{v}{R_r f} = \left[\frac{\pi g}{\rho'} \right]^{1/3} \frac{0.1 \rho_s}{\left[\frac{d\bar{p}}{dz} f \right]^{2/3}} Q^{1/3} \quad (8)$$

to get a neater expression we write

$$\frac{\xi}{f} = A \frac{\rho_s}{\frac{d\bar{p}}{dz} \left[\frac{Q f^2}{N^2} \right]^{1/3}} \quad (9)$$

Equation (9) is a function of time through $Q(t)$. Each experiment has its own $\xi/f(Q)$ curve. The curves from the stable experiments fall below the curves from the unstable ones as would be expected. The transition from stable to unstable runs occurs over a quite narrow range of ξ/f - only 1/10th of the total experiment range.

Remark: The flow could be considered from the point of view of energetics. The rotational kinetic energy generated by the pressure field resulting from the convection has to be contained in a volume with a basic solid body rotation. The ratio between this energy and the energy of the same volume in solid body rotation has the form $\sim v^2 / [f R_r]^2$ (note the resemblance with the equation (8)). This ratio suggests that the flow induced by the double-diffusive convection might become too energetic to be contained in the volume affected by the convection. The flow has to lower its energy density by expanding drastically. It goes unstable.

It is seen that the occurrence of instability is closely related to the amount of relative vorticity generated by the diffusion (Diagram 8). We may find by choosing Q the value ζ/f above which the intrusion is unstable. For instance,

$$Q = 100, \rightarrow \zeta/f \sim 3.5$$

(The runs with salt injected into sugar seemed to give a higher value (Diagram 9). Too few runs were, however, made to establish this as a fact.)

The representation is not good because of its time dependence through Q . A nondimensional representation can be given by plotting

$$\left[\frac{g}{\rho'} \right] \frac{\rho_2 Q^{1/3}}{f^2} \quad \text{versus} \quad Q^{1/3} \left[\frac{\rho_2}{\frac{d\rho}{dz}} \right]$$

for any particular Q .

The slope of the time dividing the stable from the instable experiments is given by $N^2/f^2 \sim -1$

and is constant for all Q . The position of the line, however, changes with Q .

Discussion

a) The Instability

The intrusion is assumed to always keep its Rossby radius as it

expands. The double diffusive convection changes the density of the intrusion and the surrounding density field. The theoretical value of the Rossby radius then increases and the intrusion has to adjust to keep up with the changes. In some cases this adjustment is easily done and the disc grows gently to its new size. In the unstable cases the change in Rossby radius is too great and sudden. The central core is disrupted and expands violently to its new size. This means that in experiments with a constant injection of fluid the strongly unstable cases are never able to build up a stable central core but always have to start anew, pass through the singular destabilizing phase, and get disrupted.

The fact that the instability acts to increase the rate of expansion of the intrusion seems to suggest a barotropic, or even centrifugal, type of instability rather than a baroclinic one, even if the energy available to the instability comes from the creation of a baroclinic density field.

b) Zonal Velocities and the Helical Shape

The whole region of the intrusion has an anticyclonal rotation due to the injection of fluid with zero angular momentum. This angular momentum is rapidly distributed over the convecting region because of the high viscosity due to the salt fingers.

However, in addition to this the downward mass flux creates a low pressure zone inside the convective region. A corresponding cyclonal flow is then generated inside the general anticyclonic circulation. Because the vorticity has to be conserved a corresponding anticyclonal flow must be generated somewhere in the fluid. If the double diffusion redistributes density in the vertical this anticyclonal flow may occur inside the convective

region. Otherwise a barotropic anticyclonic circulation must be generated in the whole fluid. This may be done by a horizontal squashing of the diffusive region which will raise the free surface and create a general anticyclonic flow (Fig. 11 and 12).

The vertical shear, thus being present, acts upon the highly viscous convective region. This region will then become twisted by the zonal flow, somewhat like a bar twisted vertically, if the viscosity is strong enough. A simple kinematic feature like this may help to explain the observed helical shape of the convective region.

These thoughts must, however, remain highly speculative since not enough is known about the nature of the flow inside the convective region or about its interaction with the salt fingers. The helical shape can be generated in an altogether different way, more closely related to the double-diffusive mechanisms and the instability.

Conclusions

The experiments show that strong zonal motions, and even instabilities may occur when an intrusion interacts with its environment through double diffusive convection.

A general criteria for the occurrence of instability could not be found because of the continuous increase of volume Q of the injected fluid. However, the lines of marginal stability were seen to have the same slope for all Q . The position of the time was shifted towards the origin with increased Q .

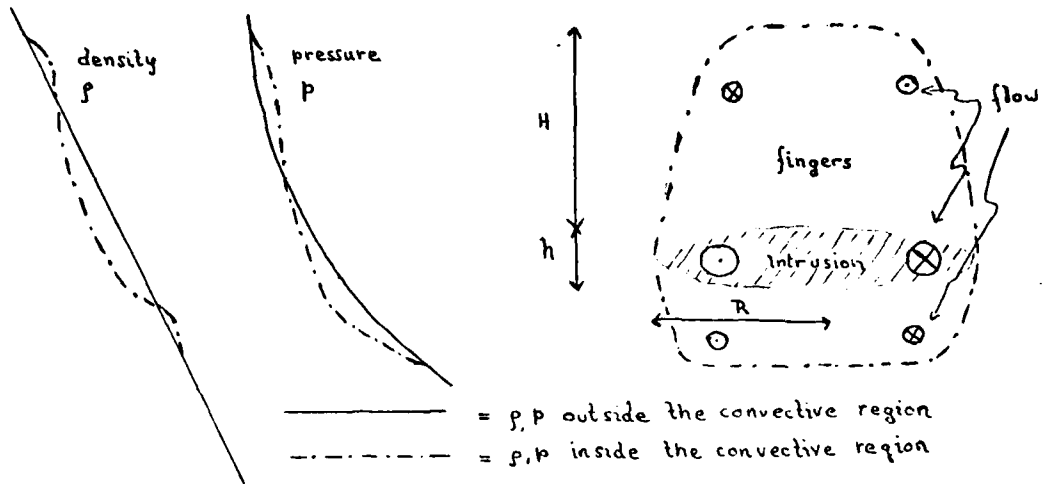


Fig. 11. Sketch of possible density- and pressure distribution and the associated flow pattern when some redistribution of mass occurs.

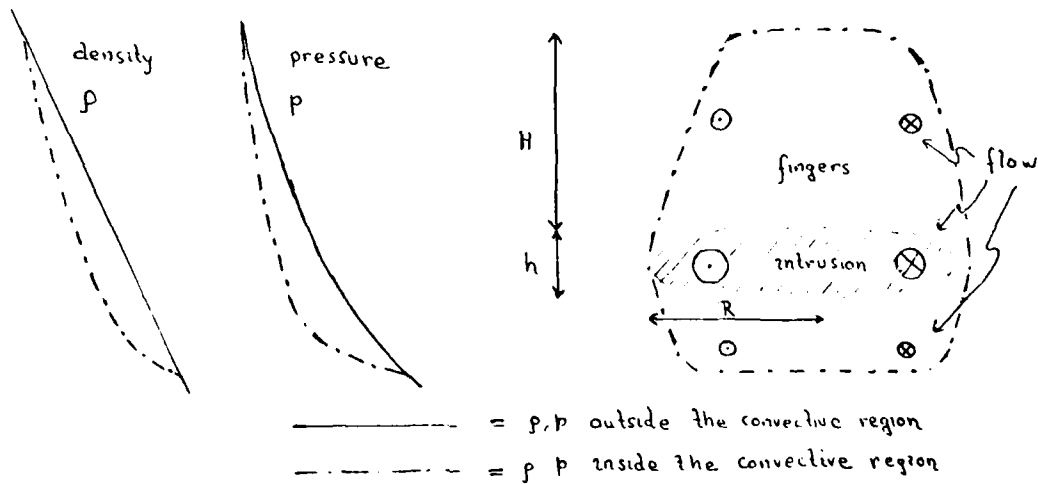


Fig. 12. Sketch of possible density- and pressure distribution and the associated flow pattern when no redistribution of mass occurs.

These experiments suggest ways in which the molecular effects may influence motions on a larger scale in the oceans. Cyclonal velocities created by the downward mass flux may be present in the subsurface cyclonal eddies that have been observed in the Arctic (Hunkins, 1974). These eddies showed high cyclonal velocities connected with intrusions of anomalously cold water.

The transformation and mixing of oceanic eddies can also be speeded up considerably if these eddies become unstable and disrupt. Because of the lack of field observations these thoughts should be regarded as speculations.

Acknowledgements

I would like to thank Stewart Turner for introducing me to the experiment, Melvin Stern for his guidance during the work, Adrian Gill, Louis Howard, and George Veronis for many discussions. Thanks is also due to Robert Frazel for all his help and to Florence Mellor and Maryanne Macaluso for their work with the manuscript.

REFERENCES

- Hunkins, K. L., 1974. Subsurface eddies in the Arctic Ocean. Deep-Sea Res., 21, 1017-1033.
- Stern, M. E., 1975. Ocean Circulation Physics. New York, Academic Press.
- Stern, M. E. and J. S. Turner, 1969. Salt fingers and convecting layers. Deep-Sea Res., 16, 497-511.
- Turner, J. S., 1973. Buoyancy effects in fluids. London, Cambridge Univ. Press.
- Turner, J. S., 1978. Double-diffusive intrusions into a density gradient. Jour. Geophys. Res., 83, 2887-2901.

BOUNDARY DENSITY CURRENTS OF UNIFORM
POTENTIAL VORTICITY

Bach-Lien Hua

Introduction

Oceanic examples of boundary density currents can be found in regions of abyssal western boundary currents. Their time-dependent behavior is related to the intermittent formation of cold water that sinks in wintertime to the bottom of polar coastal regions (Wadhams, Gill and Linden, 1979). The structure of each current, their width and stability, are questions of great importance since their temperature determines the mean temperature of the bottom of the oceans. The same features, upside down can be found when fresh water from coastal source debouches in a plume in saltier water. The effect of rotation compensates lateral spreading due to buoyancy forces and constrains the light water to flow along the coast in a confined current which is geostrophic behind the nose of the intrusion.

The rate of propagation of the nose of the intrusion and some nonlinear dynamics on the trailing geostrophic front have been examined by Stern (1979), but with the restriction to flows of zero potential vorticity. Such flows appear as the simplest generalization of nonrotating irrotational flows and a possible realization is when the intrusion comes from an infinitely deep reservoir (Whitehead, Leetma and Knox, 1974).

This summer's work is an extension of Stern's paper and considers flows of finite potential vorticity, first for an intrusion overlying an infinitely deep layer at rest (Section III) and the interaction with the dynamics of a second layer of finite depth is taken into account in the last section.

The equations describing such flows are complex and would require a thorough numerical reduction. We have then chosen to concentrate our attention on two main points:

1) Investigate if the result found by Stern (1979) that there exists a limiting width of the boundary current for a bore-like steady intrusion propagate, is still valid for finite potential vorticity flows in a two-layer ocean and find numerically that value.

2) See qualitatively if some nonlinear waves found in Stern (1979) have their analogs in our problem.

II. Experiments

Some qualitative experiments relevant to the above dynamics were conducted with the set-up represented on Fig. 1. In a rotating channel, light fluid is separated from a heavier one by a vertical barrier and the ensemble is brought to a state of solid rotation. At initial time the barrier is pulled up. If the channel was not rotating, light fluid would be raised buoyantly over the heavier one and the flow would be uniform through the section. If the fluid were rotating, but if there were no lateral walls, we would face the classical problem of geostrophic adjustment. Because of the Coriolis force, the flow is parallel to the pressure gradient and the limit between light and heavy fluid is displaced to the right (facing the flow) on a distance of a Rossby radius of deformation. In this case, the presence of the lateral wall deviates the light fluid in a boundary flow that is constrained by rotation to flow along the right wall (looking downstream) in a confined current of width comparable to the Rossby radius of deformation.

Some features observed in the experiments have been sketched on Fig. 1. The flow presents a very complicated pattern just in the corner behind the initial position of the barrier, where the flow of light fluid strikes the lateral wall.

Downstream of this very complex region, the intrusion appears to be parallel, laminar and steady, upstream of the nose of the intrusion. The

speed of propagation of the nose appears to be uniform in time and its shape looks unchanged while it advances downstream.

The range of some parameters chosen for the experiments are

rotation range	$\omega = f/2$	$0.2 - 1\text{s}^{-1}$
density difference		10^{-3}
Rossby radius of deformation		2.5 cm
width of the channel		15 cm

The lateral frictional boundary layer thickness in our experiments was around 1 mm, so that the influence friction may be neglected on the boundary current, except in the incipient frontal part of the intrusion. After some time, certain experiments were unstable and finite amplitude wave patterns could be seen on the trailing front behind the nose and some observed waves would steepen and break towards the upstream direction and bumps in height and width of the current, associated with those waves, would appear almost in phase.

This experiment is the rotating analog of densimetric exchange flows in rectangular channels (Barr, 1972). The analysis of the actual rotating experiment is complicated by the possible influence of the other lateral wall on the light fluid intrusion. However, we expect, as shown by Gill (1976), that if the radius of deformation is small compared with the channel width, as a first approximation, the influence of the other lateral wall may be neglected.

The existence of the frontal wall that ends the channel may also cause reflection of surges at the interface between the two fluids once the density current has reached the frontal wall. But the greatest complication in analyzing the experiment results from the region on the corner just behind the initial position of the barrier, where a sort of complicated adjustment occurs

and from which a laminar intrusion emerges. In this corner region, both highly transient and short-wave effects occur, therefore, the following theory cannot be taken into account. The situation, as idealized from the experiment, may be applied to the laminar intrusion. The parallel flow behind the incipient nose will be referred to hereafter as the upstream state as opposed to the nose itself. We then deal with a boundary current, constrained along a straight coast, and presenting a density front.

One important premise is the conservation of potential vorticity in each layer (both the intrusion layer and the bottom layer). This supposes that changes in potential vorticity induced by mixing and friction may be neglected, so that modelling by an ideal fluid can only be applied over limited path lengths. Moreover, as in the experiment, we will restrict our attention to initial distributions corresponding to uniform potential vorticity in both layers, since at initial time both light and heavy fluids have uniform potential vorticity $1/H_i$ ($i = 1, 2$) where H_i is the initial height. (Experiments were also conducted for $H_1 \neq H_2$, the heavier fluid having an L-shaped distribution, lying on both sides of the barrier and on the bottom beneath the light fluid, in the light fluid compartment.)

III. Density Current of Finite Potential Vorticity

1) Equations: We shall first consider the case of an intrusion overlying an infinitely deep inactive ocean. If η denotes the depth of the intrusion, k designates the vertical axis, and $f/2$ is the angular velocity, the hydrostatic equations for the horizontal velocity \underline{v} are:

$$\frac{\partial \underline{v}}{\partial t} + (f + \zeta) \underline{k} \times \underline{v} = - \nabla (g\eta + \underline{v}^2/2) \quad (1)$$

$$\frac{\partial \eta}{\partial t} + \nabla \cdot \underline{v} \eta = 0 \quad (2)$$

where $\zeta = \underline{k} \cdot \nabla \times \underline{y}$ is the relative vorticity. (1) and (2) imply that $\frac{d}{dt} \left(\frac{\zeta + f}{\eta} \right) = 0$ so that for a uniform potential vorticity distribution $\frac{1}{H}$, this yields: $\frac{\zeta + f}{\eta} = \frac{f}{H}$

- adimensionalization:

We introduce the following nondimensional quantities:

$$\eta = H_0 \hat{h}$$

$$y = (gH_0)^{1/2} f^{-1} \hat{y}$$

$$x = \epsilon^{-1} (gH_0)^{1/2} f^{-1} \hat{x}$$

$$u = (gH_0)^{1/2} \hat{u}$$

$$v = \epsilon (gH_0)^{1/2} \hat{v}$$

$$t = \epsilon^{-1} f^{-1} \hat{t}$$

H_0 designates the height scale, and ϵ is the ratio of the length scale in the y-direction over the length scale in x-direction.

Hereafter, the notation $\hat{\quad}$ denoting nondimensional quantities will be omitted. The equations in nondimensional form are:

for x-momentum equation: (3)

$$u_x - (1 + u_y - \epsilon^2 v_x) v = -(h + \frac{u^2}{2} + \frac{\epsilon^2 v^2}{2})_x$$

for y-momentum equation: (4)

$$\epsilon^2 v_t + (1 - \epsilon^2 v_x) u = -(h + \frac{\epsilon^2 v^2}{2})_y$$

for continuity equation: (5)

$$h_t + (hu)_x + (hv)_y = 0$$

for vorticity equation: (6)

$$(1 + u_y - \xi^2 v_x) = h/H$$

If $L(x,t)$ denotes the nondimensional displacement of the front ($h = 0$) from the wall, the boundary conditions may be written as:

no normal flux at the wall:

$$v(x,0,t) = 0 \quad (7)$$

The height goes to zero on the free streamline $y = L(x,t)$.

$$h(x,L(x,t),t) = 0 \quad (8)$$

Kinematic condition on the free streamline:

$$v(x,L(x,t),t) = \frac{dL}{dt} \quad (9)$$

The height far upstream behind the nose is chosen to scale the heights in the problem:

$$h(-\infty,0,t) = 1 \quad (10)$$

- straight boundary current:

A new level of approximation appears when we consider the case where the downstream variations are small compared to the nonstream direction, i.e., for the limit $\xi \rightarrow 0$, equations (3) to (6) then become:

$$u_t - (1 + u_y)v = -(h + u^2/2)_x \quad (11)$$

$$u = -h_y \quad (12)$$

$$h_t + (hu)_x + (hv)_y = 0 \quad (13)$$

$$(1 + u_y) = h/H \quad (14)$$

This formal expansion yields the result that the downstream current is geostrophic. Equations (12) and (13) give:

$$h_{yy} - \frac{h}{H} = 1 \quad (15)$$

Using (8) the variables $u(x,y,t)$ and $h(x,y,t)$ can be written as:

$$h(x,y,t) = H \left[1 - \cosh\left(\frac{L-y}{H^{1/2}}\right) \right] + H^{1/2} U \sinh\left(\frac{L-y}{H^{1/2}}\right) \quad (16)$$

$$u(x,y,t) = H^{1/2} \sinh\left(\frac{L-y}{H^{1/2}}\right) + U \cosh\left(\frac{L-y}{H^{1/2}}\right) \quad (17)$$

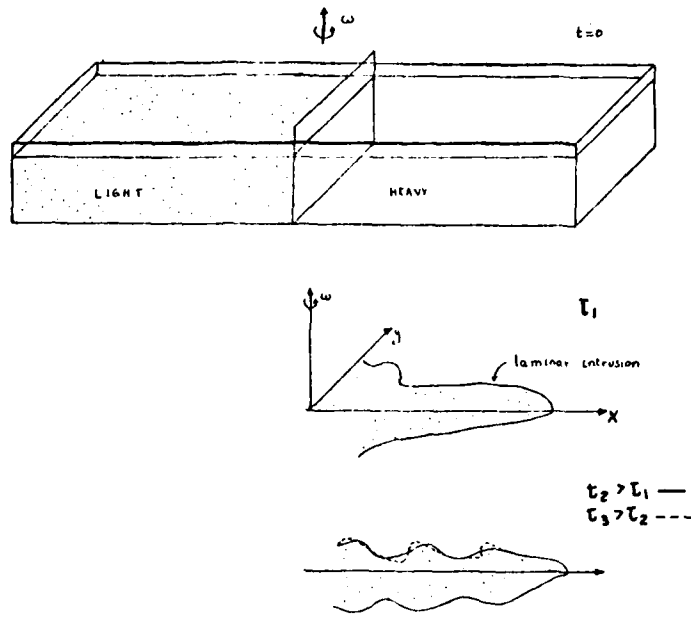


Fig. 1. Experimental set-up.

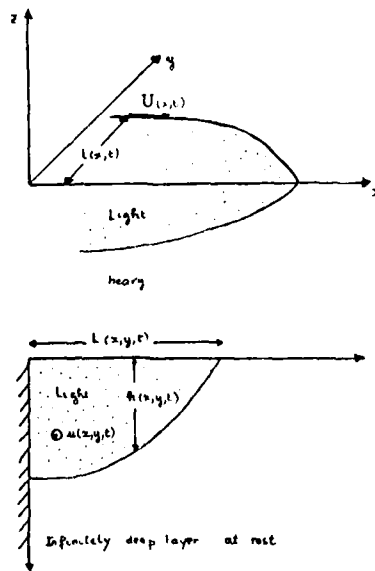


Fig. 2. Intrusion over an inactive deep layer.

where $L = L(x,t)$ and $U = U(x,t)$ are defined as (Fig. 2) the y -displacement relative to the wall of the density front and the downstream velocity on that free streamline; both quantities are only functions of x and t . We can notice that in (16) and (17) the x and y dependence are separate. Using (7), (8) and (9) the equation of continuity integrated across a given section can be written as:

$$\frac{\partial}{\partial t} \int_0^L h \, dy + \frac{\partial}{\partial x} \int_0^L h u \, dy = 0 \quad (18)$$

The system of equations that $U(x,t)$ must satisfy are obtained by replacing (16) and (17) in (18) and (11) taken on the free streamline $y = L$:

$$\frac{\partial U}{\partial t} + U \frac{\partial U}{\partial x} - \frac{\partial L}{\partial t} = 0 \quad (19)$$

$$\begin{aligned} & \left(\frac{U}{H^{1/2}} \sinh \frac{L}{H^{1/2}} \right) \frac{\partial L}{\partial t} + \left(\frac{U}{H^{1/2}} \sinh \frac{L}{H^{1/2}} - \cosh \frac{L}{H^{1/2}} + 1 \right) \left(\frac{U}{H^{1/2}} \cosh \frac{L}{H^{1/2}} - \sinh \frac{L}{H^{1/2}} \right) \frac{\partial L}{\partial x} \\ & + \left(\frac{U}{H^{1/2}} \cosh \frac{L}{H^{1/2}} - \sinh \frac{L}{H^{1/2}} \right) \left(\cosh \frac{L}{H^{1/2}} - 1 \right) \frac{\partial U}{\partial x} = 0 \end{aligned} \quad (20)$$

If we seek solutions of (18) and (19) having a time invariant functional relation between $U(x,t)$ and $L(x,t)$, i.e. $U = U(L)$ such as:

$$\frac{\partial U}{\partial t} = U'(L) \frac{\partial L}{\partial t} \quad \text{and} \quad \frac{\partial U}{\partial x} = U'(L) \frac{\partial L}{\partial x}$$

if this functional relation is satisfied at some initial time, then U and L are independent of time at a point $x = x(t)$ which moves with the propagation speed:

$$\frac{dx}{dt} = \frac{UU'}{U'-1} \quad (21)$$

2) Resolution by Riemann Invariants

Equations (19) and (20) are hyperbolic and equasi-linear (i.e. of first order in terms of partial derivatives of L and U) and can be solved by the method of characteristics, yielding: $\frac{\partial}{\partial t} + d_{\pm} \frac{\partial}{\partial x} R_{\pm}(U,L) = 0$, where curves such as $R_{\pm}(U,L) = \text{constant}$ correspond to the Riemann invariants of the problem, i.e., curves along which a functional relation between U and L remains unchanged for an observer moving at speed d_{\pm} . The O.D.E. yielding the Riemann invariants can be written as:

$$\frac{dU}{dL} = 1 - \frac{(2U/H^{1/2}) \cosh(L/2H^{1/2})}{a \pm \sqrt{a^2 + b}} \quad (22)$$

with

$$a = \sinh \frac{L}{H^{1/2}} \left(\cosh \frac{L}{2H^{1/2}} - \frac{U}{H^{1/2}} \sinh \frac{L}{H^{1/2}} \right)$$

$$b = 2 \sinh \frac{L}{H^{1/2}} \left(\frac{U}{H^{1/2}} \cosh \frac{L}{H^{1/2}} - \sinh \frac{L}{H^{1/2}} \right)$$

The characteristic slopes in (x,t) space are

$$d_{\pm} = \frac{(U/H^{1/2}) \cosh(L/H^{1/2}) - \sinh(4H^{1/2})}{\cosh\left(\frac{L}{H^{1/2}}\right) + 1 \mp \left\{ \frac{2 \sinh\left(\frac{L}{H^{1/2}}\right) \sinh^3(L/2H^{1/2}) \cdot \frac{U}{H^{1/2}} - \cosh^3\left(\frac{L}{2H^{1/2}}\right) + 2 \cosh(L/2H^{1/2}) \right\}^{1/2}} \frac{U}{H^{1/2}} \cosh\left(\frac{L}{2H^{1/2}}\right) - \sinh\left(\frac{L}{2H^{1/2}}\right)} \quad (23)$$

- The U-axis (i.e. $L=0$) which is the locus of the nose state points: at such points one can verify from equation (21) that the propagation speed equals the downstream velocity ($U(L=0)$).

3) Bore and Wedges Solutions:

Solutions obtained for + and - signs for the Riemann Invariants correspond to very different physical behaviors which have been called wedge and bore solutions

- Wedge solutions, correspond to the + sign.

As can be seen from Figs. 3, 4 and 5, the \oplus curve passing through a given upstream state point Q corresponds to a flow where the velocity of the nose $U(L=0)$ is larger than the velocity in the parallel upstream current behind the nose, so that the incipient part of the intrusion becomes thinner as time increases. This frontal behavior is called a wedge in analogy with the behavior of the wedge that exists in the nonrotating dam break problem. For such intrusions, frictional forces in the nose region become important after a certain time. The distinguishing feature is that the energy flux in the nose is divergent and cannot compensate frictional terms, and this class of solutions cannot lead to a steady picture of the shape of the nose.

For the case of zero potential vorticity $1/H = 0$ (Fig. 3), the maximum width for the parallel current upstream of the wedge nose corresponds to the \oplus Riemann curve passing through R, i.e. $L_{\max} = \sqrt{2}$. For the intermediate case $1/H = 2$, the width is larger (Fig. 4): $L_{\max} = 1.86$. For given H, one can show that the maximum width of the upstream parallel current corresponding to a wedge solution is:

$$L_{\max} = H^{1/2} \cosh^{-1} \left(\frac{H}{H-1} \right)$$

The limit case where $1/H \rightarrow 0$ (zero potential vorticity) corresponds to Stern (1979) and an expansion in series of $\frac{U}{H^{1/2}}$ and $\frac{L}{H^{1/2}}$ in that case in (22) and (23) yields the same solutions as in Stern's paper. Resolution of (22) and (23) gives U and L and we have seen that all the variables of the problem can be expressed in terms of U and L. A. Gill (personal communication) has shown that the whole problem could also be formulated in terms of $L(x,t)$ and $M(x,t) = 2h_0(x,t)^{1/2}$ where $h_0 = h(x,0,t)$.

Equation (22) has been integrated numerically using a Runge-Kutta second order scheme and Riemann invariants waves have been plotted for $1/H = 0$, $1/H = 1/2$ and $1/H = 1$ (Figs. 3, 4 and 5) in the phase space (U,L). Some particular locii in this phase space are:

- Curve OR, which represents the locus of sections of the intrusions (given U and L), where the downstream velocity at the wall goes to zero (points such as)

$$\frac{U}{H^{1/2}} = \tanh \frac{L}{H^{1/2}}$$

- The locus of upstream state points (as defined by (10)), which corresponds to the dotted line PQR: its extension is limited for large L by point R where the flow reverses at the wall. PQR is defined by:

$$\frac{U}{H^{1/2}} = \coth \frac{L}{H^{1/2}} - \frac{H-1}{H} \frac{1}{\sinh(4H^{1/2})}$$

- Curve OH, which represents the sections where the height of the intrusion at the wall goes to zero: points lying below curve OH have no physical meaning since they would correspond to negative heights at the wall, or is defined by

$$\frac{U}{H^{1/2}} = \tanh \frac{L}{2H^{1/2}}$$

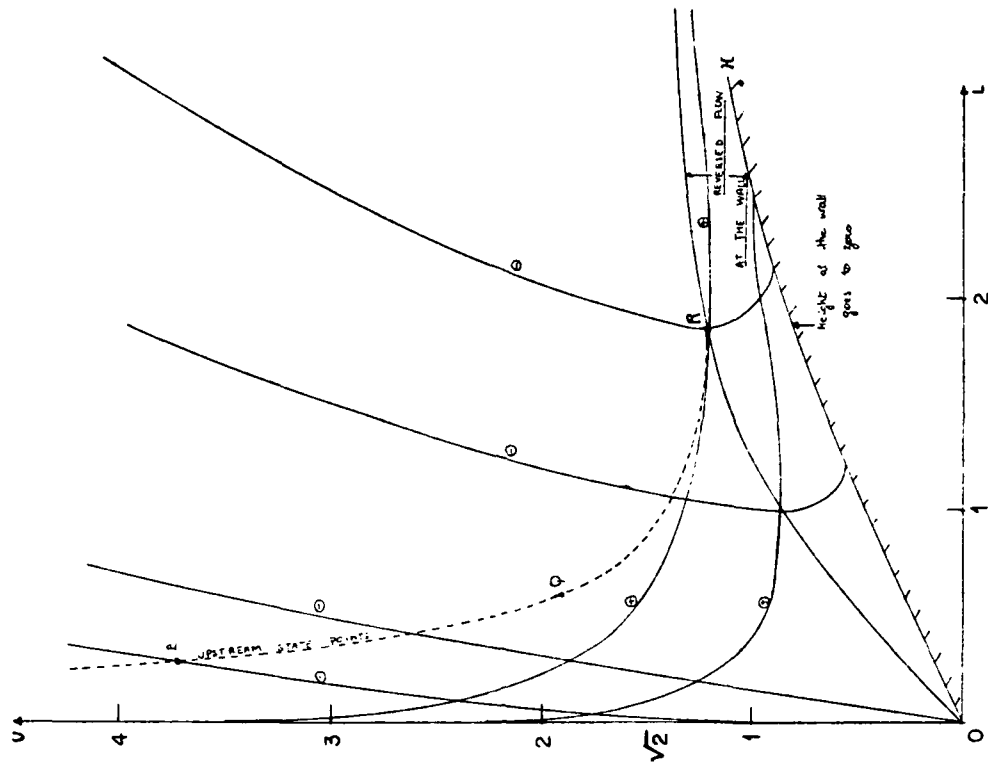


Fig. 4. Intrusion of finite potential vorticity. $1/H = 0.5$. - Riemann invariants.

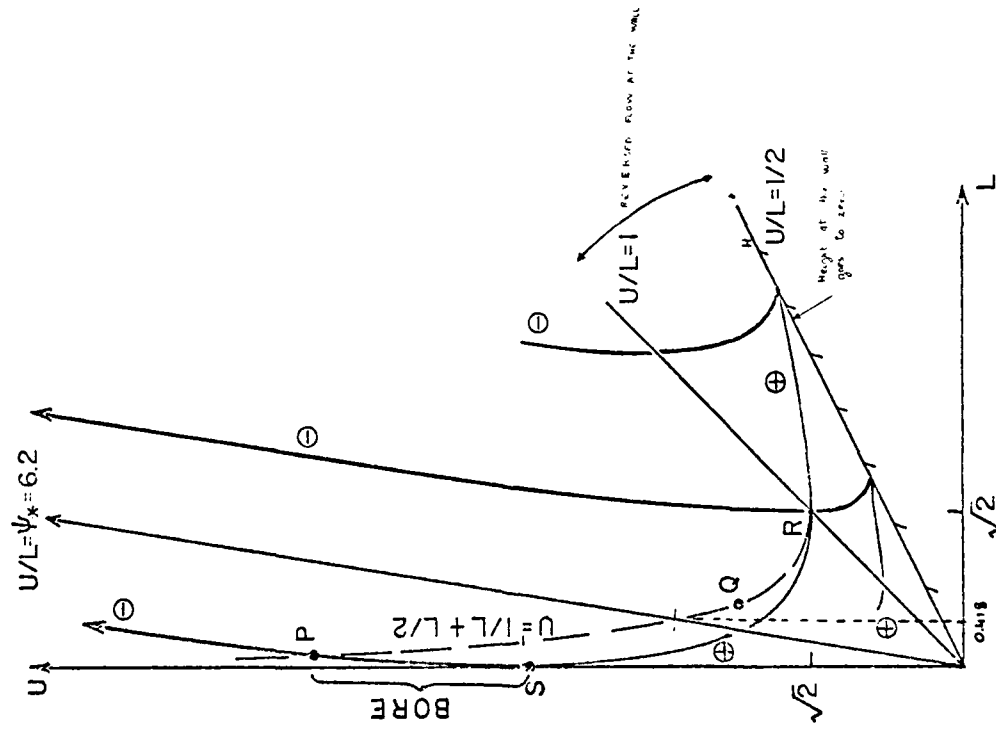


Fig. 3. Zero potential vorticity. ($1/H = 0$). (From Stern, 1979).

For the limit case of $1/H = 1$ (Fig. 5), $L_{\max} \rightarrow \infty$.

- bore solution: for such solutions the Riemann θ curve passing through a given upstream point P (Figs. 3, 4 and 5) intersects the U axis at a value $U(L = 0) < U(P)$: that corresponds to the case of an overrunning bore, where the velocities on the trailing front are larger than the nose speed so that there is a convergent kinetic energy flux towards the nose region which will help to compensate frictional effects there. On the other hand, the overrunning in the nose only occurs until short wave terms come into being and their dispersion effects will give rise to a steady shape of the nose that will travel downstream unchanged in shape. Neither friction nor short waves influences are taken into account in this approach but the argument that could be evoked here is that there exists an intermediate region, not too far behind the point where the front strikes the wall ($L = 0$), where the short wave solution matches the long wave solution found in our problem.

For the case of zero potential vorticity (Fig. 3), one can see that no bore can propagate (i.e., the Riemann θ curve does not intersect the U-axis) for upstream states width larger than $L = 0.418$, for which case the speed of the nose is zero ("arrested bore").

Figure 4 ($1/H = 1/2$) (resp. Fig. 5 ($1/H = 1$)) yield $L^* = 0.422$ (resp. 0.426) and for intermediate values of H, numerical integration shows that:

$$0.418 < L^* < 0.426 .$$

One can then conclude that the finite value of uniform potential vorticity of the intrusion seems to play little influence on the limiting width of stable bore-like intrusions.

On the other hand, in the band where $L < 1$, numerical integration shows also little quantitative differences in the Riemann curves when H varies from 1 to ∞ .

For a resolution of an initial-value problem for a given initial repartition, one should notice that the \oplus and \ominus characteristics have the same slopes in the region where $L = 0$, and also that α_+ and α_- have the same sign in that region: a numerical resolution using the method of characteristics should require analytic expansion near the nose ($L = 0$).

4) Quasi-geostrophic Breaking Wave

The comparisons of the topologies of the Riemann curves and other particular state points locii of Figs. 3, 4 and 5 present an important similarity. The reader is referred to Stern (1979) for a detailed discussion (section of "special solutions") of various nonlinear behaviors that can occur on the trailing geostrophic front. The discussion is mostly based on the amplitude dispersion of the propagation speed along the Riemann curves. The similar properties in our case would be that:

$$\text{for } \frac{U}{H^{1/2}} < \tanh \frac{L}{H^{1/2}}, \quad \alpha_+ \text{ and } \alpha_- \text{ are positive}$$

$$\text{for } \frac{U}{H^{1/2}} > \tanh \frac{L}{H^{1/2}}, \quad \alpha_+ \text{ is positive and } \alpha_- \text{ is negative}$$

$$\text{for } \frac{U}{H^{1/2}} = \tanh \frac{L}{2H^{1/2}}, \quad \alpha_+ = \alpha_- = 0 \text{ (this is important for the "Blocking wave" case).}$$

We shall just show here the generalization of a class of special solutions which is the quasi-geostrophic breaking wave. Let us consider an initial distribution of a basic state of the front far behind the nose, which would correspond to the largest upstream state (i.e., point R on the upstream state curve (see for instance, Fig. 4: $1/H = 1/2$, $L_R = 1.86$ and $U_R = 1.22$)).

If this upstream state is perturbed in such a way as the perturbed distribution corresponds to points lying on the \oplus Riemann curve and lying on each side of $R \cdot U'(R) = 0$ and one can see from equation (21) that the propagation speed for such a wave has opposite sign for points situated on different sides of R : for $L > L_R$ (resp. $L < L_R$), the propagation speed is negative (resp. positive) and increases in magnitude when $L - L_R$ increases in magnitude. Therefore, the crest of the front (max L) moves upstream with the largest speed and the frontal wave pattern steepens on the upstream direction. The transverse velocity on the free streamline is given by eq. (9)

$$v(x, L, t) = \frac{\partial L}{\partial t} + U \frac{\partial L}{\partial x} = \frac{U}{1-U'} \frac{\partial L}{\partial x} \approx U \frac{\partial L}{\partial x}$$

so that v increases as the wave steepens and the current shoots away from the boundary at the steepest parts of the front. It follows from eq. (16) that

$$\left(\frac{\partial h}{\partial x}\right)_{x=L} = U \frac{\partial L}{\partial x}$$

$$v(x, L, t) = \frac{1}{1-U'} \left(\frac{\partial h}{\partial x}\right)_{x=L} \approx \frac{\partial h}{\partial x}$$

so that the wave is also quasi-geostrophic for the transverse velocity

$$(v \approx \frac{\partial h}{\partial x}) \quad \text{as well as for the downstream velocity.}$$

IV. Intrusion Overlying a Second Layer of Finite Depth

In this section, the dynamics of the density current intrusion is coupled with a second layer of uniform depth H_2 . The intrusion layer is still supposed to have a uniform potential vorticity distribution $1/H_1$. The meaning of the various notations are given on Fig. 6. The equations in the same non-

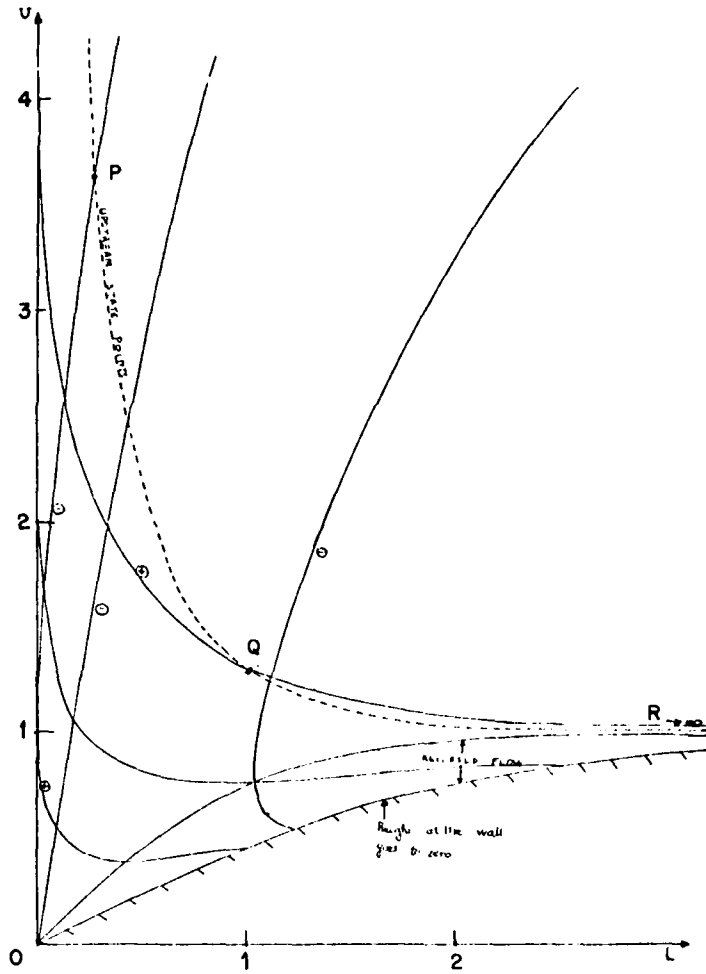


Fig. 5. Intrusion of finite potential vorticity. $1/H = 1$. - Riemann invariants.

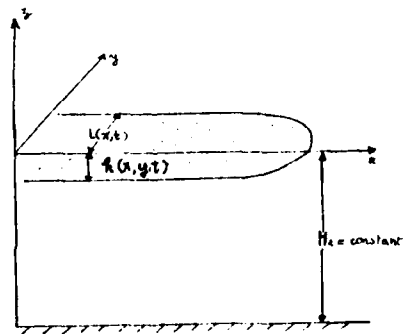


Fig. 6. Intrusion over a finite depth layer.

dimensional quantities as in Section III, are:

1st layer

x-momentum equation: (24)

$$u_{1t} - (1 - u_{1y})v_{1t} + h_x + u_1 u_{1x} = 0$$

vorticity equation: (25)

$$1 - u_{1y} = h/H_1$$

continuity equation: (26)

$$h_t + (h u_1)_x + (h v_1)_y = 0$$

2nd layer

Margules relation: (27)

$$u_1 - u_2 = -h_y$$

vorticity equation (28)

$$u_{2y} = h/H_2$$

Equations (26), (27) and (28) yield:

$$h_{yy} - \frac{h}{H} = 1 \quad (29)$$

where we have introduced the "equivalent depth" H:

$$H = \frac{H_2 H_1}{H_1 + H_2} \quad \text{so that} \quad \frac{H_1}{H} + \frac{H_2}{H} = 1 \quad (30)$$

Equation (29) has the same form as (15) found in section III, but with an equivalent depth in the 2-layer case. In addition to the boundary conditions given in section III, we need an extra boundary condition for the downstream velocity in the second layer $v_2(x,y,t)$. Outside the region lying under the

vertical of the density current intrusion, $h(x,y,t) = 0$ and equation (28) yields $u_{2y} = 0$: since there can be no motion u_2 in the second layer that can extend to $y \rightarrow \infty$, this implies $u_2(x,y,t) = 0$, outside the vertical of the intrusion region, so that the matching condition at the vertical of the free streamline is

$$u_2(x, L(x,t), t) = 0 \quad (31)$$

Solutions of (26), (27) and (28) for $u_1(x,y,t)$, $u_2(x,y,t)$ and $h(x,y,t)$, satisfying the boundary conditions (31) and (8) are:

$$h(x,y,t) = H \left[1 - \cosh \frac{L-y}{H^{1/2}} + \frac{U}{H^{1/2}} \sinh \frac{L-y}{H^{1/2}} \right] \quad (32)$$

$$u_1(x,y,t) = \frac{H}{H_2} (U + y - L) + \frac{H}{H_1} \left[-H^{1/2} \sinh \frac{L-y}{H^{1/2}} + U \cosh \frac{L-y}{H^{1/2}} \right] \quad (33)$$

$$u_2(x,y,t) = \frac{H}{H_2} \left[(y-L) + H^{1/2} \sinh \frac{L-y}{H^{1/2}} + U \left(1 - \cosh \left(\frac{L-y}{H^{1/2}} \right) \right) \right] \quad (34)$$

Again $U(x,t)$ and $L(x,t)$ are the downstream velocity and the y -position of the free streamline.

We have used the same method as in section III, to separate the x and y dependence in the solutions by introducing the variables on the free streamline. The system that $U = U(x,t)$ and $L = L(x,t)$ must satisfy is:

$$U_t + U U_x - L_t = 0 \quad (35)$$

$$\begin{aligned} & (\hat{U} \sinh \hat{L}) \frac{\partial \hat{L}}{\partial t} \\ & + \frac{\partial U}{\partial x} \left\{ \frac{H}{H_2} (\hat{U} - \hat{L}) (\cosh \hat{L} - 1) + \frac{H}{H_1} \left(\frac{\hat{U}}{2} (\cosh 2\hat{L} - 1) - \hat{U} (\cosh \hat{L} - 1) \right) + H^{1/2} \left(\sinh \hat{L} - \frac{\sinh 2\hat{L}}{2} \right) \right\} \\ & + \frac{\partial L}{\partial x} \left\{ \frac{H}{H_2} (\hat{U} - \hat{L}) (\hat{U} \sinh \hat{L} - \cosh \hat{L} + 1) + \frac{H}{H_1} (\hat{U} \cosh \hat{L} - H^{1/2} \sinh \hat{L} - \hat{U} \cosh 2\hat{L} + \frac{U^2 + 4}{2H^{1/2}} \sinh 2\hat{L}) \right\} = 0 \end{aligned} \quad (36)$$

where $\hat{U} = U/H^{1/2}$, $\hat{L} = L/H^{1/2}$.

The solution using Riemann invariants yields:

$$\left(\frac{dU}{dL} \right)_{\oplus}^{\ominus} = 1 - \frac{2\hat{U} \cosh(\hat{L}/2)}{a \pm \sqrt{a^2 + b^2}} \quad (37)$$

$$\text{with } a = \cosh\left(\frac{\hat{L}}{2}\right) \left[\hat{U} - \frac{H}{H_2} (\hat{U} - \hat{L}) - \frac{H}{H_1} (\hat{U} \cosh \hat{L} - \sinh \hat{L}) \right]$$

$$b = 2 \sinh(\hat{L}) \left[\frac{H}{H_2} (\hat{U} - \hat{L}) + \frac{H}{H_1} (\hat{U} \cosh \hat{L} - \sinh \hat{L}) \right]$$

The limit case where $H_2 \rightarrow \infty$ corresponds to the solutions found in section III. We have only investigated in this case, the "arrested" bore solution using again a second order Runge-Kutta scheme: the maximum width for a bore

to propagate for $H_1 = H_2 = 1$ is

$$L^* = 0.4185$$

so that the inclusion of the dynamics of a second layer seems to play little influence on the numerical result found in section III.

V. Conclusion

The results of the previous sections concerning the maximum width of a bore-type intrusion strongly lead to the conjecture that there exists a limiting width of the boundary current far upstream of the nose, in the region where the current appears to be both laminar and steady. The existence of this maximum width is a consequence of the analytical resolution of the dynamics of the flow, whereas previous studies have evoked dimensional arguments to limit this width. Therefore, the need is felt for a careful experimental measurement of this width, using immiscible fluids (such as silicon oil and a mixture of ethyl and water in order to obtain small density differences) so that the interface between the two fluids is sharply defined and that no mixing occurs. If the actually measured maximum width exceeds the theoretical value found here, this will stimulate further theoretical investigations to relax the long-wave assumption in the downstream direction, and include short waves dispersion effects at the nose of the intrusion, which could lead to a steady shape of the nose like those observed in the preliminary experiments.

In this work, an outline of some non-linear interaction on the trailing front has been sketched. A thorough study would require a numerical resolution of given initial-value repartitions. It would be interesting to test, particularly if one can reproduce numerically instabilities such as those observed in the experiment. However, the theory is strongly restricted by the assumption of uniform potential vorticity distribution in each layer, since this filters out all the geostrophical unstable modes for which (Stern, 1975, page

68-71) a necessary condition for amplifying waves in that the gradient of the basic potential vorticity must assume both positive and negative values within the cross-stream interval of the jet.

The mathematical method used in the two-layer case may be used for an analytical approach of the classical frontal waves problem as initially posed by the Norwegian school (Orlanski, 1968) for an atmospheric front intersecting the ground.

Acknowledgements

I would like to thank Melvin Stern for a very stimulating and enjoyable summer's work. I am also grateful to George Veronis, who suggested to me the initial subject of this work, and to Adrian Gill for his helpful comments.

REFERENCES

- Barr, D.I.H., 1967. Densimetric exchange flow in rectangular channels. III. Large scale experiments. La Houille Blanch, 22, 619-32.
- Gill, A., 1976. Adjustment under gravity in a rotating channel flow. Jour. Fluid Mech., 77,, pt. 3, 603-631.
- Gill, A. and E. Schumann, 1979. Topographically induced changes in the structure of an inertial coastal jet: application to the Agulhas Current. Submitted to D.S.R.
- Orlanski, I., 1968. Instability of frontal waves. Jour. Atmos. Sci., 25, n^o2, 178-200.
- Stern, M., 1975. Ocean circulation physics, Academic Press, New York.
- Stern, M., 1979. Geostrophic fronts, bores, breaking and blocking waves. Submitted to
- Wadhams, P., A. E. Gill and P. F. Linden, 1979. Transects by submarine of the East Greenland Polar Front. Submitted to D.S.R.
- Whitehead, J. A., A. Leetma and R. A. Knox, 1974. Rotating hydraulics of strait and sill flows. Jour. Geophys. Fluid Dyn., 6, 101-105.